EVALUATION OF OPTOACOUSTIC FREQUENCY ANALYSIS SENSITIVITY TO DISCRIMINATE HEALTHY AND NEOPLASTIC TISSUES AND TO MONITOR TREATMENT-INDUCED PHYSIOLOGICAL CHANGES

BY

MICHELLE PATTERSON

A Thesis
Submitted to the Graduate Faculty
in Partial Fulfillment of the Requirements
for the Degree of

DOCTOR OF PHILOSOPHY

Department of Biomedical Sciences
Faculty of Veterinary Medicine
University of Prince Edward Island

CONDITIONS FOR THE USE OF THE THESIS

PERMISSION TO USE GRADUATE THESIS

Title of Thesis:	Evaluation of optoacoustic frequency analysis sensitivity to discriminate healthy and neoplastic tissues and to monitor treatment-induced physiological changes.
Name of Author:	Michelle Patterson
Faculty:	Faculty of Veterinary Medicine
Department/Discipline:	Biomedical Sciences
Degree:	Doctor of Philosophy (PhD) Year: 2014
Name of Supervisor(s):	Dr William Whelan & Dr Christopher Riley

Members of Supervisory Committee:

Dr Andy Tasker (Chair)
Dr LeeAnn Pack
Dr Yingwei Wang

In presenting this thesis in partial fulfillment of the requirements for a graduate degree from the University of Prince Edward Island, the author has agreed that the Robertson Library, University of Prince Edward Island, may make this thesis freely available for inspection and gives permission to add an electronic version of the thesis to the Digital Repository at the University of Prince Edward Island. Moreover the author further agrees that permission for extensive copying of this thesis for scholarly purposes may be granted by the professor or professors who supervised the author‘s thesis work, or, in their absence, by the Chair of the Department or the Dean of the Faculty in which the author‘s thesis work was done. It is understood that any copying or publication or use of this thesis or parts thereof for financial gain shall not be allowed without the author‘s written permission. It is also understood that due recognition shall be given to the author and to the University of Prince Edward Island in any scholarly use which may be made of any material in the author‘s thesis.

Signature: _____

Address:

Date: _____

University of Prince Edward Island
Faculty of Veterinary Medicine
Charlottetown

CERTIFICATION OF THESIS WORK

We, the undersigned, certify that Michelle Patterson, BSc, candidate for the degree of Doctor of Philosophy (PhD), has presented her thesis with the following title:

EVALUATION OF OPTOACOUSTIC FREQUENCY ANALYSIS SENSITIVITY TO DISCRIMINATE HEALTHY AND NEOPLASTIC TISSUES AND TO MONITOR TREATMENT-INDUCED PHYSIOLOGICAL CHANGES

that the thesis is acceptable in form and content, and that a satisfactory knowledge of the field covered by the thesis was demonstrated by the candidate through an oral examination held on _____, 2013.

Examiners:

Dr. Jeffrey Carson _____

Dr. William Whelan _____

Dr. Christopher Riley _____

Dr. Leeann Pack _____

Dr. Robert Hurta _____

Date: _____

ABSTRACT

One of the major limitations of the use of optoacoustics (OA) for the imaging of prostate cancer is the relatively low resolution when performed in real time. The work presented in this thesis aims to address this limitation by applying frequency-based analyses, which contribute additional information on sub-resolution structures to OA images, and may prove useful for advanced detection and monitoring of prostate cancer.

Optoacoustic imaging was employed to distinguish physiological differences between tissues in *in vivo* mouse models (transgenic adenocarcinoma of mouse prostate [TRAMP] and C57Bl6) and vascular casts of mouse renal and hepatic vasculature, and heat-induced physiological changes in *ex vivo* bovine liver during laser thermal therapy (LTT). Optoacoustic signal intensity and frequency spectrum analyses were performed on signals obtained from a reverse-mode OA imaging system (Seno Medical Instruments Inc., San Antonio, TX) with a 775 nm pulsed optical illumination

Neoplastic prostate tissue and laser-induced tissue changes were identified based on the OA signal amplitude in combination with spectral analysis of the OA radiofrequency (RF) data. Tumours generated higher amplitude signals than those of the surrounding tissues, with contrast ratios of 33 ± 3 dB. In *ex vivo* bovine liver, the amplitude of the post-treatment OA signals was on average three times higher compared with pre-treatment signals. The RF spectrum analysis showed significant differences between neoplastic and normal tissues, and between pre-heated and post-heated tissues. The midband fit was 62% (5 dB) higher, the intercept 57% (4 dB) higher and the spectral slope 50% (0.4 dB/MHz) higher for neoplastic prostate tissue compared to normal tissues in the control mice.

These spectral parameter values were further investigated using simple and complex phantoms and were found to relate to the size and density of the OA targets (in this case, vasculature). During LTT, the midband fit and intercept increased on average by 7 ± 1 dB and 9 ± 1 dB, respectively, and the slope decreased on average by 0.3 ± 0.1 dB. Unlike the amplitude of the OA signal, the spectral parameters were not significantly affected by the temperature of the target during LTT. The spectral parameters, thus, may have been affected primarily by tissue state (i.e. native or coagulated). Thus, this may provide a means of monitoring LTT directly using OA imaging, rather than through monitoring temperature which is often used as a surrogate of damage.

The results of this study demonstrate that OA imaging provides high-contrast imaging of a murine model of prostate cancer *in vivo*, and real-time monitoring of LTT *ex vivo*. Analysis of OA frequency parameters may offer information on sub-resolution vascular structures in the neoplastic tissue. Optoacoustic frequency analysis may also offer a more direct measure of tissue thermal damage compared to temperature-based methods. Such OA frequency analysis, in combination with OA thermometry, may represent an improved strategy for monitoring LTT. This analysis technique may be applied to any OA signal to provide additional information on sub-resolution tissue structures. Overall, this represents a promising technique for improving prostate tumour detection and real-time treatment monitoring.

ACKNOWLEDGEMENTS

During the course of my studies, I have been blessed with the support and guidance of many talented and enthusiastic individuals. Without their assistance, this thesis and the work contained within it would not have been possible.

First and foremost, I would like to thank my co-supervisors Dr Whelan and Dr Riley whose advice and constant encouragement have been invaluable. I have had the freedom to travel, to present my research at national and international conferences, and to coordinate Let‘s Talk Science UPEI, all of which has had an incredible impact on my graduate school experience, as well as my career development.

Every member of the Whelan lab over the years has contributed something positive toward my experience. Specific assistance in this thesis work was provided by Michel Arsenault, who acquired some of the images for the animals studies, Jonathan Horrocks, who helped to construct and image the microsphere phantoms, and Janice Murphy who provided valuable technical assistance. Without their assistance, I truly would not have accomplished all that I did.

I thank my supervisory committee members: Dr Andy Tasker (chair), Dr LeeAnn Pack, and Dr Yingwei Wang, who continue to tirelessly assist me with my ongoing career endeavors. Thank you to Jonathan Spears, the UPEI university veterinarian, for his support and endless patients helping me to develop and carry out the animal experiments. The staff of the UPEI animal facility has also provided valuable assistance with the animal research performed in this thesis.

Funding support from Innovation PEI, the Atlantic Veterinary College, and the Department of Biomedical Sciences is also acknowledged and greatly appreciated.

To all of you with whom I have had the privilege of sharing an office over the last 5 years: thank you for everything. To Kate, Jessy, Janet, Amber, Emily, Jess, Denise and especially Bob: we had some great times and made memories that I will treasure.

And last, but not least, I would like to thank my family that have been tremendously supportive throughout my graduate program. To my parents Paul and Betty Macphee, thank you for your support during busy times in all our lives. You have been endlessly generous and thoughtful. To my husband, Jordan Patterson and our son Milo, thank you for your unwavering support and confidence in me, and for always being there when I needed you.

DEDICATION

I would like to dedicate this thesis to my parents,

Paul and Betty Macphee,

whose passion for helping others has been my inspiration

and to my husband and son

Jordan and Milo Patterson

for giving me the courage to pursue my dreams.

TABLE OF CONTENTS

LIST OF FIGURES

LIST OF TABLES

LIST OF SYMBOLS AND ABBREVIATIONS

A-line	Amplitude line
APS	Average power spectrum
BNF	Biological nitrogen fixation
CEM43°C	Cumulative equivalent minutes at 43°C
CNR	Contrast to noise ratio
CT	X-ray computed tomography
DIS	Double integrating sphere
DOT	Diffuse optical tomography
FFT	Fast Fourier transform
FWHM	Full width half max
Hb	Deoxygenated hemoglobin
HbO2	Oxygenated hemoglobin
IAD	Inverse adding double algorithm
IAP	Integrated amplitude projection
LTT	Laser thermal therapy
MIP	Maximum intensity projection
MRI	Magnetic resonance imaging
NE	Neuroendocrine
NIR	Near Infrared Region
OA	Optoacoustic
OCT	Optical coherence tomography
PIN	Prostate intraepithelial neoplasia

PU4ii	Polyurethane based resin
PZT	Piezoelectric
RF	Radio frequency
ROI	Region of interest
ROI_analysis	Region of interest used for analysis
ROI_scan	Region of interest scanned by the imaging system
SNR	Signal to noise ratio
TGC	Time gain control
TRAMP	Transgenic adenocarcinoma of mouse prostate
TRUS	Transrectal ultrasound

μ_a	Absorption coefficient
μeff	Effective attenuation coefficient
$\mu^{s\prime}$	Effective scattering coefficient
μ^s	Scattering coefficient
A	Amplitude
a	Amplitude attenuation factor
A_o	Incident amplitude
A_λ	Absorbance
c	Speed of sound
c_c	Concentration
c_p	Specific heat
D	Cylinder diameter
DL	Left child branch diameter

DR	Right child branch diameter
D_T	Thermal diffusivity
ε	Molecular density
H(r,t)	Heat source
H_T	Hilbert transform
I(z)	Intensity at depth
I_o	Initial intensity
L	Cylinder length
l	Path length
L_p	Characteristic linear dimension
ø	Rotation of child branch with respect to reference plane
OA_{corr}	Depth correction factor of optoacoustic signal intensity
OA_{HT}	Hilbert transform of the optoacoustic signal amplitude
p	Pressure
r	Position
R^2	Coefficient of determination
Rd	Diffuse reflectance
S	Raw signal
t	Time
Tc	Collimated transmittance
Td	Diffuse transmittance
v	Velocity
w	width

z	Distance
β	Isobaric volume expansion coefficient
Γ	Grüeneisen parameter
ΔP	Optoacoustic pressure change
θ	Angle
ρ	Density
τ_p	Laser pulse duration
τ_{th}	Relaxation time
Φ	Laser fluence

CHAPTER 1

GENERAL INTRODUCTION

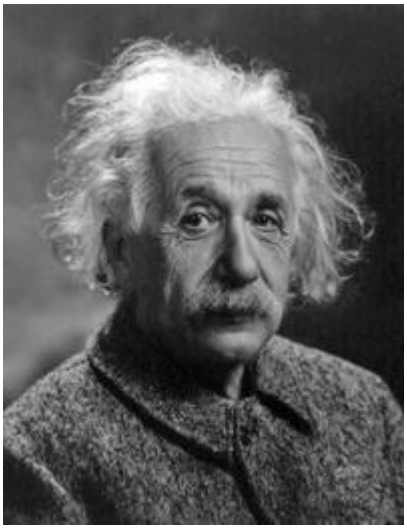

"Learn from yesterday, live for today, hope for tomorrow. The important thing is to not stop questioning."

-Albert Einstein (1879-1955)
picture from http://www.goodreads.com/author/show/9810.Albert_Einstein

1.1 Prostate cancer

Prostate cancer is the most common cancer among men in developed countries. An estimated 240,000 men in the United States were diagnosed with prostate cancer in 2012, resulting in over 28,170 deaths [1] . While prostate cancer can be deadly, approximately 95% of men diagnosed with the disease will survive over 5 years [2], and 83% of men will survive more than 10 years post diagnosis if the disease is found in its early stages [3]. However, diagnosis of this disease in its early stages remains unreliable, and treatments of early-stage prostate cancer are often associated with adverse side effects [4].

1.2 Diagnosis and treatment techniques

Conventional diagnosis of prostate cancer involves using imaging techniques such as ultrasound, CT, and MRI to identify suspect areas in the prostate which are then biopsied for definitive diagnosis [5]. These imaging techniques, however, cannot reliably distinguish neoplastic from healthy prostate tissue with an estimated sensitivity of only 50% [6]. This leads to a large sampling error associated with biopsies [5]. Hence, the ability to accurately image potentially neoplastic regions in the prostate may better determine if and where a biopsy is necessary (i.e. targeting).

One of the most common techniques used for local grading of the prostate is transrectal ultrasound because it can be performed in real-time and has relatively good resolution [7]. However, the accuracy of this technique is reported to be less than 50-60% with respect to detection of prostate cancer, due largely to the weak contrast at depth in soft tissues [7–9]. Conventional diagnosis is currently based solely on detection of gross

anatomic properties of tissues [10]. Recent ultrasound techniques have been developed that probe tissue microstructure based on the spectral analysis of the ultrasound radiofrequency (RF) data [11,12]. However these techniques do not provide any information on the oxygen saturation or hemoglobin concentration of the tissue, both of which are often altered with neoplasia [13,14]. Pure optical imaging techniques, such as diffuse optical tomography (DOT), are being investigated as possible targeting technologies for prostate cancer because of their ability to achieve adequate contrast in soft tissues and their ability to measure the oxygen saturation and hemoglobin concentrations of the tissues [14]. These techniques, however, suffer from strong light scattering in biological tissues [17], resulting in either very limited imaging depth (<1 mm) as in optical coherence tomography (OCT), or limited resolution, as in DOT [17–19].

Once prostate cancer has been diagnosed, treatment can ensue. Unfortunately, due to the location of the prostate and morbidity associated with current treatment methods (e.g. radiation, surgery), many men face difficulties with health-related quality of life during and post-treatment [20]. The most common problems involve urinary, sexual, and bowel dysfunctions [3]. These issues usually do not arise until advanced stages of the disease or until treatment begins [21].

The greatest downfall of current treatments of prostate cancer are that they target the whole prostate regardless of the size of the tumour. This approach not only damages the cancerous tissue but may also damage the surrounding healthy tissue of the prostate which leads to the health issues previously mentioned [5]. New treatment methods have been developed that may focally target the neoplastic tissue within the prostate leaving the healthy prostate tissue unaffected [8,22]. The challenge with these treatments is that

they require real-time, high resolution, high contrast monitoring which cannot simultaneously be achieved with any current imaging modalities (e.g. CT, MRI, ultrasound, etc) [8,23].

1.3 Optoacoustic wave generation

1.3.1 Physics of optoacoustics

Optoacoustic (OA) imaging (analogous to photoacoustic imaging) overcomes the limitations described by merging the contrast capability of optical imaging with the resolution of ultrasound imaging [16]. Image contrast in OA imaging is related to the optical properties of the target, as in pure optical imaging and the thermomechanical properties of the target. The resolution and the maximum imaging depth are scalable with the ultrasonic frequency as in ultrasound imaging [13]. Consequently, OA imaging can provide high contrast images with good resolution and penetration depth in soft tissue [24,25], potentially providing a useful monitoring technique for prostate cancer treatments. This emerging technique exposes tissues to nanosecond pulsed laser light, which induces tissue-generated acoustic waves that are detected using wide band transducers [26,27].

Short laser pulses are absorbed by tissue based on local optical properties and, if the conditions of stress confinement and thermal confinement are met, a high frequency pressure wave is generated [28]. Thermal confinement is satisfied if the duration of the laser pulse (τ_p) is less than the thermal relaxation time (τ_{th}). The thermal relaxation time after absorbing a laser pulse of length τ_p is estimated to be [28];

$$\tau_{Th} = \frac{L_p^2}{4*D_t} \quad [1]$$

where D_T is the thermal diffusivity of the sample and L_p is the characteristic linear dimension of the tissue volume being heated [28]. Stress confinement is satisfied when the duration of the laser pulse (τ_p) is less than the time it takes for the stress to transit the heated region (τ_s). This value can be estimated as;

$$\tau_s = \frac{L_p}{c} \quad [2]$$

where L_p is the characteristic linear dimension of the tissue volume being heated and *c* is the speed of sound in the tissue [28]. A typical value for many soft tissues is D_T=1.4x10^{-3} cm^2/s. So, for example, to image (i.e. resolve) a target of size 100 μm, thermal confinement is satisfied when the duration of the laser pulse is less than 18 μs. To image (i.e. resolve) a target of size 100 μm, stress confinement, using speed of sound in water of 1500 m/s, is satisfied when the duration of the laser pulse is less than 60 ns. Under the stress confinement condition, high thermoelastic pressure can build up quickly creating the pressure wave which is detected as an OA signal. The propagation time of the pressure wave provides quantitative depth information.

The pressure, *p(r,t)* at position *r* and time *t*, which arises in response to a heat source *H(r,t)* in an acoustically homogeneous medium is governed by the following wave equation [29,30];

$$\nabla^2 p(r,t) - \frac{1}{c^2}\frac{\partial^2}{\partial t^2} p(r,t) = -\frac{\beta}{C_p}\frac{\partial}{\partial t} H(r,t) \quad [3]$$

where *H(r,t)* is a heating function defined as the thermal energy deposited per time per volume, β is the isobaric volume expansion coefficient in K^{-1}, and c_p is the specific heat in J/(K*kg)

A solution to the wave equation describes the intensity of the generated OA signal which is dependent on the optical and physical properties of the target as well as the laser energy used;

$$\Delta p = \mu_a \Gamma \Phi \quad [4]$$

where μ_a is the absorption coefficient of the target, Γ is the Grüneisen parameter (i.e. $(\beta c_s / c_p)$ where c_s is the speed of sound and c_p specific heat) which is dependent on several physical characteristics of the target, and Φ is the laser fluence (i.e. energy per unit area) [28].

1.3.2 Optical absorption

The amplitude of an OA signal is largely dependent upon the optical absorption properties of the target (e.g. the absorption coefficient). The absorption coefficient describes the amount of light absorbed by the target, and is wavelength dependent. Absorption coefficient values as a function of wavelength of several biological chromophores are presented in Figure 1.1.

The large variation in absorption coefficient values with wavelength, allows for multi-wavelength optoacoustic imaging to be used for characterization of certain tissue properties [10]. For example, oxygenated hemoglobin (HbO_2) and non-oxygenated hemoglobin (Hb) have different wavelength-dependent optical absorption properties. This allows optoacoustic imaging to differentiate between arteries (oxygenated) and

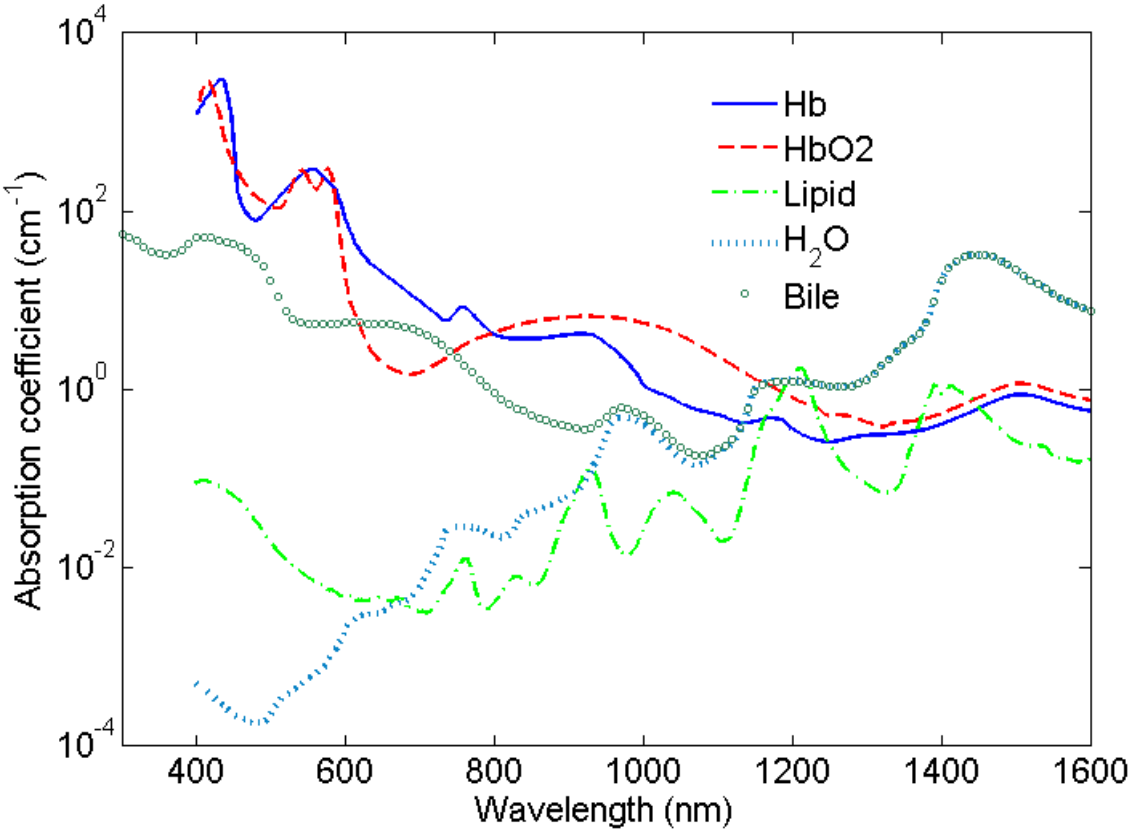

Figure 1.1: Absorption coefficients of deoxygenated hemoglobin (solid line), oxygenated hemoglobin (dashed line), lipid (dashed-dotted line), bile (circle-marked line) and water (dotted line) from 400 to 1600 nm . The absorption coefficient axis is in a logarithmic scale (adapted with permission) [31].

veins (deoxygenated) based on their relevant signal amplitudes at two wavelengths (one at which HbO_2 has a higher absorption than Hb, and another at which Hb has a higher absorption than HbO_2). Furthermore, Hb and HbO_2 have the same absorption at approximately 800 nm. Optoacoustic signals acquired at this and other wavelengths can be used to calculate relative hemoglobin oxygen saturation and total hemoglobin concentration [32].

The wavelength range between approximately 650 nm and 1100 nm is known as the optical window in biological tissues [31]. At these wavelengths light has a maximum penetration depth in biological tissues. Within the optical window, scattering is the dominant light-tissue interaction; thus, propagating light gets diffused to a greater extent than at wavelengths outside the optical window [33]. Since scattering increases the distance that photons can travel, the photons may penetrate further into the tissue [31,34].

1.3.3 Acoustic wave propagation

Acoustic (or sound) waves propagate in longitudinal motion (compression and expansion) [35]. They are inherently three-dimensional and are time-dependent (t). Acoustic pressure, $p(x, y, z, t)$, is often used to describe an acoustic wave. For longitudinal waves, the acoustic pressure is related to the underlying particle velocity [36];

$$p(x, y, z, t) = v(x, y, z, t) * \rho * c \quad [5]$$

where ρ is the density of the medium (kg/m^{-3}), and c is the speed of sound in the medium (m/s) [37].

Acoustic waves are partially reflected and refracted by boundaries between two media with different densities. The transmitted portion of the wave is 'bent' (i.e. refracted) [37]. This propagation follows Snell's Law (Figure 1.2);

$$\frac{\sin\theta_i}{c_1} = \frac{\sin\theta_r}{c_1} = \frac{\sin\theta_t}{c_2} \quad [6]$$

where θ_i, θ_r and θ_t are the angles of the incident, reflected and transmitted wave with respect to the vertical axis and c_1 and c_2 are the speed of sound in both media [37].

Attenuation is the term used to account for loss of wave amplitude (or strength) due to all mechanisms, including absorption and scattering. Amplitude decay can be modeled as [36];

$$A(z) = A_o e^{-\alpha z} \quad [7]$$

where a is the amplitude attenuation factor ($dB/MHz^{-1}cm^{-1}$) which is dependent on frequency, A_o is the incident amplitude of the wave and z is distance.

1.4 Optoacoustic detection and imaging

1.4.1 Ultrasound transducers

Ultrasound refers to waves with frequencies that are greater than 20 kHz [36]. Ultrasound transducers produce ultrasound waves that are directed into tissue and are reflected/transmitted at boundaries between tissues with different densities [38]. The reflected portion propagates and is then detected by the transducer.

Almost all medical ultrasound transducers are made of lead zirconate titanate (PZT) [39]. PZT is a ceramic ferroelectric crystal, also known as a piezoelectric crystal,

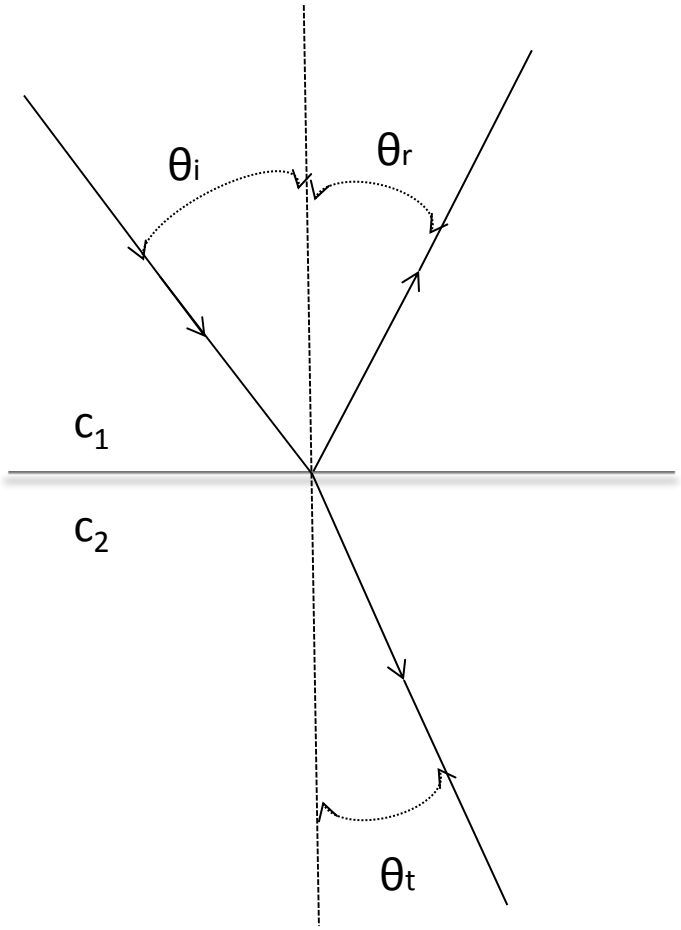

Figure 1.2: Bending of acoustic waves from one medium to another with different density follows Snell's Law [6].

that exhibits a strong piezoelectric effect [40]. The "piezoelectric effect" is the production of electricity or electric polarity in response to mechanical stress on certain crystals [40]. The converse effect (reverse piezoelectric effect), is also valid, in which mechanical stress (compression and expansion of the crystal) can be produced by an applied potential difference [39]. Ultrasound is a mechanical wave and, therefore, by applying a potential difference to the piezoelectric crystal in the transducer, ultrasound waves can be generated by the rapid compression/expansion of the crystal. The reflected ultrasound waves will also interact with the crystal by applying 'stress' which will generate electrical signals [39].

Ultrasound transducers, or arrays of transducers (transducers connected in series) come in many sizes and shapes (e.g. circular, rectangular), the simplest of which contains one piezoelectric crystal [41]. The essential components of a single crystal transducer are shown in Figure 1.3.

The crystal is the most important component of the transducer and is a thin piece of piezoelectric material near the front surface of the transducer [41]. The thickness of the crystal dictates the frequency of vibrations that the crystal/transducer are capable of producing and detecting [41]. The front and back surfaces of the crystal are coated with films of electrically conducting material to facilitate connections with the electrodes which establish the potential difference needed to compress/expand the crystal, thereby generated ultrasound waves [40]. These electrodes also detect the signal generated in the crystal when the reflected waves return. The backing material situated behind the crystal is heavily absorbing of ultrasound waves [41]. The purpose of this backing is to

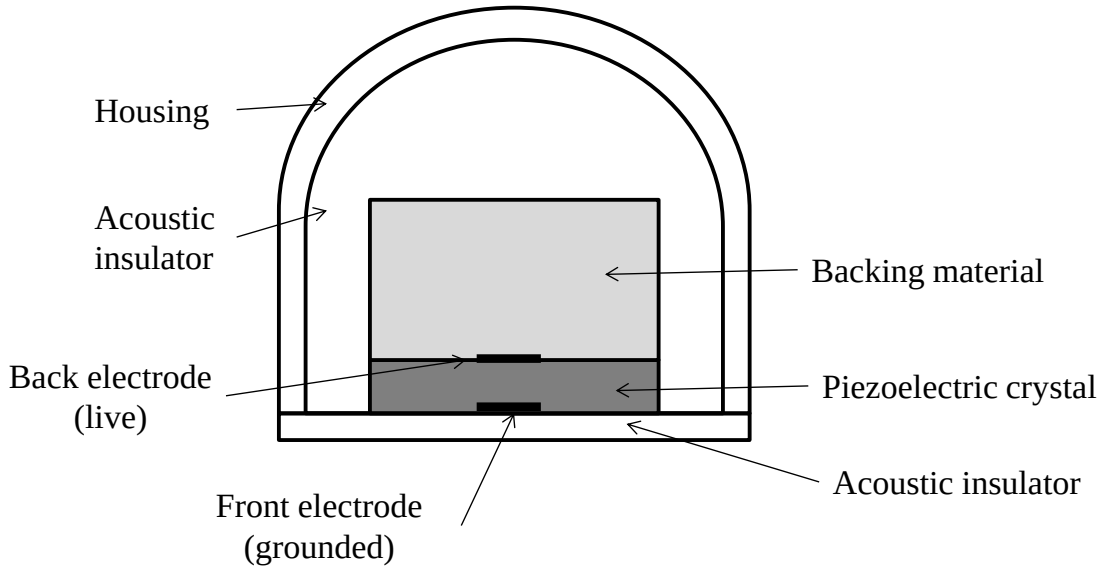

Figure 1.3: The essential components of a single piezoelectric crystal transducer.

absorb ultrasonic energy transmitted back into the transducer and thereby dampen the oscillations of the crystal following a pulse. The acoustic insulator prevents ultrasound waves originating from the crystal from being transmitted into the transducer housing. It also insulates the crystal from external sources of ultrasound [40]. The transducer house consists of a robust material that houses all the components of the transducer.

1.4.2 Signal processing

In OA imaging, absorber-generated pressure waves are detected by an ultrasound transducer (or an array of transducers). These time-dependent signals are recorded by each transducer and a reconstruction (i.e. beamforming) is applied based on the type of transducer and array employed [42,43]. Beamforming is a signal processing technique that involves merging signals detected by numerous transducers in such a way that signals at certain angles experience constructive interference while signals at other angles experience destructive interference [44]. An annular array transducer (as used in this study) consists of several concentric piezoelectric ring sensors (Figure 1.4a). Each of these rings can be described by their radius (r_i) and width (w_i). An acoustic wave generated at a distance d from the transducer surface at time t=0 arrives at the i^{th} transducer at time t_i (Figure 1.4b). The delay-time that a wave will reach each transducer can be calculated by using its radius, $r_{i,}$ and the speed of sound, c. Conversely, the distance of a target from the transducer can be calculated using the arrival time of the wave [44].

The achievable resolution of each transducer in the array is dependent upon the depth, z, of the optoacoustic source, as well as on the diameter and width of the

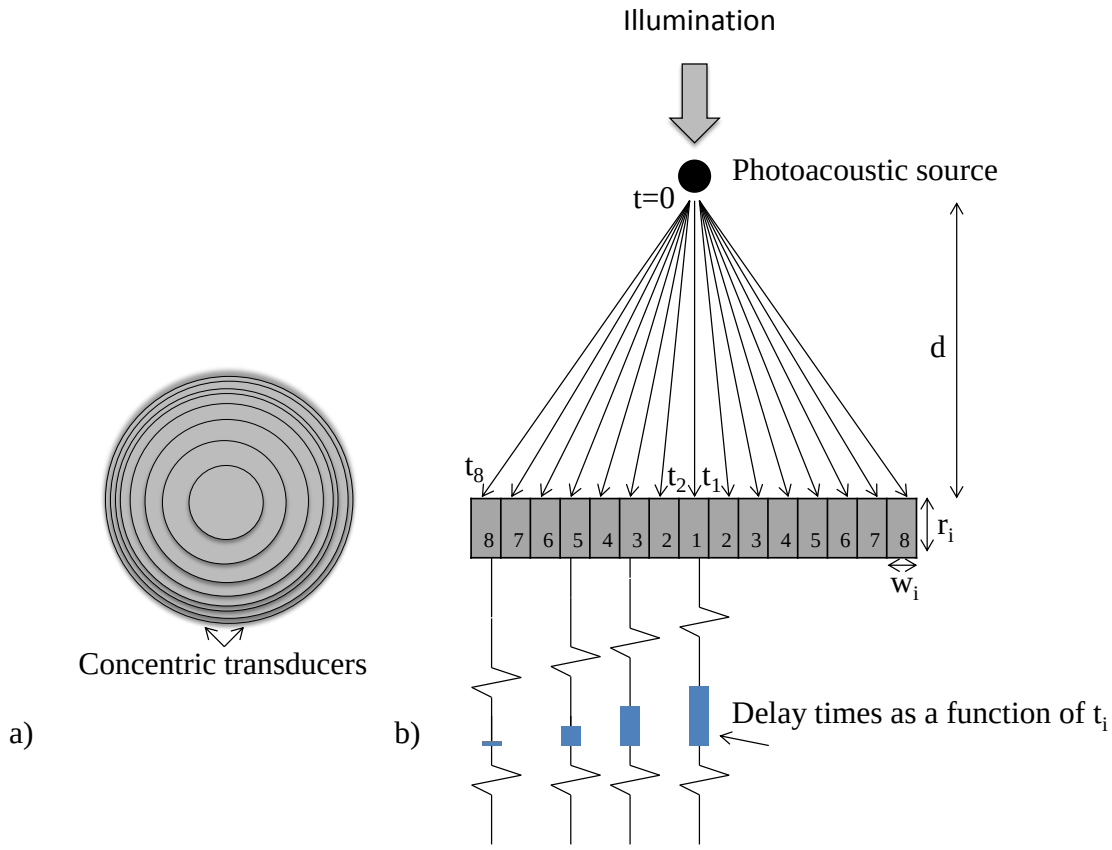

Figure 1.4: Schematics of (a) an annular array transducer consisting of 8 concentric piezoelectric ring sensors. Each transducer ring has the same surface area, and (b) acoustic wave delay time generated by an optoacoustic source at a distance d from the transducer surface at time t=0 and arriving at the i^{th} transducer at time t_i. Delay times as a function of t_i are applied to the wave detected by each transducer, thereby interpolating them to a common axis to be summed for optimal focusing.

transducer [44].

A signal originating from a source at t=0 will take longer to reach transducer rings further from the center ring simply due to the distance that they must travel to reach them. This delay is the difference between t_1 and t_i, and is accounted for prior to summing the detected signals. Signals detected by each transducer are, thus, interpolated to a common axis and summed to achieve optimal focusing [36]. This type of focusing can enhance the amplitude of the signals on the axis by a factor related to the number of transducer rings and suppresses artifacts originating in areas away from the axis [44].

Once this has been applied to the signal received by each ring, the resulting signal is referred to as an amplitude line (A-line) signal. An image is formed by acquiring A-line signals across the axis parallel to the transducer and arranging them in order to produce a two- or three-dimensional image [45].

1.4.3 Image formation

The Hilbert transform is an important tool for signal processing and is often applied to OA signals [28]. The Hilbert transform selectively enhances 'edges' in an image. The Hilbert transform causes a phase shift in the bipolar pressure signals, producing a maximum at the transition point from positive to negative pressure. Since this intercept corresponds to the approximate center of the source, Hilbert transformed signals are thought to be better suited for image analysis compared with the raw signals [28]. The Hilbert transform is described by the following equation;

$$SH(z) = \sum_{i=1}^{N}\left[H_t\left(S_i(z)\right)\right],\ z = \sqrt{(ct_i)^2 - r_i^2} \quad [8]$$

In this equation, S_i is the raw signal received by the i^{th} ring, r_i is the radius of the i^{th} ring, c is the speed of sound, and H_T represents the Hilbert transform [44].

1.5 Optoacoustic applications

1.5.1 Tumour imaging

Solid tumours often have an increased blood flow and, therefore, have a higher hemoglobin concentration compared to healthy prostate tissue [46,47]. OA imaging takes advantage of the high optical absorption of hemoglobin compared with other tissue components, at wavelengths in the visible and near infrared (NIR) range, to generate higher amplitude signals in regions with higher hemoglobin concentrations (e.g. at the location of the tumour) [48].

OA imaging has the ability to image vascular structures *in vivo* with high resolution and high contrast. OA images of tumour vasculature have been shown by a number of groups [25,48–51]. Lao et al. (2008) monitored tumour growth of subcutaneous inoculated breast cancer tumour cells in a mouse over a 20 day period using a 532nm laser (Figure 1.5) [49]. They found that morphological vascular features of early tumour growth could be detected using OA imaging. In addition, changes in the morphology and optical absorption (which is highly correlated with the total hemoglobin concentration of the blood at this wavelength) of the vessels were observed over the duration of the experiment. Total acquisition time for each image was approximately 18 minutes. Laufer et al.(2012) imaged human colorectal tumour xenografts implanted

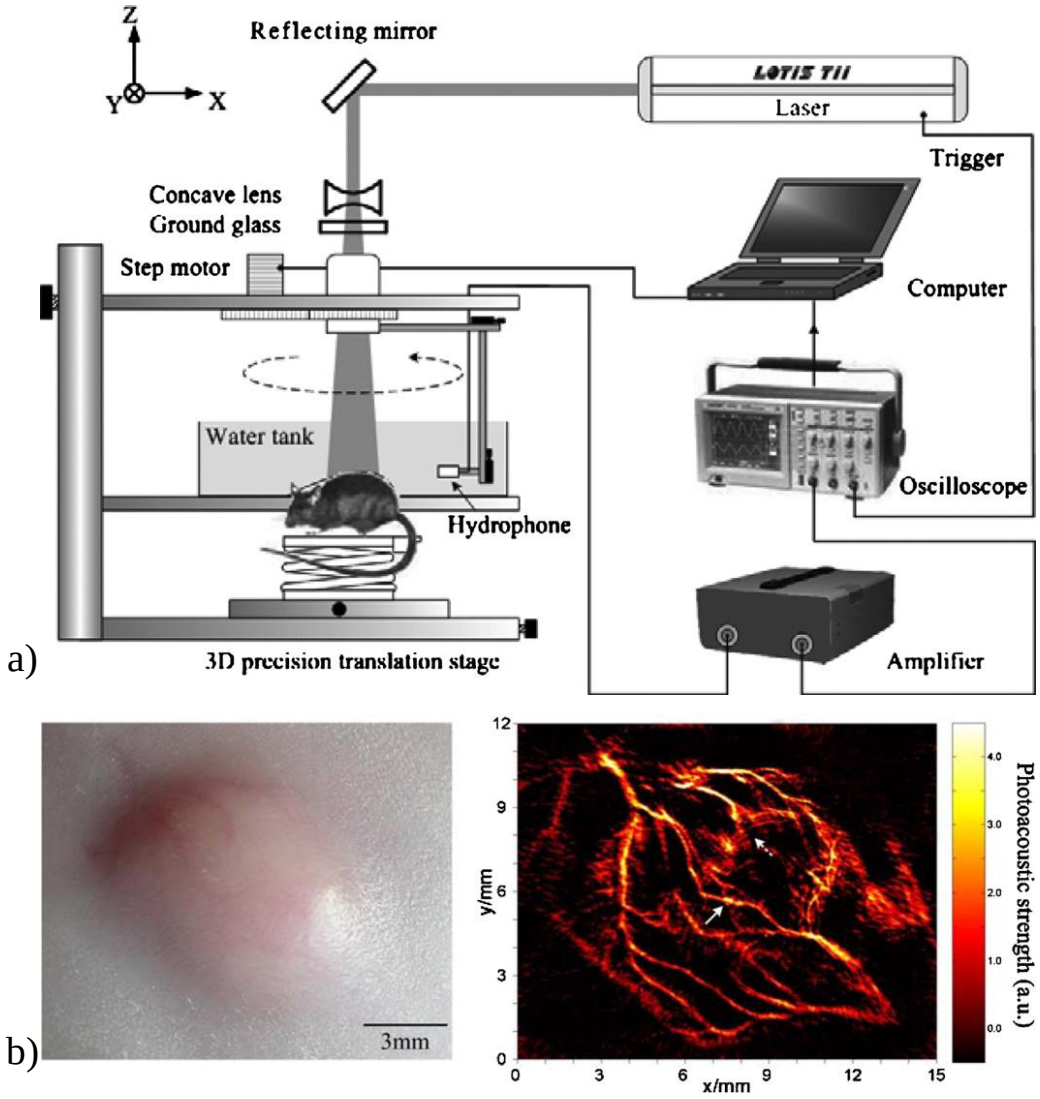

Figure 1.5: a) Schematic diagram of the optoacoustic imaging system used by Lao et al. (2008), and b) photograph of tumour nodule (left) and corresponding optoacoustic image (right) [32]. Reprinted with permission, *Physics in Medicine and Biology*, Volume 53, Issue 15, Pages 4205 and 4207 , Figures 1 and 3 (2008).

subcutaneously in mice (Figure 1.6) [52]. Images to depths of up to 10 mm with 100 micron spatial resolution were acquired in a longitudinal manner. This allowed for tumour-related vascular features, such as vessel tortuosity, feeding vessel recruitment, and necrosis to be visualized over time. Acquisition time of each image was approximately 8 minutes.

Unfortunately, these images took several minutes to acquire, thus, they would serve as proficient tools for prostate cancer diagnosis, but would not be suitable for treatment monitoring. The majority of the OA systems recently described in literature, with the ability to image in real time and with the highest resolution and deep penetration used spherical or cylindrical detection geometries [53,54]. For example, Brecht et. al acquired three-dimensional images of a nude mouse using a whole body, small animal scanner with spherical detection geometry [53]. Both kidneys are visualized, along with the spleen and a partial lobe of the liver with spatial resolution of approximately 0.5 mm (Figure 1.7). Kruger et. al. has described a hemispherical detection geometry system for breast cancer detection. Blood vessels were visualized at depths up to 40 mm with spatial resolution of approximately 0.25 mm (Figure 1.8) [54].

These detection geometries are ideal for accurate OA image reconstruction, and provide high contrast and resolution in real time. However, these geometries are constrained by the need for access to all sides of the target. They are not suitable for imaging superficial structures, such as the skin, or if strongly echogenic structures such as bone or lung are situated along the acoustic propagation path [55]. These circumstances

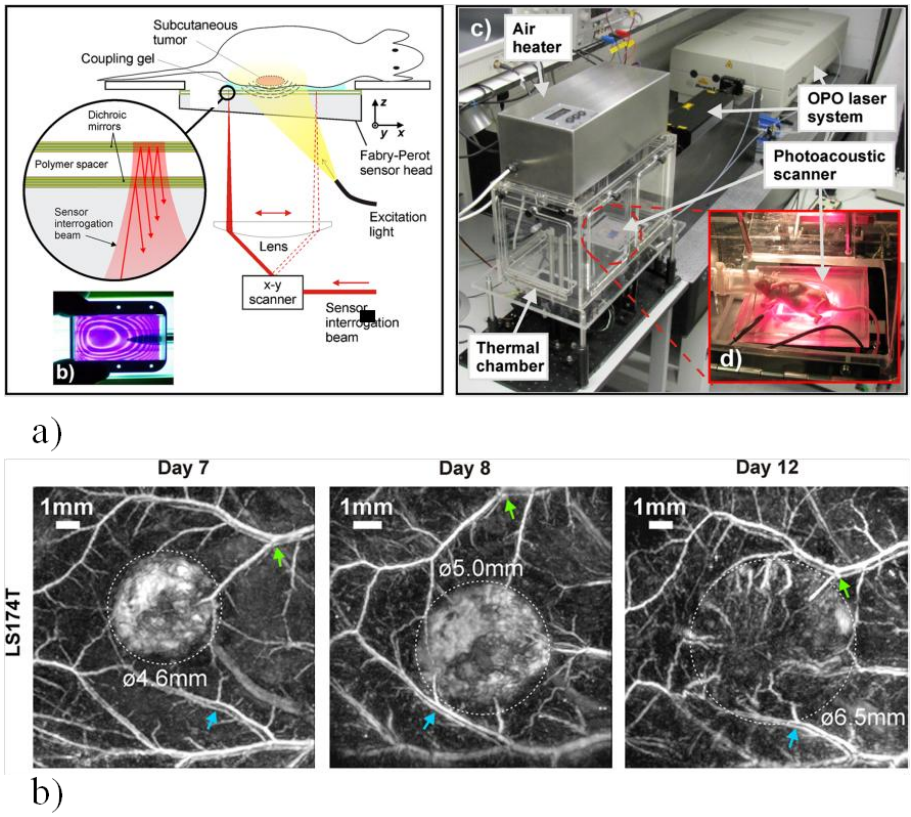

Figure 1.6: a) Schematic of the optoacoustic imaging system used by Laufer et al. (2012) and (right) a photograph of the imaging system showing the system in operation and the anaesthetized animal. b) Optoacoustic images (maximum intensity projections) showing the development of human colorectal tumour LS174T and the surrounding vasculature between day 7 and day 12 post-inoculation. The dashed lines indicate the tumour margins. The arrows show common vascular features in the images [52]. Reprinted with permission, *Journal of Biomedical Optics*, Volume 17, Issue 5, Figures 1 and 4 (2012).

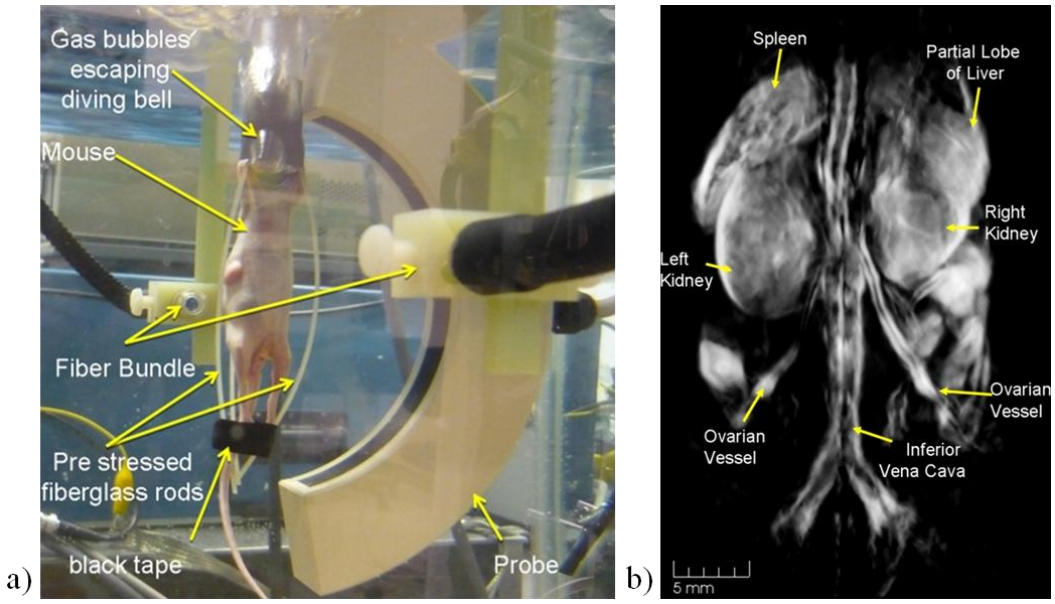

Figure 1.7: Optoacoustic whole body scanner with spherical detection geometry. (a) Experimental set up showing 64 element arc array. (b) Three-dimensional image of a nude mouse acquired using 755 nm illumination [53]. Reprinted with permission, *Journal of Biomedical Optics*, Volume 14, Issue 6, Figures 1 and 6 (2009).

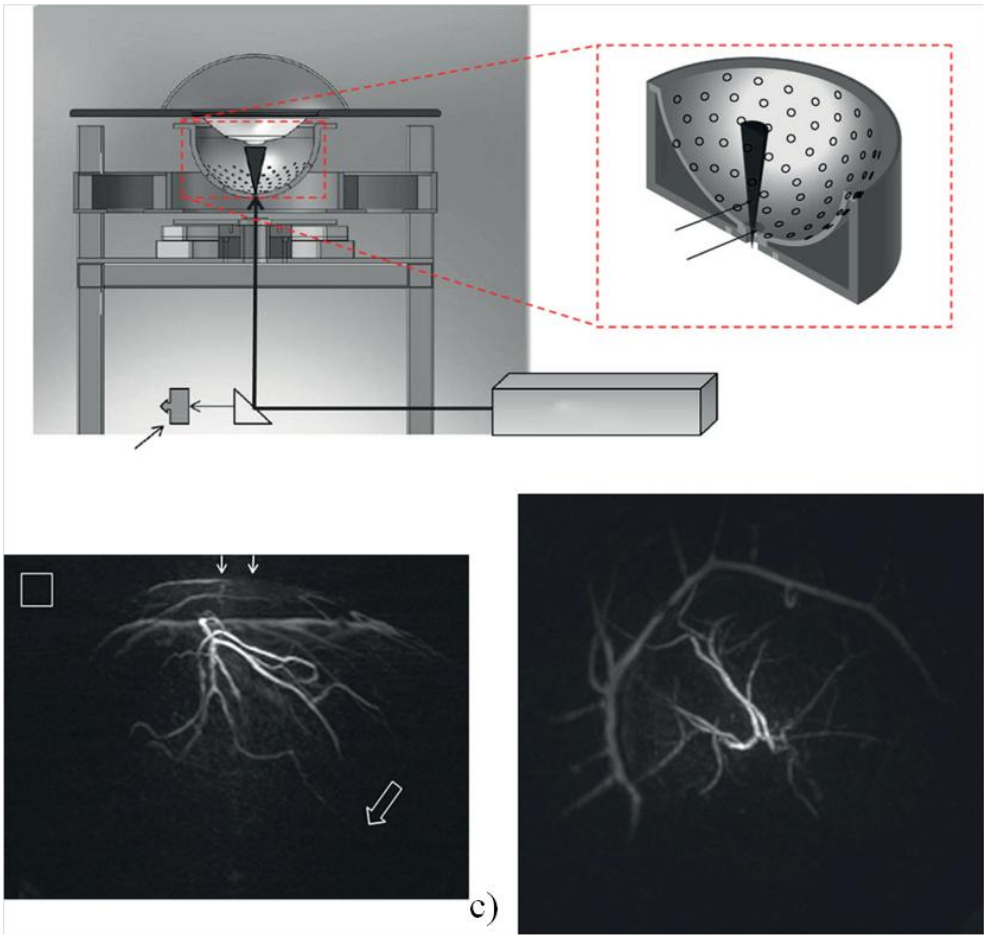

Figure 1.8: Optoacoustic breast imaging system with hemispherical detection geometry. (a) Schematic of the system. (b) Maximum intensity projection of the left breast of a patient (lateral projection) over a 64 x 50 mm^2 field of view. Hollow box represents 1 x 1 mm^2. (c) Orthogonal projection with a field of view of 64 x 64 mm^2. Images were acquired using 800 nm illumination [54]. Reprinted with permission, *Medical Physics,* Volume 37, Issue 11, Pages 6098 and 6099 , Figures 2 and 5 (2010).

call for the more versatile planar detection geometry in which detection is performed over a finite plane using a one or two-dimensional ultrasound array [55]. The OA imaging systems that employ this geometry often resemble conventional ultrasound imaging systems. Often OA imaging instruments may use existing clinical ultrasound scanners, sufficiently modified, so that the RF (radio frequency) acquisition can be triggered by the excitation laser in order to detect OA waves as well as ultrasound echoes [47,56–59]. Co-registration of the OA and ultrasound images are then relatively straightforward. Then absorption-based contrast of the OA image in combination with the morphology based on elasto-mechanical properties in the ultrasound image can provide structural and functional information about the vasculature [55,60].

Although, this type of OA imaging is the most versatile, particularly for clinical use, image quality provided by planar geometry detection rarely matches that of spherical or cylindrical, due to the limited detection aperture [55]. This often limits lateral resolution [55]. Axial resolution is relatively independent of the detection aperture and is limited largely by acoustic attenuation. This discrepancy between the two spatial resolutions leads to an anisotropic spatial point spread function, which introduces artifacts into the images during reconstruction [55].

Real-time optoacoustic imaging has been demonstrated using planar geometry detection to visualize tumours *in vivo* [61]. An example of this is provided in Figure 1.9 showing superimposed ultrasound and optoacoustic B-mode images of a pancreatic tumour in a mouse with spatial resolution greater than 1 mm [61]. As is evident in Figure 1.9, the resolution of these images rarely matches the resolution of images acquired

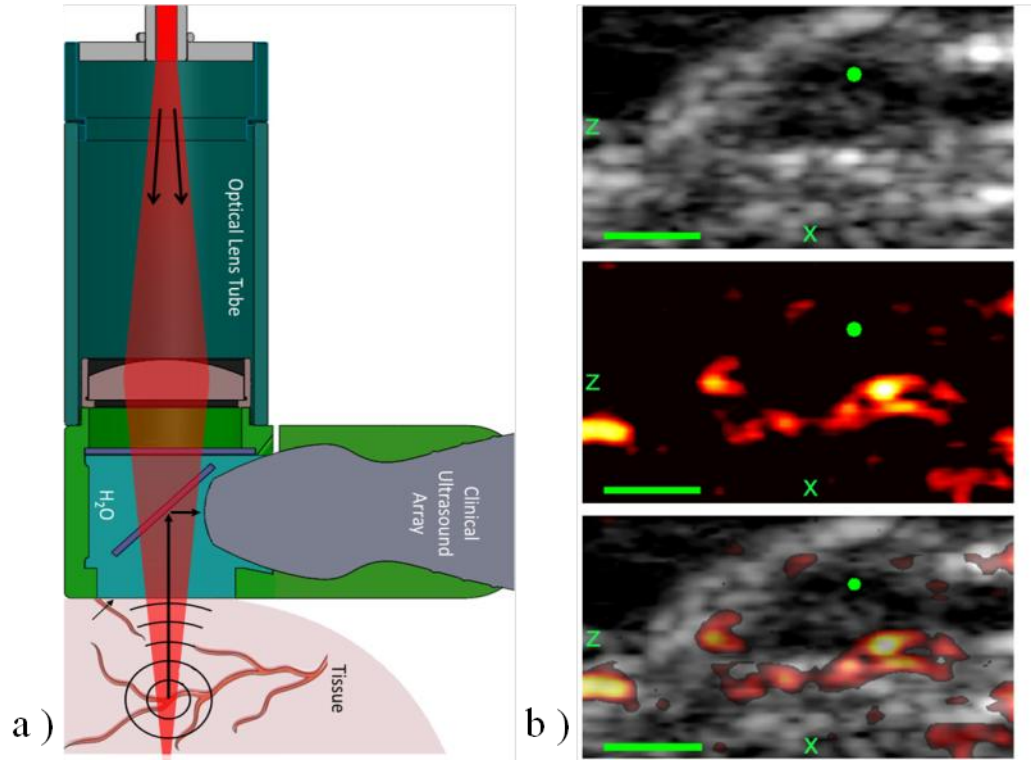

Figure 1.9: Optoacoustic imaging system using conventional ultrasound linear array detection. (a) Cross-sectional view of the optoacoustic imaging system set up using a clinical ultrasound probe providing simultaneous optoacoustic and ultrasound imaging. (b) Ultrasound and optoacoustic images (800 nm illumination) of a tumour (Panc-1 pancreatic cancer cells six weeks after implantation into a mouse) and surrounding regions. Sagittal (x-z) plane (top), optoacoustic image (middle) and superimposed images (bottom). Scale bar denotes 2 mm [61]. Reprinted with permission, *Physics in Medicine and Biology*, Volume 58, Issue 1, Pages N4 and N10 , Figures 2 and 9 (2013).

using a spherical or cylindrical detection system. Three-dimensional, OA images with spatial resolution of approximately 100 μm were acquired using planar detection systems as shown by Laufer et. al. in Figure 1.10 [51]. However, these images necessitate axial and lateral mechanical scanning which consequently increases imaging time (the OA images in Figure 1.10b was acquired in approximately 15 minutes) [51]. Thus imaging time remains a common limiting factor for three-dimensional planar detection systems for clinical use [50,62].

Thus, planar detection geometry, although ideal for clinical use, lacks the necessary resolution or cannot be performed in real time [55]. In order to overcome these limitations, the mechanical scanning speed must be increased (limited, and often itself introduces artifacts) or the resolution of two-dimensional OA images must be improved.

1.5.2 Temperature monitoring

The amplitude of an OA signal is dependent upon the Grüneisen parameter, which increases with temperature, and therefore has been used to monitor temperature changes during LTT [63]. The amplitude is also dependent on the optical absorption properties of the target tissues which provides the opportunity to take advantage of the

significant changes in tissue optical properties, at wavelengths in the visible and near infrared (NIR) range, due to thermal coagulation [63]. Larin et al (2005), demonstrate that during heating of an *ex vivo* canine liver, OA signal amplitude increased at a constant rate to approximately 53°C at which point the amplitude began to increase at an accelerated rate (Figure 1.11). It was hypothesized that this change in slope occurs at the point of

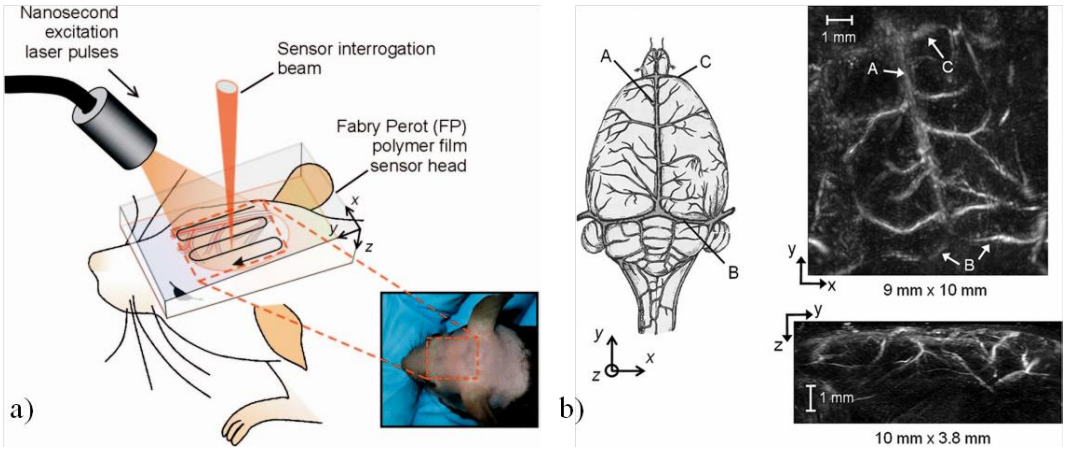

Figure 1.10: Optoacoustic small animal brain imaging system with planar detection geometry . (a) Experimental set up. Excitation laser pulses emitted by a tunable OPO laser system. A second laser emitting at 1550 nm provides a focused interrogation laser beam that is raster scanned over the surface. (b) Optoacoustic images of mouse brain vasculature obtained using 590 nm excitation laser. Left schematic of superficial cerebral vascular anatomy: A, superior sagittal sinus; B, transverse sinus; C, inferior cerebral vein. Top optoacoustic image, x-y maximum intensity projection (MIP), bottom optoacoustic image, y-z MIP. Total imaging time: 15 minutes [51]. Reprinted with permission, *Applied Optics,* Volume 48, Issue 10, Pages D301 and D303 , Figures 1 and 2 (2009).

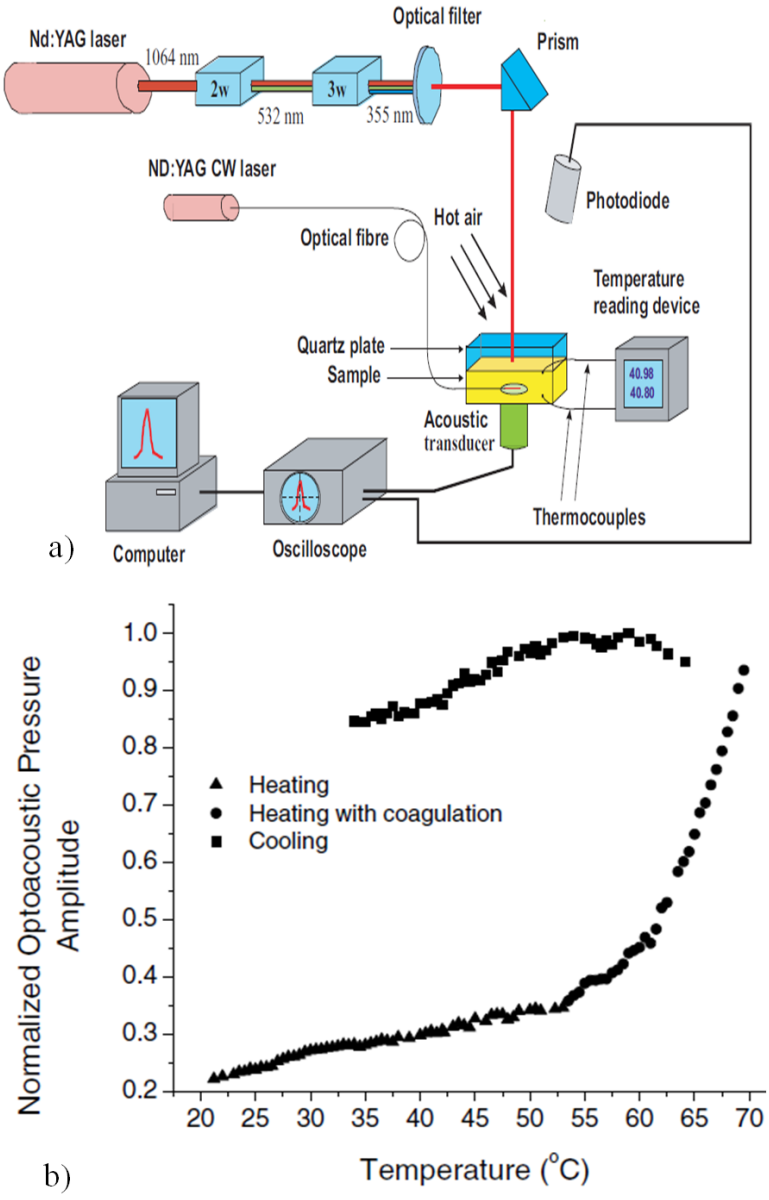

Figure 1.11: Schematic (a) of the optoacoustic imaging system employed by Larin et al. (2005) (b)Amplitude of OA pressure induced in canine liver during conductive heating and passive cooling. The triangles represent heating without coagulation, circles represent heating with coagulation and squares represent cooling of sample [64]. Reprinted with permission, *Journal of Physics - London*, Volume 38, Issue 15, Pages 2647 and 2648 , Figures 1 and 3 (2005).

coagulation [64]. Shah et al. (2008) created thermal maps in *ex vivo* animal tissue and tissue-mimicking phantoms using optoacoustic imaging by monitoring the changes in the OA signal during photothermal therapy (Figure 1.12c) [47]. They found that the OA signal increased as the temperature increased from an initial temperature of 25°C, to 35 °C. This data was compared with ultrasound data acquired simultaneouly and showed that OA contrast to noise ratio (CNR) was 45 ± 5 dB while that of ultrasound was 24 ± 4 dB an almost two-fold increase (Figure 1.12b) [47].

Significant changes in tissue physical properties also arise during coagulation, such as blood vessels constriction, increased optical scattering, and protein unfolding [65]. These changes may influence the frequency content of the OA signals and frequency analysis of these signals may provide additional information about the tissue state (see section 1.6).

1.6 Frequency spectrum analysis

In addition to the amplitude, the frequency content of the OA signals may provide sub-resolution information, making relatively low-resolution OA images more viable for clinical use [66]. This is especially important for system that are confined to planar detection as their resolution is often low (> 0.5 mm) when operating in real time [56]. Even if vascular structures themselves are not resolved in the reconstructed images (reconstruction often loses a great deal of information, particularly the sub-resolution detail [67]), the frequency content of the generated OA signals may be used to identify tissue regions with specific vascular characteristics which may indicate the presence of disease (or other specific tissues). Phantom and simulation studies by Yang

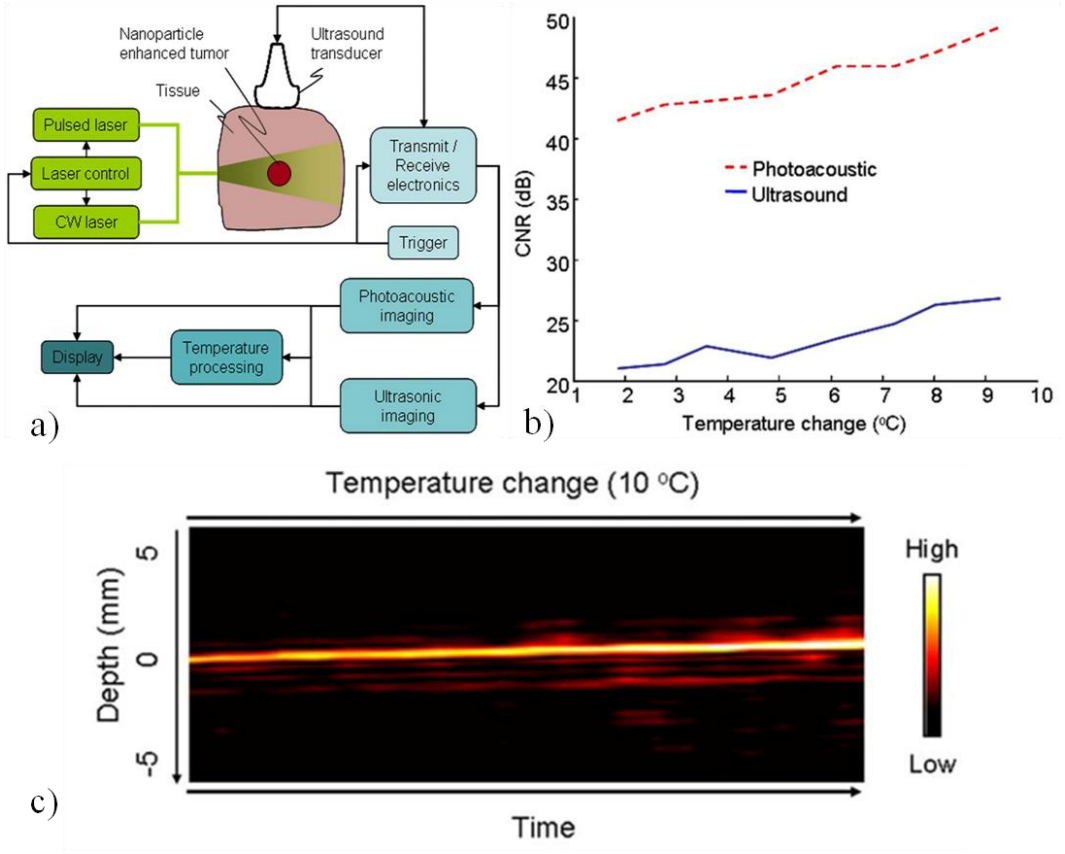

Figure 1.12: Schematic (a) of the optoacoustic set-up used by Shah et al. (2008) (b) Contrast to noise ratios (CNR) of ultrasound and optoacoustic signals during heating indicating that the CNR of both methods increase with temperature and that optoacoustic has a greater CNR than ultrasound in this temperature range. (c) Successive optoacoustic signals plotted for increasing temperature demonstrating that the amplitude increases with temperature [47]. Reprinted with permission, *Journal of Biomedical Optics*, Volume 13, Issue 3, Figures 1 and 4 (2008).

et al (2012), and Xu et al.(2004) have experimentally confirmed the feasibility of discriminating sub-resolution target size and concentrations based on the OA frequency spectrum characteristics [68,69]. This may provide essential information about the target that replaces the need for very high resolution imaging, which is associated with long acquisition times when using planar detection geometry [55].

1.6.1 Ultrasound frequency spectrum analysis

The information content of a transducer's signal is related to the frequency response and the field profile of the transducer [70]. As the number of transducer locations decreases, limiting the system's resolution, the information content from each individual signal remains unchanged. There is significant information with sub-resolution detail contained in each OA signal [71,72]. For example, it is known that the size and concentration of the optical absorber dictates the frequency content of the OA RF signals [73,74]. Work is ongoing to identify how other target characteristics are manifested in the frequency content of the OA signals as well [68,69].

Spectrum analysis of ultrasound RF data and its relation to tissue microstructure has been well described [75]. During the 1970's, means of computing quantitative, calibrated, averaged power spectrum from a region of interest (ROI) were developed, which remove system-specific artifacts, and thus provide quantitative analysis [76]. Analysis of the frequency components of the RF signals has been shown to significantly improve the diagnostic capabilities of conventional ultrasound imaging [11,76].

The size of the scattering structures compared to the wavelength of the incident ultrasound modifies the frequency content of the backscattered signal [77]. Therefore, the

frequency analysis of the ultrasound backscatter RF signals may hold useful information about the sub-resolution structures in tissues. Large databases have been developed, which are used with statistical classifiers to identify specific tissue types from spectral image data [11]. Analysis of the frequency components of the RF signals improves the diagnostic capabilities of conventional ultrasound imaging [11,75,78].

A power spectrum of the RF signals as well as the transducer-specific power spectrum are calculated. The transducer's power spectrum is subtracted from the RF power spectrum to remove any system-dependent features from the analysis [76]. A representative calibrated power spectrum is shown in Figure 1.13 with a linear fit applied between 1 and 6 MHz. The spectral components of the calibrated power spectra (e.g. slope, intercept and midband fit of the linear best fit to the spectral data) are related to the physical characteristics of the target scatterer and are visually depicted in Figure 1.13. Assuming the Born approximation (random scatterer distribution and weak scattering) represents soft tissue scattering, the spectral slope will increase and the spectral intercept will decrease with decreasing size of the scatterer and the midband fit is dependent on the size, shape and acoustic impedance of the scatterer [11]. Differences in spectral components of neoplastic tissue compared with healthy tissue have already been demonstrated for ultrasound RF data [11]. Neoplastic tissues have different microstructure than that of healthy tissue, for example, neoplastic tissues are often denser than normal tissue and consist of more turbulent vasculature [79]. This leads to significant differences in the spectral components associated with neoplastic tissue

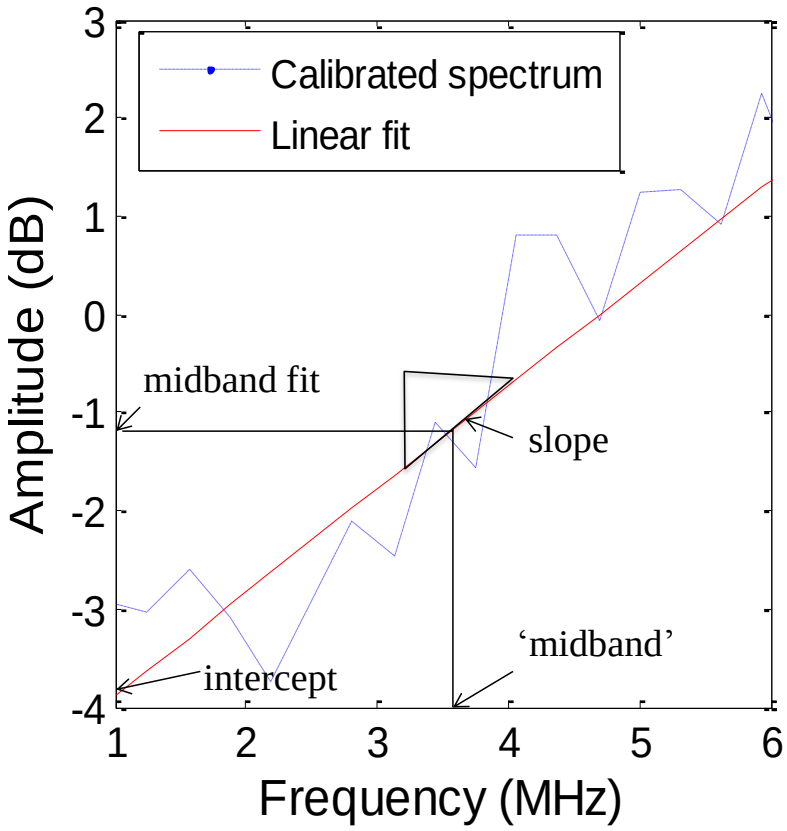

Figure 1.13 A representative calibrated power spectrum with linear fit applied between 1 and 6 MHz. Visual depictions of the midband fit, intercept and slope are presented.

compared to many healthy tissues [80]. Significant changes to ultrasonic spectral components have also been observed during treatment of neoplastic tissue [81].

1.6.2 Optoacoustic frequency spectrum analysis

The frequency content of the generated OA RF signals is broadband and the detected signals are limited by the finite bandwidth of the ultrasound transducers and the frequency dependent attenuation of ultrasound in tissue [73]. Since RF data are collected in OA imaging, and the size of the absorbing structure contributes to the frequency content of the OA signal [13,73], the relationship between the spectral parameters of OA data may also be linked to the physical properties of the target. The midband fit and intercept are directly affected by the amplitude of the signal. Therefore, they will increase as the size and concentration of the absorber increases, since the volume and concentration of the OA targets determine the total optical absorbance and, consequently, the magnitude of the OA signal. Midband fit may be superior to amplitude based on the relative increases of each parameter with change in size and concentration of the target. The slope of the OA frequency spectrum will decrease as the target diameter increases because a target with a larger diameter will theoretically generate a signal with a lower frequency, and this will result in a shift in the signal center frequency towards low frequency [74]. The slope value should not be affected by changes to the target concentration and, thus, should be affected minimally by OA signal amplitude [69].

Using the slope and the midband fit together, size and concentration of OA targets can be inferred. If the OA slope generated from target 'A' is greater than the

slope generated from target 'B' then we can deduce that target 'A' is smaller in size than target 'B'. Therefore, the midband fit generated by target 'A' would be less than that generated by target 'B' at similar concentrations. If the midband fit generated by target 'A' is less than that of target 'B' then the concentration of target 'A' is less than or similar to that of target 'B'. If the midband fit generated from 'A' is greater than that generated from target 'B' then the concentration of 'A' is greater than that of 'B'.

Spectrum analysis of OA RF signals generated by blood vessel phantoms (cylindrical tubes filled with ink and embedded into gelatin) show a relationship between the spectral components and the diameter of the cylinders [74]. Spectrum analysis of high-frequency OA imaging of *ex vivo* ocular tissue has also shown changes in the midband fit and slope around the pigmented iris [82]. Thus, the relationship between the frequency spectrum of OA data is likely linked to the physical properties of the target and, more specifically, the spatial distribution and size of the absorbing targets within the tissues [82].

1.7 Murine models of prostate cancer

Prostate cancer rarely arises spontaneously in animals [83]. Existing prostate cancer models include rodent models, human cell lines, and gene transfer and transgenic models [83]. Only transgenic models provide the spectrum of disease as it occurs in men, including progression from prostate intraepithelial neoplasia (PIN) through androgen-dependence to androgen-independence and metastases [83].

Seventeen human prostate cancer cell lines have been described by Bokhoven et al. (2003) [84]. An issue with cell lines is that they are often derived from metastatic

lesions, therefore they do not allow for genetic alterations that change normal prostate cells into malignant cells to be investigated [84].

Prostate cancer occurs naturally in dogs and resembles the human diseases in terms of characteristics [85], however, it is not androgen dependent in dogs [86]. The high cost, long gestation period and difficulty of genetic manipulation often make dogs an unrealistic model [87]. Several strains of rat also naturally develop prostate cancer including Dunning, Copenhagen and Wistar [88]. However, these tumors are rare, vary in phenotype and lack metastases making them less than ideal as experimental models [87].

The mouse is currently one of the best and most commonly used models of prostate cancer [87]. Although prostate cancer does not occur naturally in mice, they are as susceptible to cancer as humans [89]. The mouse genome is also 95% similar to that of humans and is relatively easy to genetically modify [87]. Finally, mice have short gestation, are relatively small, and easy to house and breed making them a useful candidate for experimental models. Xenograft models are created in immunodeficient mice that are injected with human tumour tissue, or cell cultures [90]. Despite the utility of these models, the major concern is that the compromised immune system, required to allow growth of foreign tissue, may affect tumour progression in these mice [90].

Genetically engineered mouse models of prostate cancer are mice inflicted with genetic modifications equivalent to those associated with the human disease [88]. The first published genetically engineered mouse model was the C3(1)-Tag model in 1994 [88]. This model was created by targeting the expression of the SV40 large tumour antigen (Tag) to the prostate by using a region of the C3(1) gene. Male C3(1)-Tag mice

developed prostatic epithelial hyperplasia as early as 3 months of age, and the majority developed locally invasive tumours by 7-11 months of age. The tumours in this model rarely metastasize [88]. The expression of Tag in this model was not specific to the prostate. Two-thirds of the female mice developed mammary tumours associated with SV40 expression [91]. This strategy of expressing SV40 antigens to the prostate was used in several later models with more effective prostate targeting [87]. The LADY series of models consist of seven transgenic lines which are split into three groups based on when in the life cycle of the mouse neoplasia is attained [92]. The cancer in this model starts as small foci of hyperplasia and then proliferates outwards, followed by dysplasia, prostatic intraepithelial neoplasia (PIN), and finally adenocarcinoma. This represents an ideal model of the stages of human prostate cancer, however, castration resistance and metastasis are not well modeled [87].

1.7.1 Transgenic ardenocarcinoma of mouse prostate (TRAMP) model

The transgenic ardenocarcinoma of mouse prostate (TRAMP) shares many similarities with the human clinical prostate disease. The TRAMP mouse develops spontaneous autochthonous prostate cancer with distant site metastasis and offers a realistic molecular and physical comparison to the human disease [93]. The tumours originate and develop within the prostate gland of the animal. Tumours cannot be palpated or visualized in the animal prior to imaging, unlike many xenograft models. Molecularly, the TRAMP model displays PIN prior to tumour formation [94]. The tumour development begins as androgen-dependent then progresses to androgen-independent similar to the human disease [95]. The major disadvantage with the TRAMP model is that it most often develops cancer with neuroendocrine (NE) origin [96]. Some neuroendocrine

markers are found in the human disease, however, the majority of cells in human prostate cancer are epithelial [87].

Adenocarcinoma is an invasive, malignant neoplasm of the epithelium with glandular formation and lacks the light microscope features of neuroendocrine differentiation [87]. Adenocarcinoma in the human is classified as well, moderation, moderately-poor or poorly differentiated. In genetically engineered mice, the classification scheme is the same excluding moderately-poor differentiated [93]. Well differentiated refers to the majority of the tumour having well-formed glands. Moderately differentiated refers to tumours with mostly glands but some foci mixed in showing gland fusion or solid areas. Poorly differentiated refers to tumours where the invasive foci are mostly nests or solid sheets, but gland formation is still focally seen [97].

1.8 Rational, hypothesis and specific aims

1.8.1 Rationale

Prostate cancer is a common disease among men in developed countries and, fortunately, has a relatively high survival rate provided diagnosis occurs in its early stages [4]. However, detection of the disease in its early stages remains unreliable due to inadequate detection techniques [5]. Furthermore, treatments of early-stage prostate cancer, when diagnosed, are often associated with adverse side effects [21]. New treatment options for early-stage prostate cancer which have minimal to no side effects are available [8], but lack adequate monitoring tools. There is, thus, a growing need for a technique that is capable of diagnosing prostate cancer with high contrast and high

resolution as well as a technique for monitoring these new, preferable prostate cancer treatments.

OA imaging has been demonstrated to acquire high contrast and resolution images in real-time [28]. This thesis addresses one of the major limitations with OA imaging of prostate cancer; the need to use planar detection geometry in prostate imaging, which is often associated with relatively lower resolution when operating in real-time [50,51,55]. Frequency analysis of OA signals, described herein, may offer a means of providing sub-resolution detail to low resolution OA images. This could greatly enhance the applicability of OA imaging in prostate cancer detection and treatment by providing sub-resolution detail about the vasculature of the tumour (which is indicative of its aggressiveness), and physical changes that occur during treatment that indicate successful tumour destruction.

This analytical technique could strengthen all OA imaging applications, especially those systems where the quality of resolution is limited by physical constraints, by providing complementary information to the current amplitude based analysis technique.

1.8.2 Hypothesis

Optoacoustic signal intensity and frequency spectrum are sensitive to physiological differences between healthy and neoplastic tissues, and to treatment-induced physiological changes.

1.8.3 Objectives

The main objectives of the current thesis were:

1. Characterize the system specifications including contrast, resolution and sensitivity to identify optimal image acquisition parameters.

2. Determine the OA image contrast and resolution of prostate tumours in a mouse model *in vivo*.

3. Determine OA frequency analysis when monitoring treatment induced physiological changes in *ex vivo* tissues, which occur during LTT, in real-time.

4. Measure the sensitivity of frequency based analysis of OA signals compared with amplitude based analysis to distinguish targets, and describe the complementary (e.g. subresolution) information that frequency based analysis may offer.

5. Determine the relationship between the OA frequency metrics and biological tissue characteristics, such as size and density of OA targets, through phantoms, computer simulations and *in vivo* experiments.

References

1. Jemal, A. *et al.* Global cancer statistics. *CA: A Cancer Journal For Clinicians* **61**, 69–90 (2011).

2. Siegel, R., Naishadham, D. & Jemal, A. Cancer statistics, 2012. *CA: a cancer journal for clinicians* **62**, 10–29

3. Thompson Jr, I. Long-Term Survival of Participants in the Prostate Cancer Prevention Trial. *New England Journal of Medicine* **368**, 603 (2013).

4. Shah, N. L. & Sanda, M. Health-related quality of life in treatment for prostate cancer: looking beyond survival. *Supportive Cancer Therapy* **1**, 230–236 (2004).

5. el-Gabry, E., Halpern, E. J., Strup, S. E. & Gomella, L. G. Imaging prostate cancer: current and future applications. *Oncology (Williston Park, N.Y.)* **15**, 325–336 (2001).

6. Liu, T. *et al.* A feasibility study of novel ultrasonic tissue characterization for prostate-cancer diagnosis: 2D spectrum analysis of in vivo data with histology as gold standard. *Medical physics* **36**, 3504–3511 (2009).

7. Wijkstra, H., Wink, M. H. & de, la R. Contrast specific imaging in the detection and localization of prostate cancer. *World journal of urology* **22**, 346–350 (2004).

8. Turkbey, B., Pinto, P. A. & Choyke, P. L. Imaging techniques for prostate cancer: implications for focal therapy. *Nature Reviews.Urology* **6**, 191–203 (2009).

9. Robert Ross, M. H. New Clinical Imaging Modalities in Prostate Cancer. *Hematology/oncology clinics of North America* **20**, 811–830 (2006).

10. Mallidi, S., Luke, G. P. & Emelianov, S. Photoacoustic imaging in cancer detection, diagnosis, and treatment guidance. *Trends in biotechnology* **29**, 213–21 (2011).

11. Feleppa, E. J. *et al.* Recent developments in tissue-type imaging (TTI) for planning and monitoring treatment of prostate cancer. *Ultrasonic imaging* **26**, 163–172 (2004).

12. Frederic, L. L., Ernest, J. F., S, K. A. & Cheri, X. D. Ultrasonic spectrum analysis for tissue evaluation. *Pattern Recognition Letters* **24**, 637–658 (2003).

13. Wang, L. V Ultrasound-mediated biophotonic imaging: A review of acousto-optical tomography and photo-acoustic tomography. *Disease markers* **19**, 123–138 (2003).

14. Mamou, J. & Oelze, M. L. *Quantitative Ultrasound in Soft Tissues*. 350 (Springer: 2013).

15. Cheong, W.-F., Prahl, S. A. & Welch, A. J. A review of the optical properties of biological tissues. *SPIE Milestone series* **102**, 129 (1995).

16. Lashkari, B. & Mandelis, A. Comparison between pulsed laser and frequency-domain photoacoustic modalities: signal-to-noise ratio, contrast, resolution, and maximum depth detectivity. *The Review of scientific instruments* **82**, 94903 (2011).

17. Boas, D. A. *et al.* Imaging the body with diffuse optical tomography. *IEEE Signal Processing Magazine* **18**, 57–75 (2001).

18. Podoleanu, A. G. Optical coherence tomography. *Journal of microscopy* **247**, 209–19 (2012).

19. Süzen, M., Giannoula, A. & Durduran, T. Compressed sensing in diffuse optical tomography. *Optics express* **18**, 23676–90 (2010).

20. Sanda, M. G. *et al.* Quality of life and satisfaction with outcome among prostate-cancer survivors. *The New England journal of medicine* **358**, 1250–61 (2008).

21. Eton David T, L. S. J. Prostate cancer and health related quality of life: a review article. *Psychooncology* **11**, 307–326 (2002).

22. Carpentier, A. *et al.* MR-guided laser-induced thermal therapy (LITT) for recurrent glioblastomas. *Lasers in surgery and medicine* **44**, 361–8 (2012).

23. Atri, M., Gertner, M. R., Haider, M. A., Weersink, R. A. & Trachtenberg, J. Contrast-enhanced ultrasonography for real-time monitoring of interstitial laser thermal therapy in the focal treatment of prostate cancer. *Canadian Urological Association Journal = Journal De L'association Des Urologues Du Canada* **3**, 125–130 (2009).

24. Wang, L. V & Hu, S. Photoacoustic tomography: in vivo imaging from organelles to organs. *Science* **335**, 1458–62 (2012).

25. Zhang, E. Z., Laufer, J. G., Pedley, R. B. & Beard, P. C. In vivo high-resolution 3D photoacoustic imaging of superficial vascular anatomy. *Physics in Medicine and Biology* **54**, 1035–1046 (2009).

26. Esenaliev, R. O., Karabutov, A. A. & Oraevsky, A. A. Sensitivity of laser opto-acoustic imaging in detection of small deeply embedded tumors. *IEEE Journal of Selected Topics in Quantum Electronics* **5**, 981 (1999).

27. Oraevsky, A. A. *et al.* Laser optoacoustic imaging of the breast: detection of cancer angiogenesis. *Proceedings - Society of Photo-Optical Instrumentation Engineers* **3597**, 352–363 (1999).

28. Xu, X.-H. & Li, H. Photoacoustic imaging in biomedicine. *Physics - Beijing* **37**, 111–119 (2008).

29. Diebold, G., Sun, T. & Khan, M. Photoacoustic monopole radiation in one, two, and three dimensions. *Physical Review Letters* **67**, 3384–3387 (1991).

30. Gusev, V. E. & Karabutov, A. A. Laser optoacoustics. *NASA STI/Recon Technical Report A* **93**, 16842 (1991).

31. Nachabé, R. *et al.* Effect of bile absorption coefficients on the estimation of liver tissue optical properties and related implications in discriminating healthy and tumorous samples. *Biomedical optics express* **2**, 600–14 (2011).

32. Zhang, H. F., Maslov, K., Sivaramakrishnan, M., Stoica, G. & Wang, L. V. Imaging of hemoglobin oxygen saturation variations in single vessels in vivo using photoacoustic microscopy. *Applied Physics Letters* **90**, 053901 (2007).

33. Ma, Q. & Su, X. Near-infrared quantum dots: synthesis, functionalization and analytical applications. *The Analyst* **135**, 1867–77 (2010).

34. Hebden, J. C., Price, B. D., Gibson, A. P. & Royle, G. A soft deformable tissue-equivalent phantom for diffuse optical tomography. *Physics in medicine and biology* **51**, 5581–90 (2006).

35. Rose, J. L. & Nagy, P. B. Ultrasonic Waves in Solid Media. *The Journal of the Acoustical Society of America* **107**, 1807 (2000).

36. Vellekoop, M. J. Acoustic wave sensors and their technology. *Ultrasonics* **36**, 7–14 (1998).

37. Alkhalifah, T. An acoustic wave equation for anisotropic media. *GEOPHYSICS* **65**, 1239–1250 (2000).

38. Ballantine, D. S. *et al. Acoustic Wave Sensors: Theory, Design, & Physico-Chemical Applications*. 436 (Academic Press: 1996).

39. *Piezoelectric and Acoustic Materials for Transducer Applications*. (Springer US: Boston, MA, 2008).doi:10.1007/978-0-387-76540-2

40. Gualtieri, J. G., Kosinski, J. A. & Ballato, A. Piezoelectric materials for acoustic wave applications. *IEEE Transactions on Ultrasonics, Ferroelectrics and Frequency Control* **41**, 53–59 (1994).

41. Vives, A. A. *Piezoelectric Transducers and Applications*. (Springer Berlin Heidelberg: Berlin, Heidelberg, 2008).doi:10.1007/978-3-540-77508-9

42. Andreev, V. G., Karabutov, A. A. & Oraevsky, A. A. Detection of ultrawide-band ultrasound pulses in optoacoustic tomography. *IEEE Transactions on Ultrasonics, Ferroelectrics and Frequency Control* **50**, 1383–1390 (2003).

43. Xu, Y., Wang, L. V, Ambartsoumian, G. & Kuchment, P. Reconstructions in limited-view thermoacoustic tomography. *Medical physics* **31**, 724–33 (2004).

44. Passler, K., Nuster, R., Gratt, S., Burgholzer, P. & Paltauf, G. Piezoelectric annular array for large depth of field photoacoustic imaging. *European Conferences on Biomedical Optics* **2**, 809012–809012–7 (2011).

45. Worthington, A. ., Trachtenberg, J. & Sherar, M. . Ultrasound properties of human prostate tissue during heating. *Ultrasound in Medicine & Biology* **28**, 1311–1318 (2002).

46. Sarntinoranont, M., Rooney, F. & Ferrari, M. Interstitial Stress and Fluid Pressure Within a Growing Tumor. *Annals of Biomedical Engineering* **31**, 327–335 (2003).

47. Shah, J. *et al.* Photoacoustic imaging and temperature measurement for photothermal cancer therapy. *Journal of Biomedical Optics* **13**, 34024 (2008).

48. Laufer, J. *et al.* In vivo longitudinal photoacoustic imaging of subcutaneous tumours in mice. *Proceedings of SPIE* **7899**, 789915 (2011).

49. Lao, Y., Xing, D., Yang, S. & Xiang, L. Noninvasive photoacoustic imaging of the developing vasculature during early tumor growth. *Physics in Medicine and Biology* **53**, 4203–4212 (2008).

50. Hu, S. & Wang, L. V Photoacoustic imaging and characterization of the microvasculature. *Journal of Biomedical Optics* **15**, 11101 (2010).

51. Laufer, J., Zhang, E., Raivich, G. & Beard, P. Three-dimensional noninvasive imaging of the vasculature in the mouse brain using a high resolution photoacoustic scanner. *Applied Optics* **48**, D299–D306 (2009).

52. Laufer, J. *et al.* In vivo preclinical photoacoustic imaging of tumor vasculature development and therapy. *Journal of biomedical optics* **17**, 056016 (2012).

53. Brecht, H.-P. *et al.* Whole-body three-dimensional optoacoustic tomography system for small animals. *Journal of biomedical optics* **14**, 064007

54. Kruger, R. A., Lam, R. B., Reinecke, D. R., Del Rio, S. P. & Doyle, R. P. Photoacoustic angiography of the breast. *Medical Physics* **37**, 6096–100 (2010).

55. Beard, P. Biomedical photoacoustic imaging. *Interface focus* **1**, 602–31 (2011).

56. Niederhauser, J. J., Jaeger, M., Lemor, R., Weber, P. & Frenz, M. Combined ultrasound and optoacoustic system for real-time high-contrast vascular imaging in vivo. *IEEE Transactions on Medical Imaging* **24**, 436–440 (2005).

57. Kruger, R. A., Kiser, W. L., Reinecke, D. R. & Kruger, G. A. Thermoacoustic computed tomography using a conventional linear transducer array. *Medical physics* **30**, 856–60 (2003).

58. Fronheiser, M. P. *et al.* Real-time optoacoustic monitoring and three-dimensional mapping of a human arm vasculature. *Journal of biomedical optics* **15**, 021305

59. Aguirre, A. *et al.* Coregistered three-dimensional ultrasound and photoacoustic imaging system for ovarian tissue characterization. *Journal of biomedical optics* **14**, 054014

60. Zhang, C., Maslov, K. & Wang, L. V Subwavelength-resolution label-free photoacoustic microscopy of optical absorption in vivo. *Optics Letters* **35**, 3195–3197 (2010).

61. Montilla, L. G., Olafsson, R., Bauer, D. R. & Witte, R. S. Real-time photoacoustic and ultrasound imaging: a simple solution for clinical ultrasound systems with linear arrays. *Physics in medicine and biology* **58**, N1–12 (2013).

62. Emelianov, S. *et al.* Intravascular ultrasound and photoacoustic imaging. *Conference proceedings : IEEE Engineering in Medicine and Biology Society. Conference* **2008**, 2–5 (2008).

63. Whelan, W. M., Davidson, S. R., Chin, L. C. & Vitkin, I. A. A Novel Strategy For Monitoring Laser Thermal Therapy Based on Changes in Optothermal Properties of Heated Tissues. *International Journal of Thermophysics* **26**, 233–241 (2005).

64. Larin, K. V, Larina, I. V & Esenaliev, R. O. Monitoring of tissue coagulation during thermotherapy using optoacoustic technique. *Journal of Physics- London* **38**, 2645–2653 (2005).

65. Barton, J. K. *et al.* Photothermal coagulation of blood vessels: a comparison of high-speed optical coherence tomography and numerical modelling. *Physics in medicine and biology* **46**, 1665–78 (2001).

66. Kumon, R. E., Deng, C. X. & Wang, X. Frequency-Domain Analysis of Photoacoustic Imaging Data From Prostate Adenocarcinoma Tumors in a Murine Model. *Ultrasound in medicine & biology* **37**, 834–839 (2011).

67. Noble, J. A. Ultrasound image segmentation and tissue characterization. *Engineering in medicine* **224**, 307–16 (2010).

68. Yang, Y., Wang, S., Tao, C., Wang, X. & Liu, X. Photoacoustic tomography of tissue subwavelength microstructure with a narrowband and low frequency system. *Applied Physics Letters* **101**, 034105 (2012).

69. Xu, G. *et al.* Photoacoustic spectrum analysis for microstructure characterization in biological tissue: A feasibility study. *Applied physics letters* **101**, 221102 (2012).

70. Zalev, J. & Kolios, M. C. Detecting abnormal vasculature from photoacoustic signals using wavelet-packet features. *Proceedings of SPIE* 78992M (2011).

71. Candes, E. J., Romberg, J. & Tao, T. Robust uncertainty principles: exact signal reconstruction from highly incomplete frequency information. *IEEE Transactions on Information Theory* **52**, 489–509 (2006).

72. Provost, J. & Lesage, F. The Application of Compressed Sensing for Photo-Acoustic Tomography. *IEEE Transactions on Medical Imaging* **28**, 585–594 (2009).

73. Diebold, G. J., Beveridge, A. C. & Hamilton, T. J. The photoacoustic effect generated by an incompressible sphere. *The Journal of the Acoustical Society of America* **112**, 1780–1786 (2002).

74. Gertsch, A. G., Bush, N. L., Birtill, D. C. C. & Bamber, J. C. Toward characterizing the size of microscopic optical absorbers using optoacoustic emission spectroscopy. *BiOS* 75641M–75641M–10 (2010).

75. Lizzi, F. L. *et al.* Ultrasonic spectrum analysis for tissue assays and therapy evaluation. *International Journal of Imaging Systems & Technology* **8**, 3–10 (1997).

76. Lizzi, F. L., Greenebaum, M., Feleppa, E. J., Elbaum, M. & Coleman, D. J. Theoretical framework for spectrum analysis in ultrasonic tissue characterization. *The Journal of the Acoustical Society of America* **73**, 1366–1373 (1983).

77. Kolios, M. Biomedical ultrasound imaging from 1 to 1000 MHz. *Canadian Acoustics* **37**, 35–43 (2009).

78. Lizzi, F. L., Astor, M., Feleppa, E. J., Shao, M. & Kalisz, A. Statistical framework for ultrasonic spectral parameter imaging. *Ultrasound in medicine & biology* **23**, 1371–1382 (1997).

79. Mucci, L. A., Powolny, A. & Giovannucci, E. Prospective Study of Prostate Tumor Angiogenesis and Cancer-Specific Mortality in the Health Professionals Follow-Up Study. *Journal of Clinical Oncology* **27**, 5627–5633 (2009).

80. Saha, R. K. & Kolios, M. C. A simulation study on photoacoustic signals from red blood cells. *The Journal of the Acoustical Society of America* **129**, 2935–2943 (2011).

81. Banihashemi, B. *et al.* Ultrasound imaging of apoptosis in tumor response: novel preclinical monitoring of photodynamic therapy effects. *Cancer research* **68**, 8590–8596 (2008).

82. Silverman, R. H. *et al.* Spectral parameter imaging for detection of prognostically significant histologic features in uveal melanoma. *Ultrasound in Medicine & Biology* **29**, 951–959 (2003).

83. Russell, P. J. & Voeks, D. J. Animal models of prostate cancer. *Methods in molecular medicine* **81**, 89–112 (2003).

84. van Bokhoven, A. *et al.* Molecular characterization of human prostate carcinoma cell lines. *The Prostate* **57**, 205–25 (2003).

85. Rosol, T. J., Tannehill-Gregg, S. H., LeRoy, B. E., Mandl, S. & Contag, C. H. Animal models of bone metastasis. *Cancer* **97**, 748–57 (2003).

86. Winter, S. F., Cooper, A. B. & Greenberg, N. M. Models of metastatic prostate cancer: a transgenic perspective. *Prostate cancer and prostatic diseases* **6**, 204–11 (2003).

87. Valkenburg, K. C. & Williams, B. O. Mouse models of prostate cancer. *Prostate cancer* **2011**, 895238 (2011).

88. Maroulakou, I. G., Anver, M., Garrett, L. & Green, J. E. Prostate and mammary adenocarcinoma in transgenic mice carrying a rat C3(1) simian virus 40 large tumor antigen fusion gene. *Proceedings of the National Academy of Sciences of the United States of America* **91**, 11236–40 (1994).

89. Rangarajan, A. & Weinberg, R. A. Opinion: Comparative biology of mouse versus human cells: modelling human cancer in mice. *Nature reviews. Cancer* **3**, 952–9 (2003).

90. Pienta, K. J. *et al.* The current state of preclinical prostate cancer animal models. *The Prostate* **68**, 629–39 (2008).

91. Yoshidome, K. *et al.* Genetic alterations in the development of mammary and prostate cancer in the C3(1)/Tag transgenic mouse model. *International Journal of Oncology* **12**, 449–502 (1998).

92. Kasper, S. *et al.* Development, progression, and androgen-dependence of prostate tumors in probasin-large T antigen transgenic mice: a model for prostate cancer. *Laboratory investigation; a journal of technical methods and pathology* **78**, i–xv (1998).

93. Gingrich, J. R. *et al.* Metastatic prostate cancer in a transgenic mouse. *Cancer research* **56**, 4096–4102 (1996).

94. Gingrich, J. R., Barrios, R. J., Foster, B. A. & Greenberg, N. M. Pathologic progression of autochthonous prostate cancer in the TRAMP model. *Prostate Cancer & Prostatic Diseases* **2**, 70 (1999).

95. Eng, M. H. *et al.* Early castration reduces prostatic carcinogenesis in transgenic mice. *Urology* **54**, 1112–1119 (1999).

96. Chiaverotti, T. *et al.* Dissociation of epithelial and neuroendocrine carcinoma lineages in the transgenic adenocarcinoma of mouse prostate model of prostate cancer. *The American journal of pathology* **172**, 236–46 (2008).

97. Fukumura, D., Yuan, F., Monsky, W. L., Chen, Y. & Jain, R. K. Effect of host microenvironment on the microcirculation of human colon adenocarcinoma. *The American Journal Of Pathology* **151**, 679–688 (1997).

CHAPTER 2

OPTOACOUSTIC IMAGING SYSTEM CHARACTERIZATION

"Not only is the Universe stranger than we think, it is stranger than we can think."

-Werner Heisenberg (1901-1976)
picture from http://www.goodreads.com/author/show/64309.Werner_Heisenberg

2.1 Introduction

The optoacoustic (OA) imaging system used in this study is a prototype system purchased from SENO Medical Instruments Inc. (San Antonio, TX). Full characterization of the system had not been accomplished prior to this work. The system is one of only three similar SENO prototype systems in the world and, therefore, has not been thoroughly characterized in literature. Knowledge of the imaging system-dependent features is imperative in order to correctly analyze the detected signals. In order to properly set up experiments and have confidence in the results, it is important to understand the capabilities and limitations of any imaging system. Specifically; its sensitivity, reproducibility, image accuracy and contrast [1]. These characteristics aid in determining such things as sample size, necessary target characteristics (i.e. size, composition, etc.) to optimize detection, and required recalibrations between acquisitions.

The phantom studies described in this chapter were performed to gather such information and provide a basic reference of the system's response to target characteristics, so as to aid in the analysis of more complex data in the following chapters.

2.1.1 Optoacoustic wave generation

Theoretically, the OA signal increases linearly with increasing absorption coefficient of the target as describe by the equation below [2].

$$\Delta P = \mu_a \Gamma \Phi \qquad [1]$$

where μ_a is the absorption coefficient of the target, Γ is the Grűneisen parameter which is dependent on several physical characteristics of the target (e.g. thermomechanical

properties, stiffness, etc.) , and Φ is the laser fluence (i.e. energy delivered per unit area) [3,4].

Absorption coefficients of different biological tissues and fluids often vary more drastically than the differences between their Grüneisen parameter, allowing OA imaging to differentiate among tissue types based on their absorption [5]. This study focuses on absorption coefficients for rodent tissues/organs. Examples of published absorption coefficients in different tissues are presented in Table 2.1, and range between approximately 0.2 and 0.6 cm^{-1}.

2.1.2 Sensitivity, theory validation and reproducibility

Sensitivity describes the minimum signal that the system can detect above background noise. In biological tissues, the primary determent of OA wave strength is the absorption coefficient. Therefore, the sensitivity can be determined by finding the target with the minimum absorption coefficient which can be detected by the OA system.

The theoretical relationship between the absorption coefficient of a target and the generated OA signal was validated. This was accomplished by comparing the average signal strength of a target to the theoretical signal strength of that target. The repeatability (or precision) of a system, is the degree to which repeated measurements show the same results [6]. The repeatability may be described by the variation in the OA signal strengths associated with a target which was imaged numerous times under unchanged conditions.

Table 2.1: Absorption coefficients in mouse tissues [7–9].

Tissue	**Wavelength (nm)**	**Absorption coefficient (cm^{-1})**
Mouse Muscle	700	0.23
Mouse Lung	700	0.35
Mouse Heart	700	0.11
Mouse Liver	700	0.45
Mouse Kidney	700	0.12
Mouse Stomach	700	0.21
Blood (oxygenated)	780/1064	0.35/0.30
Blood (de-oxygenated)	780/1064	0.60/0.05
Mouse skin	1064	0.20
Mouse Spleen	1064	0.18
Human prostate	786	0.30

2.1.3 Optoacoustic image accuracy

Optoacoustic resolution is largely affected by the frequency and geometry of the detection transducer. The transducer of the SENO OA system is an annular array transducer consisting of eight concentric piezoelectric ring sensors (See Section 1.4). The achievable resolution of each transducer in the array is dependent upon the depth, z, of the optoacoustic source, as well as on the diameter and width of the transducer [10]. Resolution is the minimum distance between two objects that a system can still determine the targets as separate [11]. The SENO OA system is a low resolution system due to the transducer characteristics and its central frequency of 5 MHz, however, for this study we are interested in its ability to accurately predict target size (i.e. its accuracy). Accuracy is defined as the ability of the system to accurately predict target size.

2.1.4 Optoacoustic image contrast

Contrast is defined as the difference between the signal strength on target compared with surrounding signal [12]. The variation among the Grüneisen parameters of biological tissues, at wavelengths of the SENO OA system (775 and 1064 nm) and at body temperature (38 °C in rodents), are minimal compared to variations in their optical absorption properties[1,13]. Contrast in tissue is, thus, driven largely by optical absorption. Understanding the relationship between the generated signal amplitude and the target's optical absorption will allow for the prediction of the contrast that can be achieved in different tissues/organs compared with surrounding tissues (based on their published absorption coefficients) [1].

2.1.5 Tissue-mimicking phantoms

When testing a system's performance, the use of *in vivo* or *ex vivo* tissue samples is ideal. However, the use of tissue is often impractical for testing significant issues with respect to the intrinsic performance of the device (signal, detector and processing precision and repeatability). A highly reliable alternative is the use of tissue-mimicking phantoms. Although phantoms do not reflect the complexity of tissue, they provide an accurate way of testing parameters and modeling and evaluating theoretical assumptions of important tissue features, such as optical absorption and scattering.

Over the past few decades many different types of phantoms have been developed for OA imaging, each with their advantages and disadvantages [8,14]. The composition of the optimal phantom depends on its intended use and the physical and biological characteristics to be mimicked. In laboratory use, the most common phantom materials are; gelatin [15], agar [16], polyester [17], epoxy [18] and resin [19]. These materials provide a soft medium which is biologically and biochemically comparable with organic molecules [19]. Alone, these materials have minimal scattering and absorption coefficients, therefore absorbing and scattering materials may be added to the phantom during preparation [17].

The OA wave generated is affected by the absorption coefficient, scattering coefficient, anisotropy coefficient, and mechanical and surface properties [3]. Therefore, it is imperative that these characteristics of the phantom can be varied to mimic those of *in vivo* tissues at the wavelengths of interest (i.e. 775 nm and 1064 nm). The mechanical and surface properties should be similar to those of tissue (e.g. Young's modulus between 0.35 to 3.15 kPa) [20], and the optical properties (absorption and scattering coefficients) can be chosen to mimic a 'generic' overlaying tissue. Of the

phantom materials presented, gelatin and agar have the most similar acoustic and mechanical properties to tissues [15,16]. The OA target (mimicking the optical properties of the biological target) can then be embedded into the phantom material.

2.1.6 Optical scatters and absorbers

The most common scatterers are titanium dioxide (TiO_2) particles, lipid-based scatterers (e.g. milk, intralipid, etc.), and polymer microspheres [17]. Titanium dioxide is available at a relatively low cost (compared with some lipid-based and microsphere scatterers) [17], and is the most commonly used scatterer due to its wide availability . The main disadvantage of TiO_2 is its powder form that can settle quickly in liquid phantoms [17]. Intralipid (fat emulsion of soy bean oil, egg phospholipids, glycerin and water) is a common lipid-based scatterer which is slightly more expensive than TiO_2, however it provides better reproducibility than TiO_2 [21]. Intralipid also disperses easier making for a more homogeneous phantom.

Polymer microparticles are biologically similar to tissue scatterers. They are also very common and provide a scattering material which is highly reproducible [17]. Their main disadvantage is their high cost compared with other scatterers. A summary of the benefits and limitations of commonly used scatterers is presented in Table 2.2.
The addition of absorbers can provide the phantom with specific absorption coefficients which is essential for mimicking tissues. The most common choice of absorbers are ink and hemoglobin [22]. Black Pelikan ink is a common absorber as it has negligible scattering and provides a simplistic way of obtaining an almost constant absorption spectra within the wavelength range of 700-1100 nm [21,23]. Hemoglobin provides a more realistic tissue

Table 2.2: Advantages and disadvantages of common scatterers used in optoacoustic phantom construction.

Scatterer	**Advantages**	**Disadvantages**
Milk (lipid-based)	Readily available	Not highly reproducible between samples
Oil/fat/lipid (lipid-based)	Readily available	Must be emulsified. Blended reproducibly
Intralipid (lipid-based)	Reproducible source of lipid solution.	Relatively high cost compared with other lipid-based scatterers
Polymer microspheres	Provide stable and precise scattering	High cost compared with other scatterers
Titanium dioxide	Readily available. Provides calibrated scattering	Settling often occurs

absorption spectrum; however, it does not offer a constant absorption spectrum. Its absorption varies significantly between wavelengths within 700-1100 nm.

In this study, the characteristics and capabilities of the OA system are investigated. Knowledge of the system-dependent characteristics, namely the sensitivity and repeatability, will allow for optimal imaging protocols to be constructed for this system. Furthermore, knowledge of the image contrast and accuracy will aid in understanding and quantifying the generated OA signals from more complex tissue targets.

2.2 Materials and Methods

2.2.1 Optoacoustic image acquisition

The imaging system (Seno Medical Instruments Inc., San Antonio, TX) consists of an Nd:YAG pumped Ti:Sapphire laser operating at 775 nm and an 8 element concentric annular array piezoelectric transducer (Figure 2.1). The piezo-electric detection system consisting of 8 elements offers dynamic focusing capabilities which leads to a reduction in image artifacts compared to spherical detectors, and allows for structures lying on the axis within a wide depth range to be localized [10,24].

The transducer has a nominal central frequency of 5 MHz, with a -6dB bandwidth of 60%, a focal point at 25 mm, a focal length of 10 mm, and a focal width of 0.5 mm. The bifurcated optical fiber bundle delivered 6 ns pulses at a 10 Hz repetition rate and 20 mJ of energy per pulse. The step size was chosen to produce the optimal lateral accuracy (directly related to step size) while maintaining a reasonable acquisition time (directly related to step size). A constant TGC was used to ensure that comparisons

a)

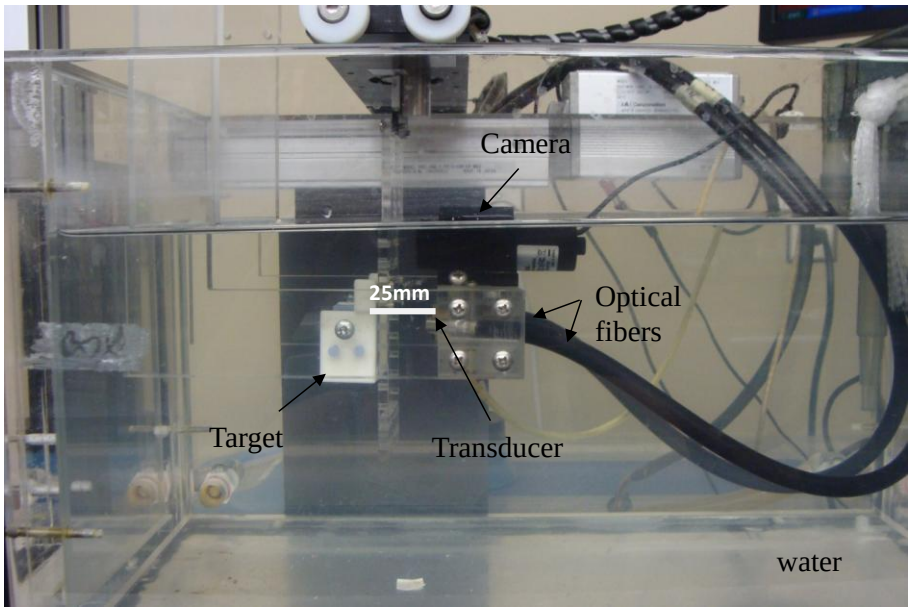

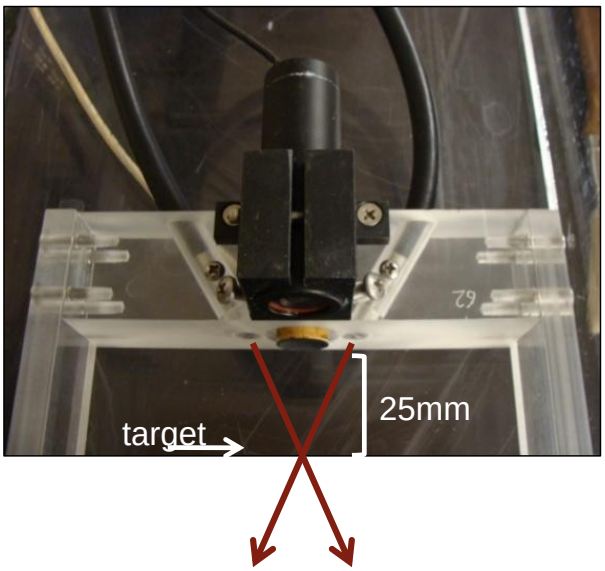

b)

Figure 2.1: Seno optoacoustic imaging system a) side view, b) top-down view. Laser optical path intercepts at 25 mm from the transducer which is located beneath a camera used for image positioning.

among images would be reliable. A laser fluence of 0.2 W/cm^2 was chosen to reflect a relative energy used *in vivo* which would allow for optical penetration depth of over 1 cm [25,26], while remaining within the American National Standards Institute (ANSI) guidelines [27].

2.2.2 Optoacoustic image contrast

The Grüneisen parameter and the laser fluence were kept constant by using the same thin walled glass tubes for each of the targets, and constant laser energy during all experiments. Therefore, the variation in the OA signal amplitude was affected only by the variation in the absorption coefficient of the target.

Black Pelikan ink (Pelikan 4001, Brilliant-Schwarz) was added to distilled water in varying concentrations to obtain solutions with specific absorption coefficients. A cuvette was filled with the solution and the absorbance (or transmittance) was measured using a spectrometer (Spectronic 20D, Thermo Fisher Scientific Inc, Wisconsin USA) according to the manufacturer's instructions. The absorption coefficient (which is wavelength dependent) was calculated using the Beer-Lambert Law.

$$A_\lambda = l c_c \varepsilon_\lambda \qquad [2]$$

Where A_λ is the absorbance (measured by the spectrometer), l is the path length of the spectrometer (1 cm), c_c is the concentration of the solution, and ε_λ is the molar extinction coefficient. The absorption coefficient is the product of the molar extinction coefficient and the concentration. Dye was added until the absorption coefficient of the solution reached the desired level. The uncertainty in the spectrometer reading is ±10% [28].

Thin walled glass tubes (3 mm diameter and 0.01 mm wall thickness; Charles Supper Company, MA) were filled with solution and secured vertically on a holder in the OA system water tank. Images of a 5 mm x 5 mm area, centered on each tube, were obtained (Figure 2.2). Contrast was defined as the average signal amplitude within a 1.5 mm x 1.5 mm region of interest (ROI) centered on the tube compared to two 0.75 mm x 1.5 mm ROI's (for a total ROI size of 1.5 mm x 1.5 mm) 0.25 mm from the edge of each side the tube.

2.2.3 Theory validation and repeatability

The tubes contained solutions of varying absorption coefficients (0.3, 0.4, 0.5, 0.6, 0.7, 0.8 and 0.9 cm^{-1}). Theoretically, OA signals would increase linearly with increasing absorption coefficient (assuming the other parameters were unchanged). Therefore, the theory was validated by measuring the linearity of the signals versus the absorption coefficients (i.e. R^2, the coefficient of determination) [29]. Measurements were performed three times each day for three days (for a total of nine repetitions to investigate the system repeatability) for each absorption coefficient. Based on power analysis, this replication rate was estimated to achieve sufficient power [30]. At the end of each of the three days the system and laser were shut off. The solutions were mixed on the first day and kept in sealed glass containers that were stored in a light-proof box to diminish optical degradation of the solutions by ambient light [31].

To investigate the effect of target size, a subset of these measurements were performed using 5 mm diameter, thin walled glass tubes filled with the same solutions. To examine the effect of overlaying tissue, identical tubes were also embedded into tissue-mimicking phantoms.

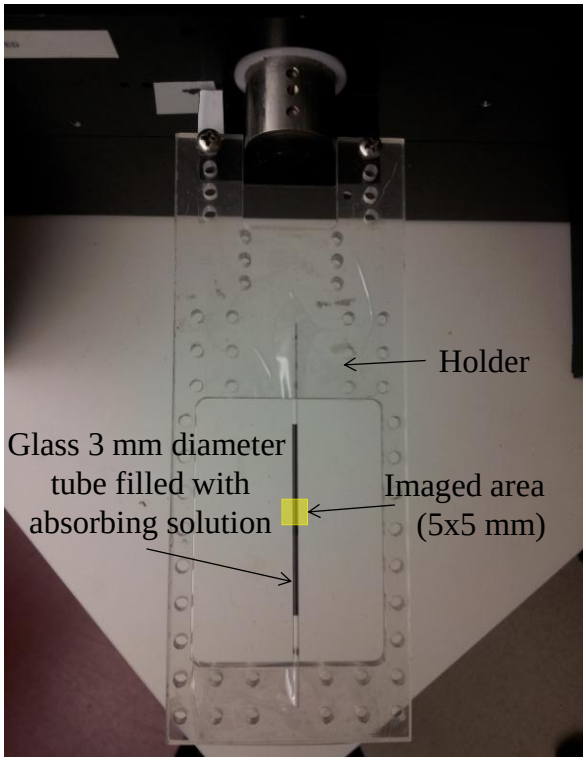

Figure 2.2: A glass tube (3mm diameter) filled with an absorbing solution and secured to a holder which will be placed into the OA imaging system waterbath during image acquisition. Images of a 5 mm by 5 mm area, centered on the tube and extending 1 mm off the sides of the tube, were obtained.

2.2.4 Distance-from-transducer

The "distance from transducer" that a target is positioned is very important when using a focused transducer and can have a great affect on the above-mentioned parameters. A focused transducer is more sensitive to signals originating closer to its focal point (at 25 mm for our system). The signal variation with target distance from the transducer was investigated by measuring the maximum OA signal amplitude obtained from a tube filled with a solution with a 0.6 cm^{-1} absorption coefficient at three distances from the transducer (20, 25, and 30 mm). These images were acquired in immediate succession. This was repeated three times on three consecutive days for a total of 9 images at each distance. Based on power analysis, this replication rate was estimated to achieve sufficient power [30].

2.2.5 Tissue-mimicking phantoms

Tissue-mimicking phantoms were constructed using gelatin derived from porcine skin (Sigma-Aldrich Co., St. Louis, MO). Gelatin is one of the most commonly used phantom materials for ultrasound and spectroscopy imaging system characterization and calibration [19,32].

Table 2.1 describes the large variation among published absorption and scattering coefficients in biological tissues [8]. However, since the aim of the phantom produced in this study was to mimic a 'representative' soft tissue in a rodent, these values were used to assist in the development of phantom parameters. Phantoms were designed to optically mimicked mouse skin and muscle tissue which have averaged published absorption and scattering coefficients of 0.2 cm^{-1} and 10 cm^{-1} respectively at 775 nm, and approximately 0.2 cm^{-1} and 20 cm^{-1} at 1064 nm [8].

2.2.6 Gelatin Phantom Preparation

Two hundred milliliters of water was placed in a 1000 mL beaker, and covered with a glass plate to reduce evaporation. A hotplate was used to bring the water to approximately 80^{o}C and maintain that temperature during mixing. One ml of Pelikan black ink was added to the water and allowed to stir for several minutes. Intralipid 20% (10 mL; Signal-Aldrich Co., Oakville, ON) was then slowly added to the mixture and stirring continued for a minimum of 10 minutes to ensure homogeneity of intralipid throughout the solution during solidification. Twenty grams of Knox® gelatin was slowly added to the solution. The solution stirred until the gelatin was fully dissolved (about 10 minutes). The temperature of the hotplate was reduced to 25 °C. The gelatin solution was then poured into 4 cm by 4 cm by 2 cm square moulds. The moulds were kept at 4^{o}C overnight [23].

Thin-walled, 3 mm diameter glass tubes were filled with an absorbing solution of ink in water, with an absorption coefficient of 0.8 ± 0.1 cm^{-1} at 775 nm (mimicking highly absorbing biological tissue, such as a tumour) [8]. Tubes were secured into the moulds at the desired depths, 0 mm (surface), 3 mm and 5 mm, and the liquid gelatin solution was then poured into the mould. Once solidified, phantoms were removed from the moulds (Figure 2.3), placed in air-tight bags, and stored at 4^{o}C for up to 3 days. Images of the embedded tubes were acquired using the same imaging parameters and protocol as was used for the un-embedded tubes described in section 2.2.1 except the imaging area was increased to 10 mm by 10mm (the ROI used for analysis remained the same).

2.2.7 Double Integrating Sphere System

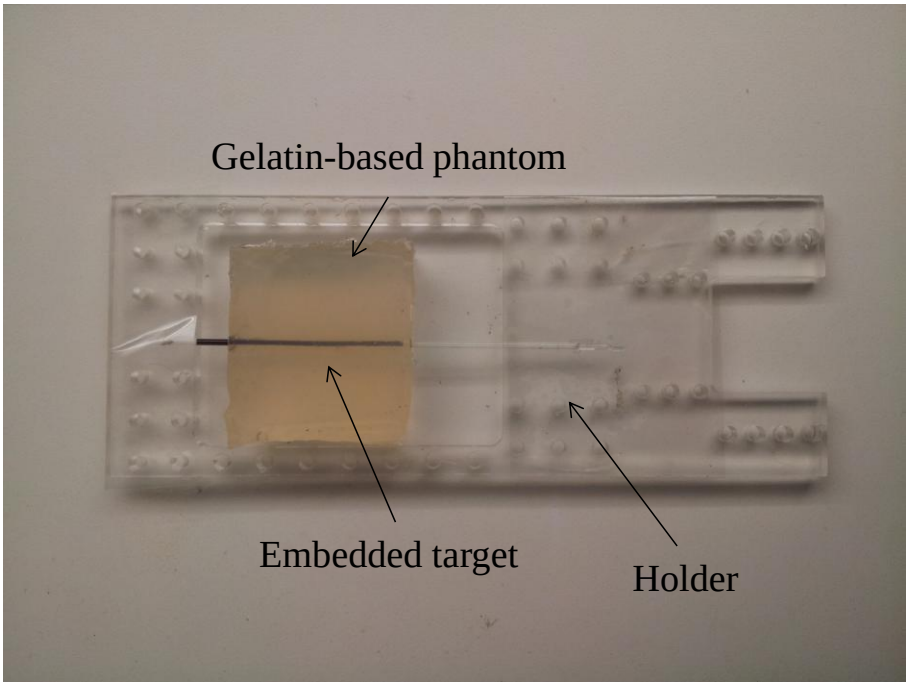

Figure 2.3: A representative tissue-mimicking phantom secured to a holder placed into the OA system waterbath during image acquisition. The gelatin-based phantom was constructed to mimicking mouse muscle and skin and the embedded glass tube filled with highly absorbing solution (0.8 cm^{-1}) mimics a highly vascularized tumour.

The goal was to construct a phantom with μ_a = 0.2 cm^{-1} and μ_s=10 cm^{-1} at 775 nm, and μ_a = 0.2 cm^{-1} and μ_s= 20 cm^{-1} at 1064 nm to simulate generic murine overlaying tissues [8]. Samples of each batch of gelatin solution used in the phantom development were sent to Ryerson University, Toronto ON where the optical properties were measured using the double integrated sphere (DIS) approach [33].

Accurate determination of the optical properties was needed to understand and predict light propagation and distribution within the gelatin material. The diffuse reflectance (*Rd),* diffuse transmittance (*Td),* and the collimated transmittance (*Tc),* were measured for each gelatin sample. To measure the optical properties, a sample is placed between two identical integrating spheres of 30.5 cm (12 in.) diameter with a circular sample window of 25 mm diameter and illuminated with a white light operating at 7 W (Ocean Optics, Dunedin, FL, USA). Light was focused onto the sample using a set of optics that collimate and produce a 5 mm beam diameter. *Rd* and *Td* were collected in the first and second sphere respectively and *Tc* was collected by capturing the collimated transmittance at a distance of 100 mm beyond the second sphere, as shown in Figure 2.4. Measurements were collected using an optical spectrometer. *Rd* and *Td* were measured relative to a baseline signal using a 99% reflecting plate (Sphere 30 Optics, SG2052, Concord, NH, USA) that was placed at the sample aperture while *Tc* was determined relative to 100% transmission (i.e. with no sample).

From these three measured parameters a unique relationship exists from which the absorption coefficient and scattering coefficient can be derived [34]. Different methods are available to compute the optical properties on measured values, such as the inverse adding doubling algorithm (IAD) which was used in this study [35], and the more

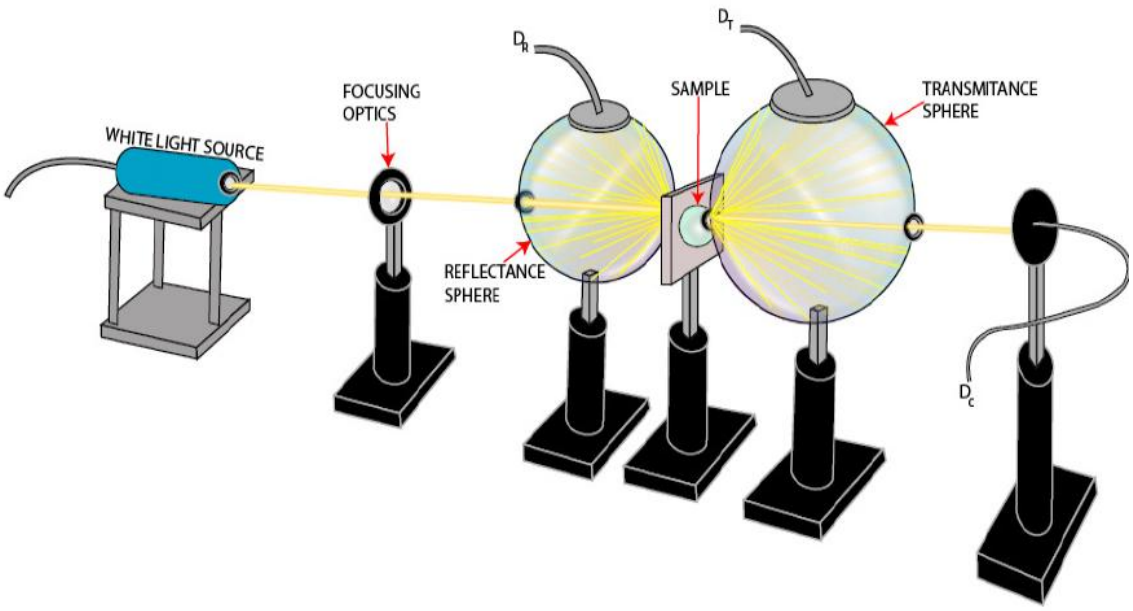

Figure 2.4: Experimental setup of DIS using a white light source. DR, DT, DC are the locations where *Rd*, *Td*, and *Tc* are measured from respectively. Adapted from Castelino 2008 [34].

sophisticated but highly computationally intensive method using Monte Carlo (MC) simulations where the measured values are correlated using an inverse MC [36,37].

2.2.8 Data Analysis

A Matlab®-based script was developed to analyze the OA signal. The Hilbert transform was applied to all signals. The maximum of the Hilbert transform along each signal was defined as the front surface of the tube. The area under each signal curve was integrated and this was defined as the integrated area under the curve. The average, baseline corrected, amplitude within a 1.5 mm by 1.5 mm region of interest (ROI) centered along the front surface of the tube was defined as OA signal amplitude.

The width of the tube in the axial direction (axis of the transducer) was measured as the distance between the two 'peaks' in the signal (peak to peak distance). The width in the lateral direction (perpendicular axis to the transducer) was determined by applying the Full Width Half Max (FWHM) approach to the acquired OA signals [38].

Standard student t-tests were employed to test for significant differences between the generated data in this chapter. Repeated trials were accounted for by an ANOVA with repeated measures when necessary.

2.2.9 Image Formation Methods

The axial data were compressed to, or presented as two dimensions to give the optimal lateral size predictions. For the compression techniques, only data from a time window corresponding to a 0.5 cm depth (centered on the tube) was used for analysis. Three techniques were analyzed.

1. Integrated amplitude projection (IAP)

The signal values were integrated within each time window, at each signal acquisition position, and projected onto a 2D plane as the corresponding pixel value in the final two-dimensional image.

2. Maximum intensity projection (MIP)

   The maximum signal value within each time window at each position was identified. This value was projected onto a 2D plane as the corresponding pixel value in the final two-dimensional image.

3. Two-dimensional slices

   Several single 2D slices (at the front surface, center and back of the tube) were analyzed. There may be some important volumetric information in this data which may be lost during image compression.

Two-dimensional images were constructed using the above three different techniques and the image contrast and accuracy were measured and compared to determine the optimal technique.

2.3 Results

2.3.1 Image formation techniques and associated contrast and accuracy

The three optoacoustic image formation techniques described in the Materials and Methods section (2.2.9) are represented in Figure 2.5. Representative two-dimension OA images of 3 mm glass tubes filled with a solution of 0.8 cm^{-1}, acquired with 775 nm illumination, are shown. Images of the tube at 0 mm (on the surface of the tissue-mimicking phantom) and embedded at a depth of 3 mm in a tissue-mimicking phantom described previously are shown.

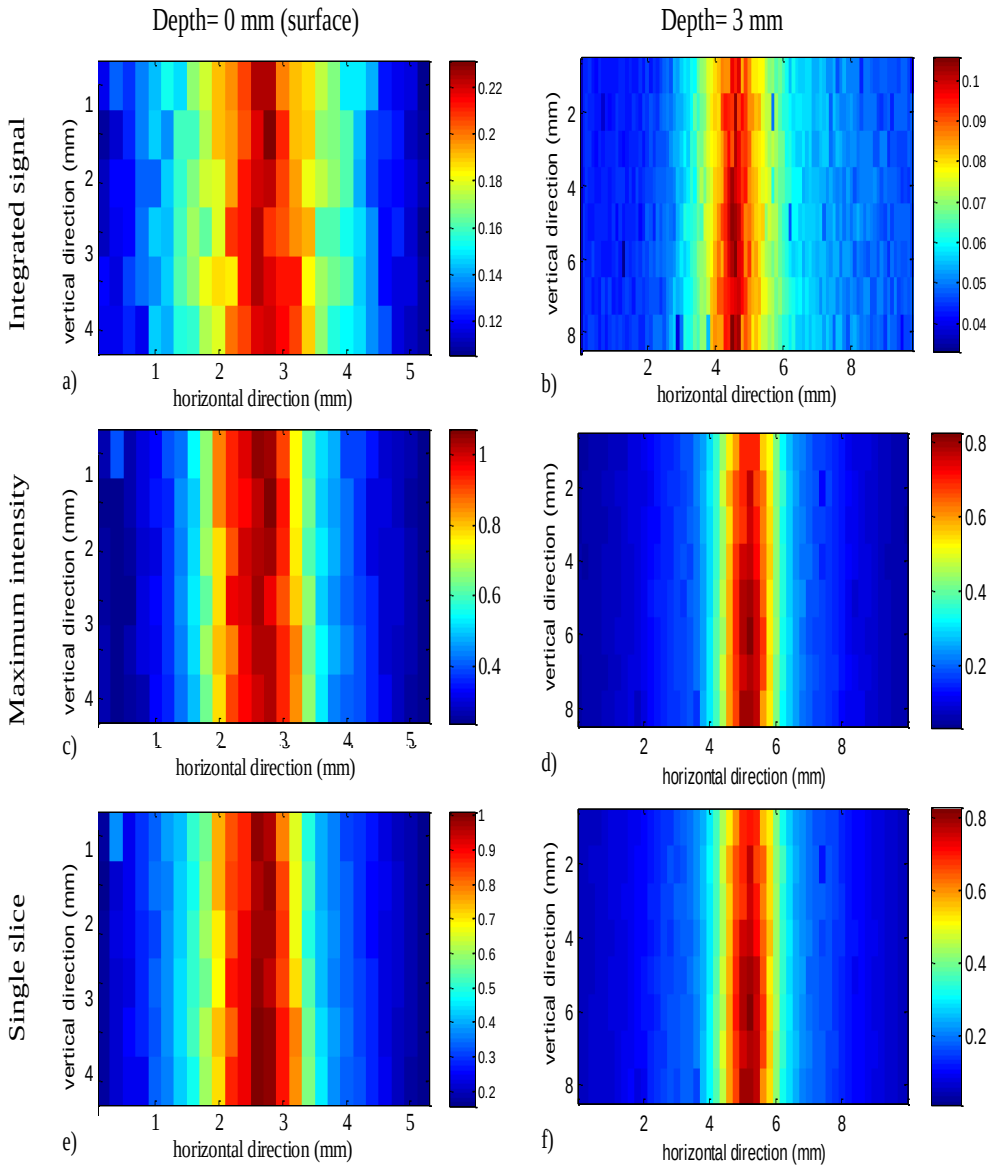

Figure2.5: Representative optoacoustic images of integrated and maximum signal amplitude projections and single slices in the lateral direction of a 3 mm glass tube filled with a solution of absorption coefficient of 0.80 ± 0.01 cm^{-1}. Front surface of the targets were placed at 25 mm from the transducer. Images are shown of the tube at depths of 0 mm (on surface of phantom) and at 3 mm in phantom. Amplitude scales of each image are set to the maximum and minimum amplitude value and vary from maximum of 0.1 (b) to >1 (c, e). Images at 0mm are 5 mm by 5 mm, images at 3 mm are 8 mm by 8 mm Images acquired with 775 nm illumination.

A representative OA signal (Hilbert transformed) and a one-dimensional IAP of a 3 mm tube filled with a 0.6 cm^{-1} solution onto a lateral plane are shown below (Figure 2.6). Width predictions were calculated along both the axial direction (peak to peak) and lateral direction (full width half max). The prediction results are shown in Figure 2.7. Target width predictions in the axial direction (along the axis of the transducer) had a mean of 1.8 mm and a standard deviation of 0.8 mm and, thus, underestimated with the true width by approximately 30%. The width predictions in the lateral direction (axis perpendicular to the transducer), using FWHM, had a mean of 3.0 mm and a standard deviation of 0.5 mm.

Contrast measurements and width predictions associated with the three compression techniques (see Section 2.2.8) are described in Table 2.3. Results are from signals acquired with 775 nm illumination.

Contrast values were greater on the maximum intensity projection images and the single slice images, averaging 3.9 ± 0.8 and 3.8 ± 0.9 respectively, compared to the IAP images whose contrast values averaged 2.0 ± 0.5. Target width predictions from the IAP images agreed with the true tube dimensions with standard deviations of approximately 3%. Maximum signal projection and slices had associated standard deviations of approximately 15% . Although contrast is lower on the IAP (yet still high compared with ultrasound contrast which is often less than 1 [39]), the accuracy of the width predictions (with overlaying scattering medium) was deemed crucial for future experiments. Therefore, based on these results all further compressions were accomplished using the IAP technique.

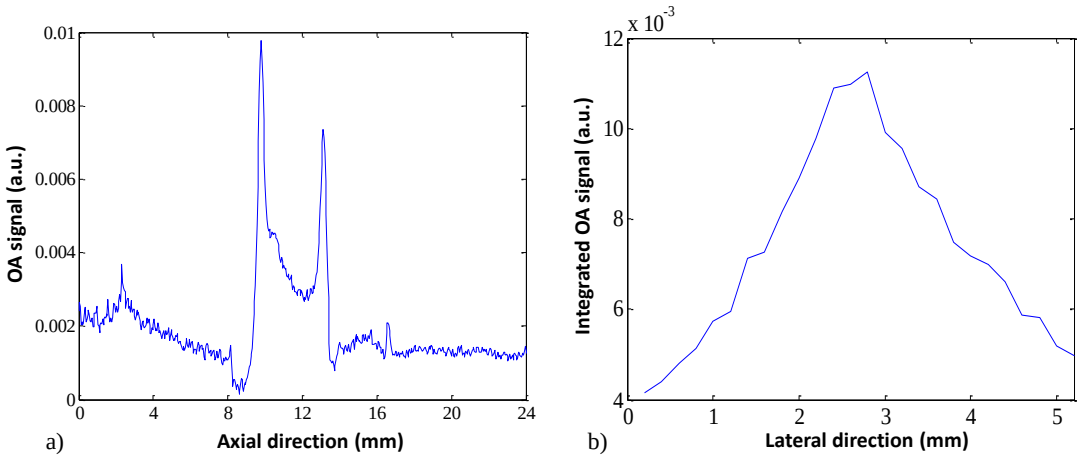

Figure 2.6: Representative a) optoacoustic signal, acquired with 775 nm illumination, generated by a thin-walled glass tube filled with a solution with an absorption coefficient of 0.6 cm^{-1} and b) OA integrated amplitude, projected onto the lateral plane (direction perpendicular to the transducer), generated by the same 3 mm tube.

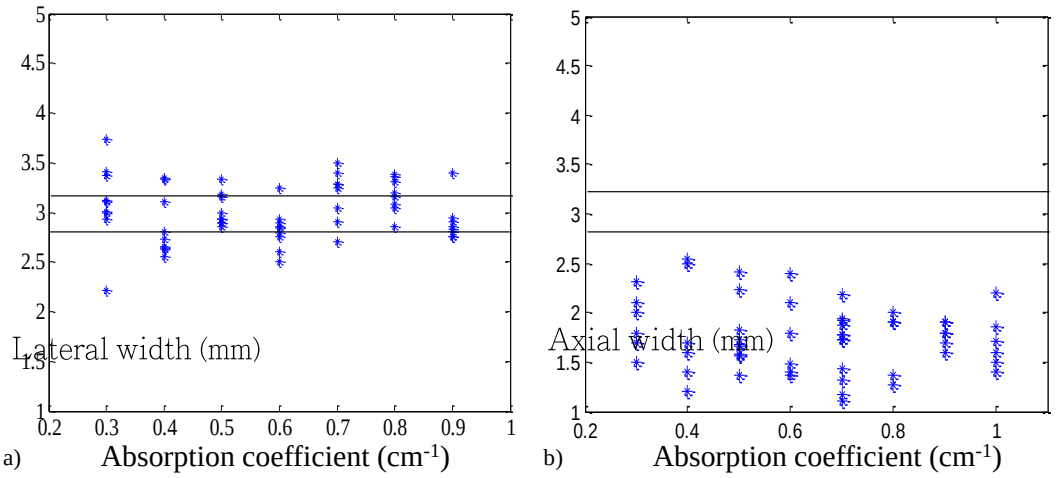

Figure 2.7: OA predicted target widths acquired with 775 nm illumination, a) in the lateral direction (perpendicular to the transducer axis) measured using full width half max of the integrated amplitude projection, b) in the axial direction (parallel to the transducer axis) measured as the distance between the front and back peaks in the OA signal (peak to peak). Horizontal lines indicated ± 10%.

Table 2.3: Contrast and width predictions of an absorbing target embedded at three depths in a gelatin phantom. Three image compression approaches were investigated for each optoacoustic image (integrated signal, maximum signal and slice). Uncertainties are presented as one standard deviation (N=9). Images acquired with 775 nm illumination.

Depth of target (mm)	**Contrast (integrated signal)**	**Contrast (maximum signal)**	**Contrast (single slice)**	**Width (integrated signal, mm)**	**Width (maximum signal, mm)**	**Width (single slice, mm)**
0	1.8±0.4	4.7±0.2	3.3±0.3	3.3±0.1	3.1±0.4	3.2±0.4
3	2.7±0.3	4.0±0.1	5.5±0.8	3.3±0.1	3.0±0.4	3.0±0.4
5	1.5±0.2	2.9±0.3	2.6±0.6	3.1±0.2	3.0±0.4	3.2±0.5

Optoacoustic signal amplitudes and axial widths of the thin-walled glass tubes with 3 mm diameters filled with absorbing solution (with an absorption coefficient of 0.8 cm^{-1}) and embedded at depths of 0 mm (surface), 3 mm and 5 mm in gelatin, acquired with 775 nm illumination, are summarized in Table 2.4.

2.3.2 Optoacoustic transducers' focus

The focal point of the OA system's transducer is located at 25 mm from its front surface (Figure 2.8a). The transducer has a focal width of 0.5 mm and focal length of 10 mm. Figure 2.8b shows the integrated OA signal amplitude from a tube (filled with a solution which an absorption coefficient of 0.6 cm^{-1}) as a function of distance from the tube's front surface to the transducer. For both 775 nm and 1064 nm illuminations, the amplitude of the signals decreased by approximately 50 % at 20 mm and 30 % at 30 mm compared with the signal at 25 mm (transducer focal point).

These results demonstrated the necessity for accurate placement of targets in the OA imaging system. All further measurements were acquired with the target placed at 25mm from the transducer surface.

2.3.3 System sensitivity, repeatability and theory validation

The two graphs in Figure 2.9 show the integrated OA signal amplitude and the absorption coefficient of the solution inside the tube. All measurements were taken with the front surface of the tube placed 25 mm from the transducer.

The OA signal versus target optical absorption coefficient was fit to a line and the correlation coefficients of 0.9112 and 0.9178 at 775 nm and 1064 nm illumination indicate a strong linear correlation. The two illuminations have the same relative slope

Table 2.4: Optoacoustic integrated signal amplitude generated by 3 mm tubes filled with absorbing solution at three depths in gelatin phantoms and associated axial width predictions. Average values ± standard deviations are presented (N=9). Images acquired with 775 nm illumination.

Depth of tube (mm)	OA signal amplitude (a.u.)	Axial width (mm)
0	0.0098 ± 0.0002	1.8±0.3
3	0.0077 ± 0.0005	3.1±0.1
5	0.0090 ± 0.0005	3.3±0.1

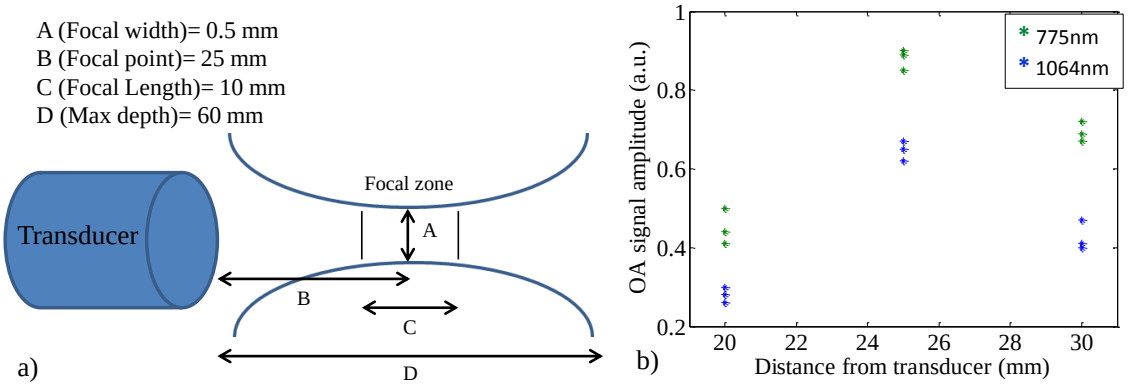

Figure 2.8: a) Schematic of the focal properties of the transducer in the SENO optoacoustic imaging system, and b) Integrated optoacoustic signal amplitudes generated by a 3 mm tube filled with a solution of 0.6 cm^{-1} absorption at three distances from the transducers' surface (N=3).

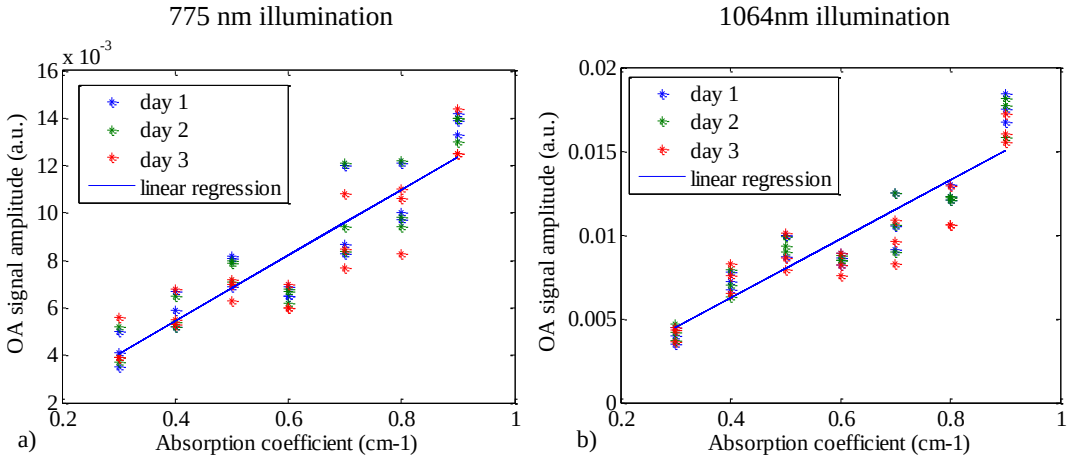

Figure 2.9: The integrated optoacoustic signal amplitude as a function of absorption coefficient showing a linear relationship with an R^2 value of 0.9112 and 0.9178 for 775nm and 1064nm illumination respectively.

as well. Theoretically, the OA signal values would fall on a linear line. A standard student t-test found significant differences between targets with absorption coefficients differing by greater than 0.2 cm^{-1} for both illuminations. A two-way ANOVA was also used to determine that there were no significant differences between the repeated data generated on the same day and on consecutive days (Figure 2.10). Thus, the system also has good repeatability within and between days. This also demonstrates that the system can detect targets with absorption coefficients down to 0.3 cm^{-1}.

2.3.4 Target size considerations

A subset of OA images were acquired of 5 mm thin glass tubes filled with solutions of different absorption coefficients. The data analysis performed was identical to that used for the 3 mm glass tube study. Table 2.5 presents the integrated OA signal amplitude and width predictions of the 5 mm tubes.

There were no significant differences between the amplitude of the generated OA signal of a 3 mm and 5 mm glass tube containing liquid with the same absorption coefficient. Width predictions in the axial direction underestimated with the true width by approximately 25% with an average predicted width of 3.7 mm and a standard deviation of 0.2 mm. The width predictions in the lateral direction using FWHM, were on average 5.5 mm and a standard deviation of 0.5 mm.

2.4 Discussion and Conclusions

This study aims to characterize the SENO OA imaging system by defining the following characteristics: system sensitivity and repeatability, and image contrast and accuracy (in this study, defined as the accuracy of the images to predict the true target width). The results demonstrate the necessity for proper image compression methods to

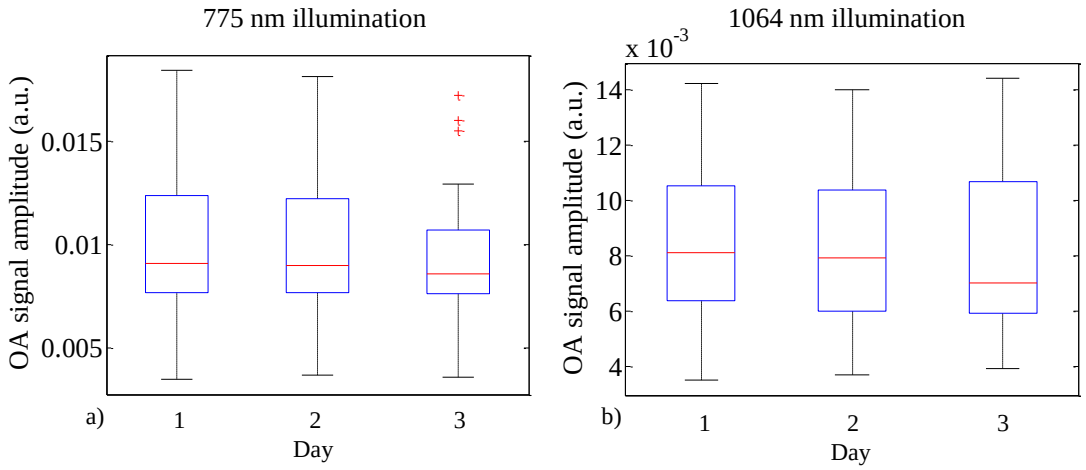

Figure 2.10: Boxplots represent the integrated optoacoustic signal amplitudes generated by solutions with absorption coefficients ranging from 0.3 to 0.9 cm^{-1} on 3 consecutive days for both 775 nm and 1064 nm illumination (N=9). A two-way ANOVA demonstrated that there were no significant differences between days ($p<0.05$). The red center line represents the mean value, the blue box represents one standard deviation and the black bars represent the spread of the data. Red crosses represent outliers in the data.

Table 2.5: Integrated optoacoustic signal amplitudes and predicted widths (axial and lateral) generated by 5 mm thin-walled glass tubes filled with solutions of varying absorption coefficients. Average values ± standard deviations are presented (N=9).

Absorption coefficient (cm-1) ±10%	**Illumination wavelength (nm)**	**OA signal amplitude**	**Axial width (peak to peak)**	**Lateral width (FWHM)**
0.3	775	0.005±0.005	3.88±0.01	5.4±0.2
0.3	1064	0.005±0.001	3.92±0.01	5.5±0.2
0.6	775	0.008±0.004	3.4±0.02	5.6±0.1
0.6	1064	0.009±0.001	3.50±0.05	5.6±0.2
0.9	775	0.015±0.001	3.85±0.07	5.4±0.1
0.9	1064	0.016±0.001	3.85±0.08	5.4±0.1
Average			3.7±0.2	5.5±0.5

be used, as well as the importance of overlaying scattering material for accurate width predictions. Three different compression methods were compared which compressed three-dimensional data to two-dimensions images. Furthermore, this study demonstrated the relatively large effect that the target positioning with respect to the transducer has on the detected signal strength.

Three different compression techniques were investigated in this study. Predicted tube widths measured in the axial direction (along the axis of the transducer) were underestimated by more than 1 mm (40%) with a standard deviation of 0.3 mm when there was no overlaying scattering medium (i.e. the tube was not embedded in a phantom). Width measurements in the lateral direction (along the axis perpendicular to the transducer) agreed with the true width with standard deviation of 3% for IAP images and up to 15% for slices and MIP images. Contrast was reduced in the IAP compared to the MIP and single slices, however, the IAP approach was chosen based on its more accurate size predictions which were deemed crucial for future experiments. Similar results were found when imaging 5 mm glass tubes. When overlaying scattering medium is introduced the axial width measurements agreed with the true width within 0.3 mm (10%). Future *in vivo* and *ex vivo* targets will always have overlaying scatters. Other, similar systems presented in literature achieve accuracies of approximately 0.1 to 1 mm [38,40,41]. Based on these results, we conclude that the OA system can accurately predict target size within 10%, when there is overlaying scattering medium, using peak to peak and FWHM analysis of IAP images.

The transducer's focus had a large impact on the detected OA signal strength. Signal strength decreased by almost 50% and 30% with the target placed at -5 mm and

+5 mm, respectively from the transducer's focus. The transducers focus is where we would expect the highest signal to be obtained from any given target. The OA laser is delivered by two bifurcated fibers which are positioned so that the beams intersect at approximately 25 mm (the transducers' focus). The combination of these two system characteristics causes the quick drop off in signal outside the focal point of the transducer.

The OA signal amplitude increased linearly, on a one to one basis with the absorption coefficient as expected give the OA pressure equation. The linear fit of the data has a high R^2 value validating the associated theoretical relationship [42]. The slope of the fit is approximately 1 at both 775 nm and 1064 nm illumination. Targets with absorption coefficients of as low as 0.3 cm^{-1} were detected indicating that the system has sensitivity adequate for detecting highly vascularized tissues (often with absorption coefficients greater than 0.3 cm^{-1} in the near infrared range [7]). Targets with absorption coefficients which differ by greater than 0.2 cm^{-1} could be differentiated based on statistical tests performed on data from Figure 2.9. The absorption coefficient of normal human prostate tissue (the absorption of mouse prostate as these wavelengths is not well-known) at 786 nm is approximately 0.3 cm^{-1} [9], while highly vascularized tumours often have very high absorption coefficients, in the near infrared range, greater than 1.0 cm^{-1} [38]. Thus, OA imaging should be able to detect a tumour from background prostate tissue based on their respective absorptions. Therefore, based upon the results of this study we conclude that the OA imaging system used herein will be capable of differentiating normal tissue from highly vascularized tissue. Images that were acquired of identical targets at different times (within and between 3 days) showed no significant

differences between the generated signal contrasts. This demonstrates that the system has good repeatability up to three days. However, the variation among the signals produced by targets with the same absorption coefficient (Figure 2.9), as well as the variation among the predicted axial and lateral widths (Figure 2.7) was relatively high. Variations up to 25% between signals generated by tubes with the same absorption coefficient were observed (Figure 2.9). Variations up to 30% in the width predictions were also observed (Figure 2.7) This is very important as future studies will involve imaging targets several days apart. Although the system variation between days may not affect the generated signals, the variation among the images may be high. This may necessitate larger sample sizes and larger signal averaging to be performed to ensure our results are valid.

There was no significant difference between the integrated OA signal amplitudes generated by the 3 mm and 5 mm glass tubes (containing solutions with the same absorption coefficients) or the differences are beyond the sensitivity of the system. As a result, only a subset of absorption coefficients (3 rather than 8) were investigated using 5 mm diameter tubes. Thus, small changes in the target size do not affect the OA signal significantly compared with changes in its absorption coefficient. Although the amplitude of the OA would theoretically increase with target diameter [42], the sensitivity of this system was not capable of distinguishing the two sizes based on amplitude.

The results of this study partially characterized the SENO OA system, and highlight some of the OA system-dependent features. The sensitivity and repeatability of the system will aid to set up future experiments by; describing the systems capabilities to detect and differentiate targets based on their absorption coefficients,

allow sample size calculations to be performed, etc. Image contrast and accuracy were determined for three image compression techniques. The preferred image compression technique was chosen based on these parameters. The information acquired may be used to aid in developing more sophisticated imaging protocols for future studies using this specific OA system, and serves as a reference point when analyzing more complex tissue data.

References

1. Xu, X.-H. & Li, H. Photoacoustic imaging in biomedicine. *Physics - Beijing* **37**, 111–119 (2008).

2. Folkman, J. & Kalluri, R. Cancer without disease. *Nature* **427**, 787 (2004).

3. Larin, K. V, Larina, I. V & Esenaliev, R. O. Monitoring of tissue coagulation during thermotherapy using optoacoustic technique. *Journal of Physics- London* **38**, 2645–2653 (2005).

4. Wang, L. V Ultrasound-mediated biophotonic imaging: A review of acousto-optical tomography and photo-acoustic tomography. *Disease markers* **19**, 123–138 (2003).

5. Wang, L. V & Hu, S. Photoacoustic tomography: in vivo imaging from organelles to organs. *Science* **335**, 1458–62 (2012).

6. *Progress in quantitative coronary arteriography*. **155**, (Springer Netherlands: Dordrecht, 1994).

7. Wang, G. *et al.* In vivo mouse studies with bioluminescence tomography. *Optics Express* **14**, 7801 (2006).

8. Cheong, W.-F., Prahl, S. A. & Welch, A. J. A review of the optical properties of biological tissues. *SPIE Milestone series* **102**, 129 (1995).

9. Laidevant, A. *et al.* Fluorescence time-resolved imaging system embedded in an ultrasound prostate probe. *Biomedical optics express* **2**, 194–206 (2010).

10. Passler, K., Nuster, R., Gratt, S., Burgholzer, P. & Paltauf, G. Piezoelectric annular array for large depth of field photoacoustic imaging. *European Conferences on Biomedical Optics* **2**, 809012–809012–7 (2011).

11. Petrovic, A. M., Siebert, J. E. & Rieke, P. E. Soil Bulk Density Analysis in Three Dimensions by Computed Tomographic Scanning1. *Soil Science Society of America Journal* **46**, 445 (1982).

12. Agarwal, A. *et al.* Targeted gold nanorod contrast agent for prostate cancer detection by photoacoustic imaging. *Journal of Applied Physics* **102**, 064701 (2007).

13. Ku, G. & Wang, L. V. Deeply penetrating photoacoustic tomography in biological tissues enhanced with an optical contrast agent. *Optics Letters* **30**, 507 (2005).

14. Andreev, V. G., Karabutov, A. A. & Oraevsky, A. A. Detection of ultrawide-band ultrasound pulses in optoacoustic tomography. *IEEE Transactions on Ultrasonics, Ferroelectrics and Frequency Control* **50**, 1383–1390 (2003).

15. Nicholson, R. & Crofton, M. Training phantom for ultrasound guided biopsy. *British Journal of Radiology* **70**, 192–194 (1997).

16. Kato, H. An agar phantom for hyperthermia. *Medical Physics* **13**, 396 (1986).

17. Hebden, J. C., Price, B. D., Gibson, A. P. & Royle, G. A soft deformable tissue-equivalent phantom for diffuse optical tomography. *Physics in medicine and biology* **51**, 5581–90 (2006).

18. Hebden, J. C., Hall, D. J., Firbank, M. & Delpy, D. T. Time-resolved optical imaging of a solid tissue-equivalent phantom. *Applied optics* **34**, 8038–47 (1995).

19. Pogue, B. & Patterson, M. Review of tissue simulating phantoms for optical spectroscopy, imaging and dosimetry. *Journal of Biomedical Optics* **11**, (2006).

20. Chen, E. J., Novakofski, J., Jenkins, W. K. & O'Brien, W. D. Young's modulus measurements of soft tissues with application to elasticity imaging. *IEEE Transactions on Ultrasonics, Ferroelectrics and Frequency Control* **43**, 191–194 (1996).

21. Foschum, F. & Kienle, A. Broadband absorption spectroscopy of turbid media by using a dual step steady-state method. *Journal of biomedical optics* **17**, 037009 (2012).

22. Beard, P. C. Photoacoustic imaging of blood vessel equivalent phantoms. *International Symposium on Biomedical Optics* 54–62 (2002).doi:10.1117/12.469848

23. Cook, J. R., Bouchard, R. R. & Emelianov, S. Y. Tissue-mimicking phantoms for photoacoustic and ultrasonic imaging. *Biomedical optics express* **2**, 3193–206 (2011).

24. Passler, K., Nuster, R., Gratt, S., Burgholzer, P. & Paltauf, G. Annular piezoelectric ring array for photoacoustic imaging. *European Conferences on Biomedical Optics* 809012–809012–7 (2011).

25. Song, K. H. & Wang, L. V Deep reflection-mode photoacoustic imaging of biological tissue. *Journal of Biomedical Optics* **12**, 60503 (2007).

26. Esenaliev, R. O., Karabutov, A. A. & Oraevsky, A. A. Sensitivity of laser opto-acoustic imaging in detection of small deeply embedded tumors. *IEEE Journal of Selected Topics in Quantum Electronics* **5**, 981 (1999).

27. *American National Standard for the safe use of lasers / secretariat, the Laser Institute of America*. (Orlando, FL : The Institute, c1993: 1993).

28. Thermo Scientific Spectronic 20+ and 20D+ Visible Spectrophotometers - Fisher Scientific. at <http://www.fishersci.com/ecomm/servlet/fsproductdetail_10652_5391897__-1_0>

29. Coefficient of Determination (R-Squared) - MATLAB & Simulink. at <http://www.mathworks.com/help/stats/coefficient-of-determination-r-squared.html>

30. Cohen, J. *Statistical Power Analysis for the Behavioral Sciences*. 567 (Psychology Press: 1988).

31. Madsen, S. J., Patterson, M. S. & Wilson, B. C. The use of India ink as an optical absorber in tissue-simulating phantoms. *Physics in Medicine and Biology* **37**, 985–993 (1992).

32. Ayache, N. Delingette, H. Golland, P. Mori, K. *Medical Image Computing and Computer-Assisted Intervention*. **1935**, (Springer Berlin Heidelberg: Berlin, Heidelberg, 2000).

33. Pickering, J. W. *et al.* Double-integrating-sphere system for measuring the optical properties of tissue. *Applied optics* **32**, 399–410 (1993).

34. Castelino, R. Biomedical applications of photoacoustics for thermal therapy . 72 (2008).

35. Prahl, S. A., van Gemert, M. J. & Welch, A. J. Determining the optical properties of turbid mediaby using the adding-doubling method. *Applied optics* **32**, 559–68 (1993).

36. Roggan, A., Albrecht, H. J., Doerschel, K., Minet, O. & Mueller, G. J. Experimental set-up and Monte-Carlo model for the determination of optical tissue properties in the wavelength range 330 to 1100 nm. *International Symposium on Biomedical Optics Europe '94* 21–36 (1995).

37. Yaroslavsky, I. V. & Tuchin, V. V. Inverse Monte Carlo method for spectrophotometric data processing. *Volga Laser Tour '93* 57–68 (1994).doi:10.1117/12.179027

38. Laufer, J. *et al.* In vivo longitudinal photoacoustic imaging of subcutaneous tumours in mice. *Proceedings of SPIE* **7899**, 789915 (2011).

39. Michailovich, O. V & Tannenbaum, A. Despeckling of medical ultrasound images. *IEEE transactions on ultrasonics, ferroelectrics, and frequency control* **53**, 64–78 (2006).

40. Laufer, J., Zhang, E., Raivich, G. & Beard, P. Three-dimensional noninvasive imaging of the vasculature in the mouse brain using a high resolution photoacoustic scanner. *Applied Optics* **48**, D299–D306 (2009).

41. Montilla, L. G., Olafsson, R., Bauer, D. R. & Witte, R. S. Real-time photoacoustic and ultrasound imaging: a simple solution for clinical ultrasound systems with linear arrays. *Physics in medicine and biology* **58**, N1–12 (2013).

42. Beard, P. Biomedical photoacoustic imaging. *Interface focus* **1**, 602–31 (2011).

CHAPTER 3

OPTOACOUSTIC CHARACTERIZATION OF PROSTATE CANCER IN AN *IN VIVO* TRANSGENIC MURINE MODEL

"Give me a place to stand, a lever long enough and a fulcrum and I can move the Earth"

-Archimedes (287-212 BC.)

picture from http://www.goodreads.com/author/show/661188.Archimedes

The data presented in this chapter has been accepted for publication to Journal of Biomedical Optics (April 13 2014, manuscript #130660R).

Summary

Optoacoustic imaging was employed to distinguish normal from neoplastic tissues in a transgenic murine model of prostate cancer. Optoacoustic images of five tumour bearing mice and five age-matched controls across a 14 mm by 14 mm region of interest (ROI) on the lower abdomen were acquired using a reverse-mode optoacoustic imaging system (Seno Medical Instruments Inc., San Antonio, TX).

Neoplastic prostate tissue was identified based on the optoacoustic signal amplitude in combination with spectral analysis of the optoacoustic radio frequency (RF) data. Integration of the signal amplitude images was performed to construct two-dimensional images of the region of interest (ROI). The prostate tumours generated higher amplitude signals than those of the surrounding tissues, with contrast ratios ranging from 31 dB to 36 dB. The RF spectrum analysis showed significant differences between the tumour and control mice. The midband fit was higher by 5 dB (62%), the intercept higher by 4 dB (57%) and the spectral slope higher by 0.4 dB/MHz (50%) for neoplastic prostate tissue compared to normal tissues in the control mice. The results demonstrate that optoacoustics offers high contrast imaging of prostate cancer in vivo.

3.1 Introduction

Conventional imaging techniques for prostate cancer such as ultrasound, computed tomography, and magnetic resonance imaging are used to identify abnormal areas in the prostate which may then be biopsied for a definitive diagnosis. These imaging techniques do not reliably distinguish neoplastic from healthy prostate tissue [1], leading to the large sampling error associated with biopsies. A sensitivity of only 50% is estimated for these techniques [2]. The ability to accurately visualize neoplastic regions in the prostate may improve biopsy targeting and reduce sampling error.

One of the most common techniques used for local evaluation of the prostate is transrectal ultrasound (TRUS) because it can be performed in real-time and has relatively good resolution [3]. TRUS often uses 5-7 MHz transducers, which provide resolutions of 0.3-0.5 mm at best [3,4]. However, the accuracy of this technique is reported to be less than 50-60% with respect to detection of prostate cancer, due largely to the weak contrast at depth in soft tissues [5–7]. Conventional diagnosis is currently based solely on the detection of gross anatomic properties of tissues [6]. Recent techniques have been developed that probe tissue microstructure based on the spectral analysis of radiofrequency (RF) data [8,9], however, these ultrasonic techniques do not provide any information on the oxygen saturation or hemoglobin concentration of the tissue, both of which are often altered with neoplasia [10,11]. Pure optical imaging techniques, such as diffuse optical tomography (DOT), are being investigated as possible targeting technologies for prostate cancer evaluation because of their ability to achieve adequate contrast in soft tissues, and their ability to measure the oxygen saturation and hemoglobin concentrations of the tissues [12,13]. These techniques suffer

from strong light scattering in biological tissues [12], resulting in either very limited imaging depth (<1 mm) as in optical coherence tomography (OCT), or limited resolution, as in DOT [10].

This emerging technique of optoacoustic (OA) imaging overcomes the limitations described by merging the contrast capability of optical imaging with the resolution of ultrasound imaging [13]. The quality of contrast in OA imaging is related to the optical properties, as in pure optical imaging and the thermomechanical properties of the target while the resolution and the maximum imaging depth are scalable with the ultrasonic frequency as in ultrasound imaging [10]. Consequently, OA imaging can provide high contrast images with good resolution and penetration depth in soft tissue [14,15].

The OA technique exposes tissues to nanosecond pulsed laser light, which induces tissue-generated acoustic waves which are detected using wide band transducers [14,15]. The amplitude of an OA signal is largely dependent upon the optical absorption properties of the target tissues. Solid tumours for example, often have an increased blood flow, and therefore hemoglobin concentration, compared to healthy tissue [16,17]. The OA approach takes advantage of the high optical absorption of hemoglobin (oxy- and deoxy-) compared with other tissue parameters, at wavelengths in the visible and near infrared (NIR) range, to generate higher amplitude signals in regions with higher hemoglobin concentrations [14,15.] High resolution OA images of the mouse vasculature have been published by a number of groups [18–22]. The frequency content of the generated OA sound waves is broadband and the detected signals are limited by the finite bandwidth of the ultrasound imaging transducers and the frequency dependent

attenuation of ultrasound in tissues [23]. The frequency content of the OA RF signals may reflect the anatomical properties of the absorbing structures in a manner similar to the established techniques involving spectral analysis of ultrasound RF data [9,24,25]. Theoretical work has shown that frequency characteristics of OA signals can differentiate between normal and neoplastic tissues even when it is not possible to resolve individual blood vessels [25]; an important consideration since many OA imaging systems cannot resolve individual blood vessels at the depth of the prostate in humans (approximately 10 cm [26]) [27,28].

Spectrum analysis of ultrasound RF data and its relation to tissue microstructure has been well described [29]. The size of the scattering structures compared to the wavelength of the incident ultrasound modifies the frequency content of the backscattered signal [30]. Therefore, the frequency analysis of the ultrasound backscatter RF signals holds useful information about the medium sub-resolution structures. Large databases have been developed, which are used with statistical classifiers to identify specific tissue types from spectral image data [8]. Analysis of the frequency parameters of the RF signals improves the diagnostic capabilities of conventional ultrasound imaging [8,29,31].

Radio frequency data are collected in OA imaging wherein the size of the absorbing structure contributes to the frequency content of the OA signal [32]. Spectrum analysis of RF OA signals generated by blood vessel phantoms (cylindrical tubes filled with ink and embedded into gelatin) show a relationship between the spectral parameters and the diameter of the cylinders [33]. Spectrum analysis of high-frequency OA signals from *ex vivo* ocular tissue has also shown changes in the midband fit and

slope around the pigmented iris [34]. Thus, the relationship between the spectral parameters of OA data is likely linked to the physical properties of the target and more specifically the spatial distribution of the hemoglobin concentration within the tissues [34]. Hence, quantitative measurements may allow for databases to be established for optoacoustics which, along with statistical classifiers, may be used to identify tissue types from amplitude images and RF analysis [25]. It may also offer additional information on the target physiology and vascular morphology.

In this work, we utilized a low resolution, high contrast reverse-mode optoacoustic imaging system. Optoacoustic amplitude and frequency data were obtained from transgenic mice that develop prostate adenocarcinoma and age-matched controls. We posit that the analysis of the optoacoustic frequency parameters arising from non-resolvable tissue structures can be used to distinguish normal from neoplastic tissues.

3.2 Materials and Methods

3.2.1 Animal model

The transgenic adenocarcinoma of mouse prostate (TRAMP) model develops tumours similar to those reported in the human clinical prostate disease [35,36]. TRAMP mice develop spontaneous autochthonous prostate cancer with distant site metastasis [36]. The tumour development begins as androgen-dependent growth and then progresses to androgen-independent, a progression similar to that of the human disease [37]. The tumours originate and develop within the prostate gland which means that unlike many other implanted tumour models, they cannot be palpated or visualized in the animal prior to imaging (unless evaluated in their late stages). At the tissue level, the TRAMP

model also displays prostatic intraepithelial neoplasia (PIN) prior to adenocarcinoma formation [35]. TRAMP mice form prostate tumours as early as 12 weeks of age, with metastasis occurring as early as 24 weeks of age [38]. In the present study, we used five TRAMP mice and five age matched controls (C57BL/6J (wild type)) (Jackson Laboratories Inc, Maine, USA).

3.2.2 Optoacoustic Image Acquisition

All procedures performed in this study were approved by the Animal Care Committee of the University of Prince Edward Island in accordance with the guidelines of the Canadian Council for Animal Care. Imaging took place between 24 and 28 weeks of age. Prior to imaging, each animal was placed in an anesthetic induction chamber and anesthetized with 2.5% isoflurane in 100% oxygen. Once anesthetized, the hair on the lower abdomen of the animal was removed using a chemical hair remover (Nair ®, Church & Dwight Corporation Inc., ON, Canada) and the area to be imaged (14 mm by 14 mm) was marked using a permanent marker. The animal was maintained under general anesthesia (2.5% isoflurane in 100% oxygen), secured to a vertical holder, and lowered up to the neck in a waterbath which contained the laser fibers and transducer. Imaging in water is required to optimize acoustic coupling.

The imaging system (Seno Medical Instruments Inc., San Antonio, TX) consists of an Nd:YAG pumped Ti:Sapphire laser operating at 775 nm and an 8 element concentric annular array piezo-electric transducer (Chapter 2; Figure 2.1). The piezo-electric detection system consisting of 8 elements offers dynamic focusing capabilities which leads to a reduction in image artifacts compared to spherical detectors, and was selected because it allows for structures lying on the axis within a wide depth range to

be localized [39,40].

The transducer has a nominal central frequency of 5 MHz, with a -6dB bandwidth of 60%, a focal point at 25 mm, a focal length of 10 mm, and a focal width of 0.5 mm. The bifurcated optical fiber bundle delivered 6 ns pulses at a 10 Hz repetition rate and 20 mJ of energy per pulse. This is below the maximum permissible exposure limit of 100 mJ/cm^2 at 775 nm as per the American National Standards Institute (ANSI) [41]. Throughout the imaging process, the mouse was held stationary as the fiber bundles and transducer array performed a raster scan across the selected area, moving in 0.2 mm steps and acquiring 4 OA signals at each position for averaging. The OA data was acquired from a 14 mm by 14 mm region of interest (ROI_scan) at the lower abdomen of the mice that included the prostate region. The ROI_scan was defined by the previously described marked outline drawn on the mouse. The total imaging time was approximately 1.4 hours. This imaging time is a result of the raster approach which, for our system, requires one second acquisition time at each step (including averaging) and there are approximately 4900 steps for each image.

Immediately following the image acquisition, each mouse was euthanized with intracardiac injection of sodium pentobarbital (65 mg/kg). Three TRAMP and age-matched control mice pairs were flash frozen in liquid nitrogen, in an upright position on the holder at all times to reduce organ migration. The lower abdomen was dissected and 100 micron lateral cryosections were acquired for gross anatomical comparison with the OA images using a cryostat. The other two TRAMP and age-matched control pairs were immediately dissected following euthanasia. The prostate, seminal vesicles and any suspected abnormal tissues were fixed in a standard biological nitrogen fixation

(BNF) solution for histological processing. The tissue was sectioned and examined for evidence of prostate adenocarcinoma. The ROI_scan that was marked using a permanent marker prior to imaging was used to align the OA images with the cryosection photographs and histological sections.

3.2.3 Signal amplitude analysis

For the signal amplitude analysis, OA data from a 3 μs time window was extracted from each RF line. This time window corresponded to a 5 mm depth, beginning 1 mm beneath the front surface of the animal (and at the same depth in the age-matched control). This removed the typically strong signals acquired from the animal skin surface and included data from tissue regions that included the prostate. The Hilbert transform was applied to all RF data [27,42]. The signal strength is presented as arbitrary units and all data were collected with the same constant gain settings.

In order to account for optical attenuation by tissues which reduces the light available at depth for OA wave generation, we have employed a depth-dependent signal correction to each A-line. This is somewhat analogous to the use of time gain controls (TGC) in ultrasound imaging to account for acoustic attenuation, However, optical attenuation is significantly greater than the acoustic attenuation below 10 MHz in tissues [27]. The large aperture fiber bundles produce uncollimated light beams incident on the tissue surface. Hence, the subsurface fluence, *I (z)*, at depth *z* is diffuse and, as such, can be described using the effective attenuation coefficient, μ_{eff} , according to Cox et al. [43],

$$I(z) = I_o e^{-\mu eff * z} \qquad [1]$$

where μ_{eff} is the effective attenuation coefficient and z is the depth. An effective optical attenuation coefficient of 3.1 cm^{-1} was used as reported for rat prostate tumours [44]. The final form of the correction factor was

$$OA_{Corr}(z) = OA_{HT}(z)e^{\mu eff * z} \quad [2]$$

A MATLAB® (The MathWorks Inc.) based script was developed and used to apply the attenuation estimate to the signals. Such a correction was considered important given the variation in tumour depths that can occur among the TRAMP mice cohort.

The signal within each 3 μs time window was integrated and projected onto a two-dimensional plane to form an image. A 2 mm by 2 mm region of interest was used for analysis (ROI_analysis). This region size was chosen so that the ROI_analysis, if placed in the center of the smallest tumour, would be on-tumour tissue despite an estimated alignment uncertainty of 2 mm between the OA images and the cryosections/histological images. The alignment uncertainty includes approximately 0.5 mm uncertainty due to measured uncertainty of the positioning camera, as well as an estimated 1.5 mm uncertainty due to potential organ migration during image acquisition and prior to freezing.

Contrast values were determined between on-tumour and adjacent (off-tumour) tissues within the OA image of the TRAMP mice, as well as between tumour and the normal prostate region of the age-matched control. Contrast was measured by subtracting the average signal value within the ROI_analysis on control tissue from the average signal value within the ROI_analysis on tumour tissue and dividing by the standard deviation [45,46].

The tumour boundary was determined using the full width half maximum (FWHM) of the signal in the two-dimensional image. Hence, regions with signals greater than half the maximum signal were defined as 'on-tumour' [22].

3.2.4 Frequency Spectrum Analysis

A spectrum analysis technique commonly performed on ultrasonic backscatter RF data was used for this analysis [29]. To obtain the sensitivity of the transducer at different frequencies**,** a calibrated power spectrum was obtained by using a 200 nm thick gold film. The film was deposited onto a thin microscope cover slide with no annealing. The gold film was used because it has a broad OA power spectrum as well as a flat response in the known bandwidth of the transducer thus providing a good measure of the transducer response [47]. OA measurements were obtained across an area of approximately 1 cm^2 at 775 nm using the same power settings as the OA measurements of the TRAMP mice. A total of 20 OA signals were recorded. This was referred to as the calibrated power spectrum.

The fast fourier transform (FFT) was applied to the tissue RF data to calculate the RF echo spectrum. The mean of the squared spectral magnitudes is the averaged power spectrum (APS). The APS was converted into the decibel (dB) scale. A calibrated power spectrum is subtracted from the converted APS to remove any system-specific artifacts caused by the transducer characteristics at the focus, and system electronics.

Values were calculated over a 5 mm depth beginning 1 mm before the front surface of the tumour. The same 4 mm by 4 mm ROI_analysis used for the contrast

measurements was used. Values were calculated at each position (i.e. every 0.2 mm) within the 4 mm by 4 mm ROI_analysis and averaged. The same acquisition plane was used on the TRAMP mice and age-matched controls.

A sliding Hamming window was employed which has been shown to significantly reduce noise in spectrum analysis of ultrasound data [29]. The Hamming window had a width of 1 mm and moved in 0.5 mm steps along the axial direction. A 1 mm window was chosen so that approximately three acoustic wavelengths (at the central frequency of the transducer) were contained within each window. The power spectrum at each location was the average of the measured spectrum in each hamming window.

A linear regression was performed on the averaged power spectrum between 1 and 6 MHz and the midband fit, slope, and intercept extracted from the fit. This region was chosen based on the approximate linearity of the dataset and the high signal to noise (SNR of 5.3 dB) within these frequencies. The statistical spread of these parameters for ultrasound RF data has been previously established by others [29].

The normality of the spectral data was confirmed using a Shapiro-Wilk test with $W>0.05$ used as the criterion for normality. The variances of the spectral parameters (on versus off tumour) were found to be equal using an *F*-test with $F<0.05$ used as the criterion for equal variance. A paired t-test was used to compare the spectral parameters between normal and neoplastic tissue. A *p*-value of 0.05 or less was used to define statistically significant differences.

3.3 Results

3.3.1 Optoacoustic Imaging

Representative TRAMP and age-matched control cryosection and integrated OA signal amplitude images are shown in Figure 3.1. Approximate areas imaged on the animals are represented by black outlines. The cryosection images of both sets of control and TRAMP mice were taken from the same depth beneath the surface of the animal, 6.0 ± 0.1 mm and 7.9 ± 0.1 mm respectively, which corresponds to the maximum coronal tumour dimension in the TRAMP mice (determined from the cryosections). Each TRAMP image was normalized to its maximum signal value, and each control image was normalized to the maximum signal value from the image of its age-matched TRAMP. The OA image of the TRAMP mouse in Figure 3.1(b) shows an increase in signal amplitude in the region of the tumour and relatively sharp decreases in signal at the border of the tumour. The signals obtained from the control mouse are typically less than 0.5 a.u. and therefore beneath our defined threshold of tumour tissue (as defined in material and methods using the FWHM, and therefore above 0.5 a.u.). The tumour of the second TRAMP mouse was less vascular compared to that of the first TRAMP mouse and has therefore been outlined in Figure 3.1(e) for easier visualization. Again the tumour is visible in the corresponding OA image, Figure 3.1(f), and the OA predicted vertical and horizontals dimensions are 7.0 ± 0.5 mm and 6.0 ± 0.5 mm which agree reasonably with actual dimensions. OA contrast for tumour compared to adjacent normal, healthy tissue ranged from 31-36 dB across the 5 TRAMP mice (Table 3.1). OA contrast for tumour compared to the region of the prostate on the age-matched control animal, also ranged from 31-36 dB. The uncertainties of the contrast values are one standard deviation of the values measured within the boundaries of the ROI_analysis in the OA image.

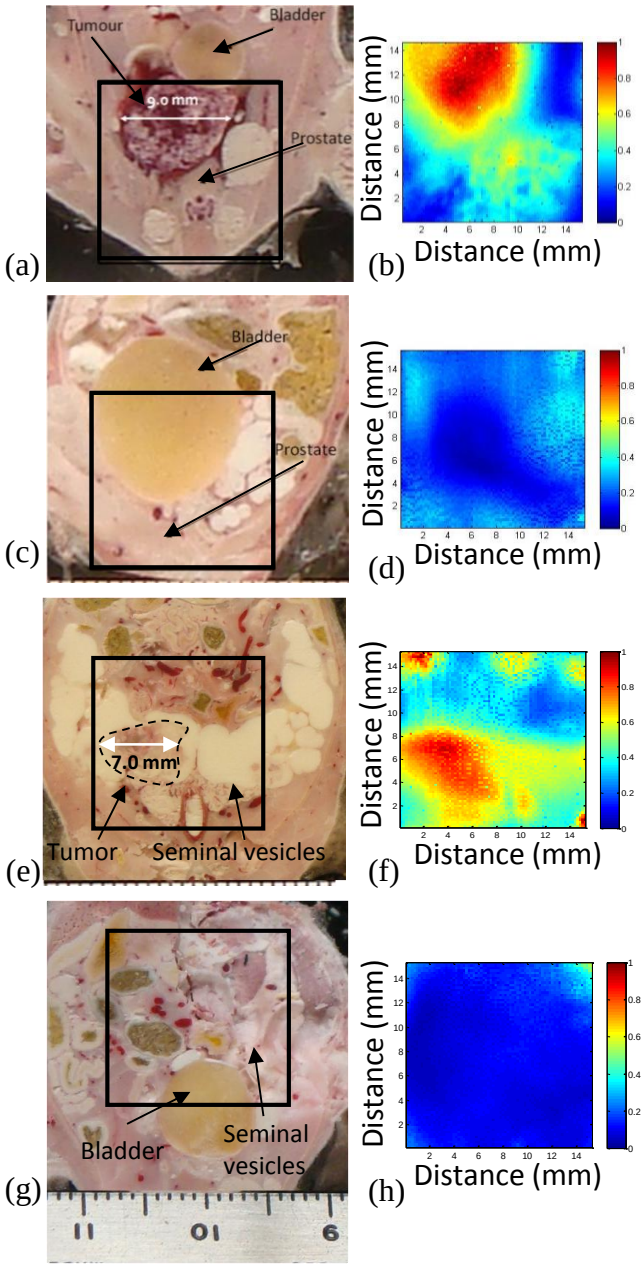

Figure 3.1: Coronal cryosection images of TRAMP tumor bearing mice (a, e), and age matched control mice (c, g). Approximate areas imaged on animals are represented by black outlines. Corresponding coronal integrated signal amplitude images of tumor bearing TRAMP mice (b and f) and age matched control mice (d and h). Both sets of optoacoustic images (TRAMP and age-matched control) were normalized to the maximum signal value of the TRAMP image

Table 3.1 Optoacoustic image contrast for 5 TRAMP mice and age-matched controls, and lateral TRAMP tumour dimensions. Values are presented as mean ± standard deviation.

Animal#	Contrast (dB)		Lateral Dimension (mm)	
	Tumour - Adjacent	Tumour - Control	From OA Image ± 0.4	From Cryosection ± 0.5
1	33 ± 2	34± 2	8.8	9.0
2	31 ± 2	35± 2	7.0	7.0
3	33 ± 2	36± 2	6.0	6.5
4	36 ± 2	34± 2	5.6	6.0
5	31 ± 2	31± 2	8.0	8.0

The OA predicted maximum lateral tumour dimension, determined using the FWHM approach, and the dimensions determined from the cryosections for the five TRAMP mice are summarized in Table 3.1. The mean tumour dimensions and measurement error (measured on cryosections) ranged from 6.0 ± 0.5 mm to 9.0 ± 0.5 mm. The results show that the OA predicted tumour dimensions agreed with the cryosection tumour dimensions to within 0.5 mm in all 5 TRAMP mice.

3.3.2 Frequency Spectrum Analysis

Representative calibrated and non-calibrated power spectra for one OA data set are shown in Figure 3.2. A linear fit was applied to the normalized spectrum between 1 and 6 MHz.

Midband fit, intercept and slope values for the 5 TRAMP mice and age-matched controls are presented in Figure 3.3 and Table 3.2. Each value represents an average of 100 spectral parameters acquired within a 2 mm by 2 mm square region of interest. Error bars represent one standard deviation. Tumour tissues generated higher values of all three parameters compared with normal tissues (adjacent and control).

Mean and standard deviation values from all TRAMP mice on tumour and on adjacent tissue, and from all control mice are presented in Table 3.2. There was a six fold increase in midband fit and a two fold increase in slope values on tumour compared with control. Significant differences ($p<0.05$) were found between all spectral parameters. No significant difference was found between the control and adjacent spectral parameter values.

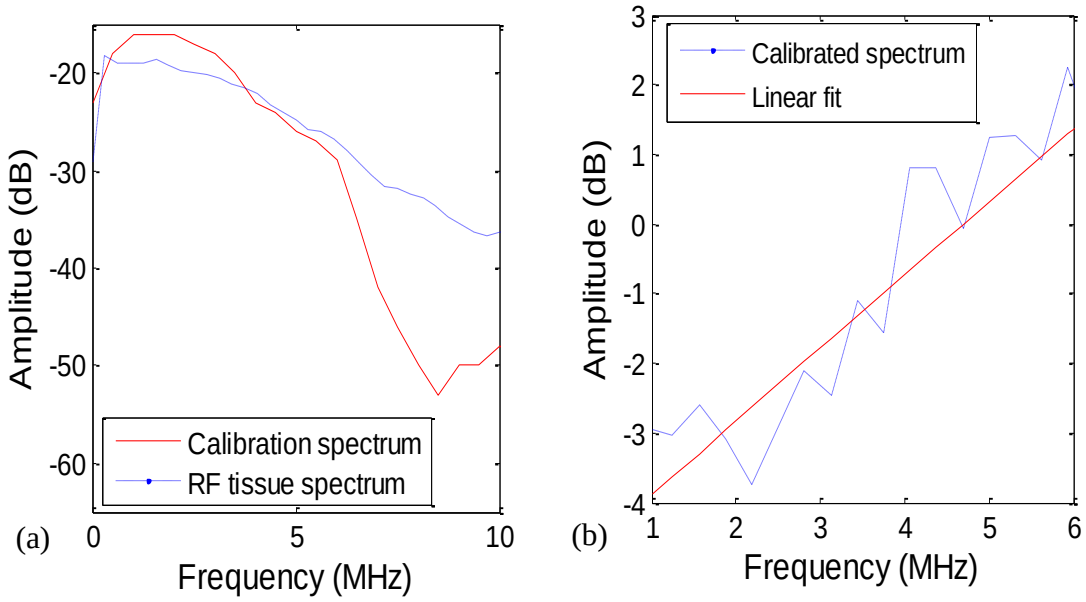

Figure 3.2: Representative power spectrums. a) uncalibrated radio frequency tissue spectrum and calibration spectrum of the 5 MHz transducer, b) The calibrated tissue power spectrum and linear fit applied between 1 and 6 MHz

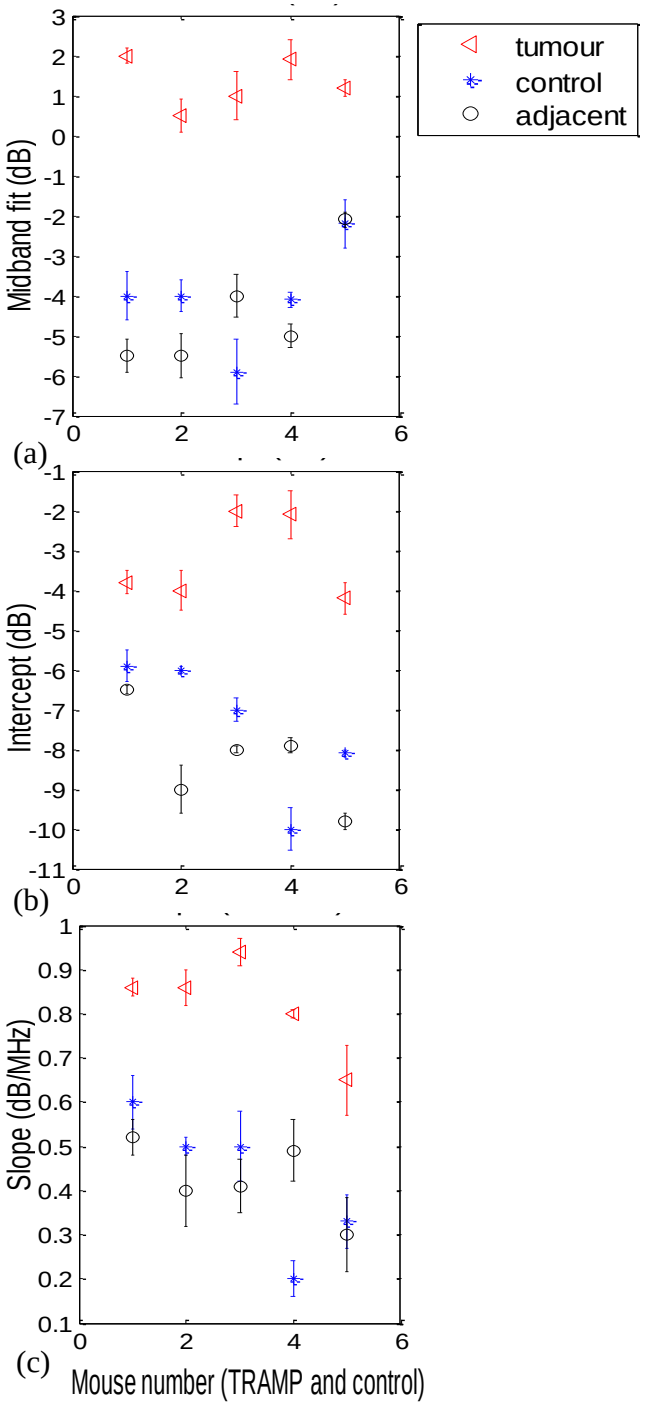

Figure 3.3: Spectral parameters on tumor and adjacent to tumor for each TRAMP mouse and age-matched control mouse. Each value represents an average of spectral parameters acquired within a 2 mm by 2 mm by 2 mm region of interest.

Table 3.2 Average and standard deviations of spectral parameters on tumour and adjacent to tumour for all TRAMP and for all control mice. N=5.

Spectral Parameter	Control	Adjacent	Tumour	t-test (p value) tumour/control	tumour/adjacent
OA midband fit (dB)	-5±1	-5±1	1±1	0.0114	0.0040
OA slope (dB/MHz)	0.4±0.1	0.4±0.1	0.8±0.1	0.0026	<0.001
OA intercept (dB)	-7±2	-8±1	-3±1	0.0155	<0.001

OA = optoacoustic

A cross-sectional profile of the slope across the lateral dimension of a representative tumour is shown in Figure 3.4. Slope values are independent of signal strength (provided the SNR is adequate) and would remove the need to correct for optical attenuation. Therefore, analyzing slope values may be a more robust method of identifying tumour boundaries. The image shows that there is a gradual increase in slope values from the boundaries of the tumour to the center and variation within.

3.4 Discussion and Conclusions

The goal of this study was to demonstrate the potential of optoacoustic imaging to distinguish neoplastic prostate tissue in a transgenic tumour model from normal tissue in a control model. This potential was confirmed in so far as amplitude and RF frequency parameters of the OA signals showed significant differences between cancerous and normal tissues. The results may arise from the principle that the amplitude of the OA signal is largely affected by the optical absorption of the target (determined by e.g. blood vessel size, oxygenation status) while the frequency parameter may be more related to the geometrical properties of absorbing structures (e.g. blood vessel size, oxygenation status and spatial distribution) [32].

By integrating the OA signal within an ROI, two-dimensional OA images of the maximum tumour dimensions were generated and resulted in contrast values of 31 dB to 36 dB. The OA predicted dimensions agree with the true dimensions to within 0.5 mm. Further data from an increased number of animals may allow a more precise estimate of these variables to facilitate calibration of the OA data analysis.

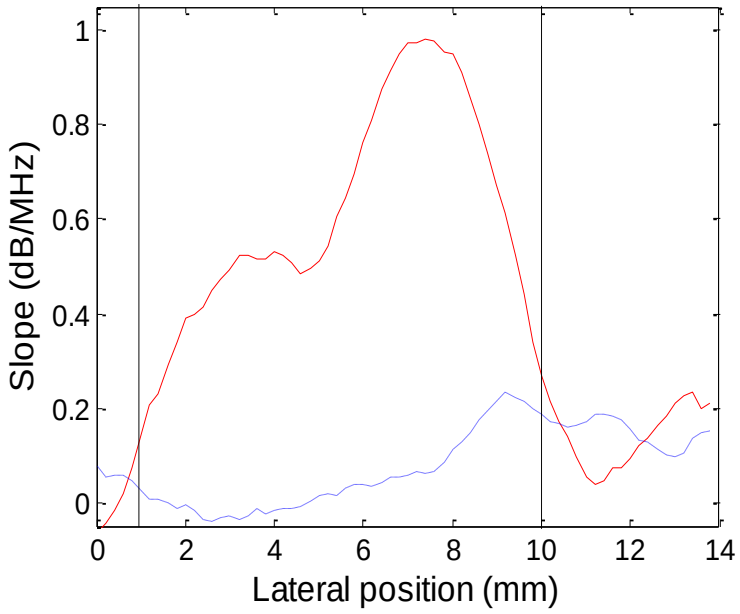

Figure 3.4: Representative slope (dB/MHz) values across the lateral direction through a tumor in the TRAMP model (red) and in the control animal (blue). Vertical lines represent the boundaries of the tumor obtained from full width half max measurements on the OA amplitude images**.**

Theoretical models relating the spectral intercept and slope for conventional ultrasound RF data and the tissue scattering structures have been well established [8,29]. For conventional ultrasound imaging, the spectral parameters, slope, intercept and midband fit are related to the physical characteristics of the target scatterer (e.g. the size, shape, acoustic impedance and spatial distribution of the scatterering sources) [8]. The primary absorbing target for optoacoustic application in this paper was hemoglobin, which is localized in blood vessels.

The axial position of the front surface of the tumour in the OA image correlated to within 0.5 mm of the position measured during cryosectioning. The two-dimensional raster scan method of acquiring OA signals results in limited axial penetration depth due to the large optical attenuation in tissue (especially in tumour tissues due to elevated hemoglobin concentration) [44]. To account for this optical attenuation, a depth dependent signal correction factor was applied to the OA signals prior to analysis.

The amplitude of the OA signal strongly affects the amplitude of the frequency spectrum, thereby affecting the midband fit and intercept values while the slope should be independent of amplitude (provided the signal to noise is adequate) [48]. The OA signal amplitude is depth dependent due to high optical attenuation in tissues. For example, tumours with similar optoacoustic characteristics but positioned at different depths may yield different midband and intercept values. Hence, correcting for changes in fluence for variable target (ie. tumour) depths is important. The depth dependent signal correction applied to the OA signals in this study represents an initial approach towards accounting for the optical attenuation. Significant differences between spectral parameters were found with and without the correction factor (data not shown).

Differences in spectral parameters of neoplastic tissue compared with healthy tissue have been reported for ultrasound RF data [49]. Neoplastic tissues have different microstructure than that of healthy tissue, for example, neoplastic tissues are often denser than normal tissue and consist of more tortuous vasculature [50]. This leads to significant differences in the spectral parameters associated with neoplastic tissue compared to many healthy tissues [51]. Use the methods described in this chapter, the authors were also able to differentiate between control and neoplastic prostate tissue.

A similar spectrum analysis technique for optoacoustics has been reported by Kumon et al. (2011) who found a significant increase in the midband fit between on and off tumour but no significant differences for the intercept and slope [52]. Kumon et al. (2011) found midband fit values were 8.8 dB higher on tumour compared with adjacent normal tissue. Similarily, we found midband fit values were 6 dB higher on tumour compared with adjacent tissue. The slope values presented by Kumon et al. (2001) were 0.5 dB/MHz higher on tumour (with no significant difference between tumour and normal) compared with the slope values of this study which were 0.4 dB/MHz higher on tumour tissue and significantly different from normal tissue. Our study demonstrates significant differences in all three spectral parameters between on and off tumour. Furthermore, control animals were used in this study to ensure that the OA signals adjacent to the tumour were consistent with normal tissues, and not affected by the presence of the tumour.

A two-dimensional image of the slope values across a representative tumour show that there is a gradual increase in the values across the boundaries of the tumour. Slope values are independent of signal strength (provided the SNR is adequate) and

would remove the need to correct for optical attenuation. Therefore, analyzing slope values may be a more robust method of identifying tumour boundaries.

OA imaging has shown promising initial results for detecting the presence of cancerous tumours with high contrast and good resolution compared with conventional ultrasound imaging [10,14,15]. Based upon the findings in the current study, using frequency spectrum analysis in combination with the current amplitude presentation of OA images may offer potentially important information about the tumour (e.g. vascular density, diameter, etc.). In terms of applying these findings in a clinical setting, OA imaging (amplitude presentation) may be used to detect the presence of a tumour and its position in the tissue/organ. Frequency analysis of the RF signals from this tumour could then be performed to obtain further information on its physiological properties which may be indicative of its aggressiveness and treatability. Typical qualitative OA images, using only signal amplitude information, are also subject to a variety of user- and system-dependent factors (e.g. brightness/contrast, thresholding, laser fluence, etc.) that make it difficult to compare between studies [52,53]. Frequency analysis described herein removes many of these factors by compensating for the system response and correcting for loss in optical fluence with depth.

It is acknowledged that the effective acquisition time of this system (~ 1 Hz) is slow for clinical application, and is due to the limitation's of the existing firmware. Future work will involve decreasing this delay time to optimize imaging time while minimizing any detection of signal generated by previous pulses.

Additional studies including a larger number of animals are required to further validate the contrast between tumour, the pre-neoplastic tissue, and healthy prostate as presented in this paper, and to determine the optimal analysis techniques for image generation and boundary determination. A framework for understanding how spectral features are related to tissue physiology will need to be established along with statistical methods for classifying different tissues [29]. Optoacoustic imaging of prostate tumours obtained at varying time points may also demonstrate the capability of these analysis techniques to not only detect the presence of the tumor but to also give an indication of the extent of the disease.

In summary, this study reports that there are significant differences between the amplitude and frequency content of OA signals between tumour and healthy tissue. The increased signal amplitude was attributed to the increased vascularization within the tumour. The differences in the frequency parameters however are likely due to the combination of increased vascularization and vascular heterogeneity (more tortuous and smaller vessels size) of tumour tissues compared to healthy tissues. Frequency analysis, unlike amplitude analysis, of optoacoustic signals provides information about non-resolvable vascular structures, an important consideration since many optoacoustic imaging systems cannot resolve individual blood vessels at the depth of the prostate [27,28]. Knowledge of these vascular characteristics may aid in cancer diagnosis and treatment planning. This report has demonstrated the utility of standard pulse-echo spectrum analysis techniques for optoacoustic characterization of normal and neoplastic tissues. The results of this work contribute to the growing evidence-based support for optoacoustics as a cancer imaging tool.

References

1. El-Gabry, E., Halpern, E. J., Strup, S. E. & Gomella, L. G. Imaging prostate cancer: current and future applications. *Oncology (Williston Park, N.Y.)* **15**, 325–336 (2001).

2. Liu, T. *et al.* A feasibility study of novel ultrasonic tissue characterization for prostate-cancer diagnosis: 2D spectrum analysis of in vivo data with histology as gold standard. *Medical physics* **36**, 3504–3511 (2009).

3. Philipp Dahm, R. D. *Evidence-based Urology*. *Wiley* 245–250 (2010).

4. Swanevelder, J. Resolution in ultrasound imaging. *Continuing Education in Anaesthesia, Critical Care & Pain* **11**, 186–192 (2011).

5. Wijkstra, H., Wink, M. H. & de, la R. Contrast specific imaging in the detection and localization of prostate cancer. *World journal of urology* **22**, 346–350 (2004).

6. Turkbey, B., Pinto, P. A. & Choyke, P. L. Imaging techniques for prostate cancer: implications for focal therapy. *Nature Reviews.Urology* **6**, 191–203 (2009).

7. Robert Ross, M. H. New Clinical Imaging Modalities in Prostate Cancer. *Hematology/oncology clinics of North America* **20**, 811–830 (2006).

8. Feleppa, E. J. *et al.* Recent developments in tissue-type imaging (TTI) for planning and monitoring treatment of prostate cancer. *Ultrasonic imaging* **26**, 163–172 (2004).

9. Frederic, L. L., Ernest, J. F., S, K. A. & Cheri, X. D. Ultrasonic spectrum analysis for tissue evaluation. *Pattern Recognition Letters* **24**, 637–658 (2003).

10. Wang, L. V Ultrasound-mediated biophotonic imaging: A review of acousto-optical tomography and photo-acoustic tomography. *Disease markers* **19**, 123–138 (2003).

11. Mamou, J. & Oelze, M. L. *Quantitative Ultrasound in Soft Tissues*. 350 (Springer: 2013).

12. Cheong, W.-F., Prahl, S. A. & Welch, A. J. A review of the optical properties of biological tissues. *SPIE Milestone series* **102**, 129 (1995).

13. Lashkari, B. & Mandelis, A. Comparison between pulsed laser and frequency-domain photoacoustic modalities: signal-to-noise ratio, contrast, resolution, and maximum depth detectivity. *The Review of scientific instruments* **82**, 94903 (2011).

14. Esenaliev, R. O., Karabutov, A. A. & Oraevsky, A. A. Sensitivity of laser opto-acoustic imaging in detection of small deeply embedded tumors. *IEEE Journal of Selected Topics in Quantum Electronics* **5**, 981 (1999).

15. Oraevsky, A. A. *et al.* Laser optoacoustic imaging of the breast: detection of cancer angiogenesis. *Proceedings - SPIE* **3597**, 352–363 (1999).

16. Sarntinoranont, M., Rooney, F. & Ferrari, M. Interstitial Stress and Fluid Pressure Within a Growing Tumor. *Annals of Biomedical Engineering* **31**, 327–335 (2003).

17. Shah, J. *et al.* Photoacoustic imaging and temperature measurement for photothermal cancer therapy. *Journal of Biomedical Optics* **13**, 34024 (2008).

18. Lao, Y., Xing, D., Yang, S. & Xiang, L. Noninvasive photoacoustic imaging of the developing vasculature during early tumor growth. *Physics in Medicine and Biology* **53**, 4203–4212 (2008).

19. Hu, S. & Wang, L. V Photoacoustic imaging and characterization of the microvasculature. *Journal of Biomedical Optics* **15**, 11101 (2010).

20. Zhang, C., Maslov, K. & Wang, L. V Subwavelength-resolution label-free photoacoustic microscopy of optical absorption in vivo. *Optics Letters* **35**, 3195–3197 (2010).

21. Laufer, J., Zhang, E., Raivich, G. & Beard, P. Three-dimensional noninvasive imaging of the vasculature in the mouse brain using a high resolution photoacoustic scanner. *Applied Optics* **48**, D299–D306 (2009).

22. Laufer, J. *et al.* In vivo longitudinal photoacoustic imaging of subcutaneous tumours in mice. *Proceedings of SPIE* **7899**, 789915 (2011).

23. Saha, R. K., Karmakar, S., Hysi, E., Roy, M. & Kolios, M. C. Validity of a theoretical model to examine blood oxygenation dependent optoacoustics. *Journal of Biomedical Optics* **17**, 55002 (2012).

24. Lizzi, F. L., Greenebaum, M., Feleppa, E. J., Elbaum, M. & Coleman, D. J. Theoretical framework for spectrum analysis in ultrasonic tissue characterization. *The Journal of the Acoustical Society of America* **73**, 1366–1373 (1983).

25. Zalev, J. & Kolios, M. C. Detecting abnormal vasculature from photoacoustic signals using wavelet-packet features. *Proceedings of SPIE* 78992M (2011).

26. Hall, T. L., Hempel, C. R., Sabb, B. J. & Roberts, W. W. Acoustic Access to the Prostate for Extracorporeal Ultrasound Ablation. *Journal of Endourology* **24**, 1875–1881 (2010).

27. Xu, X.-H. & Li, H. Photoacoustic imaging in biomedicine. *Physics - Beijing* **37**, 111–119 (2008).

28. Song, K. H. & Wang, L. V Deep reflection-mode photoacoustic imaging of biological tissue. *Journal of Biomedical Optics* **12**, 60503 (2007).

29. Lizzi, F. L. *et al.* Ultrasonic spectrum analysis for tissue assays and therapy evaluation. *International Journal of Imaging Systems & Technology* **8**, 3–10 (1997).

30. Kolios, M. Biomedical ultrasound imaging from 1 to 1000 MHz. *Canadian Acoustics* **37**, 35–43 (2009).

31. Lizzi, F. L., Astor, M., Feleppa, E. J., Shao, M. & Kalisz, A. Statistical framework for ultrasonic spectral parameter imaging. *Ultrasound in medicine & biology* **23**, 1371–1382 (1997).

32. Diebold, G. J., Beveridge, A. C. & Hamilton, T. J. The photoacoustic effect generated by an incompressible sphere. *The Journal of the Acoustical Society of America* **112**, 1780–1786 (2002).

33. Gertsch, A. G., Bush, N. L., Birtill, D. C. C. & Bamber, J. C. Toward characterizing the size of microscopic optical absorbers using optoacoustic emission spectroscopy. *BiOS* 75641M–75641M–10 (2010).

34. Silverman, R. H. *et al.* Spectral parameter imaging for detection of prognostically significant histologic features in uveal melanoma. *Ultrasound in Medicine & Biology* **29**, 951–959 (2003).

35. Gingrich, J. R., Barrios, R. J., Foster, B. A. & Greenberg, N. M. Pathologic progression of autochthonous prostate cancer in the TRAMP model. *Prostate Cancer & Prostatic Diseases* **2**, 70 (1999).

36. Gingrich, J. R. *et al.* Metastatic prostate cancer in a transgenic mouse. *Cancer research* **56**, 4096–4102 (1996).

37. Eng, M. H. *et al.* Early castration reduces prostatic carcinogenesis in transgenic mice. *Urology* **54**, 1112–1119 (1999).

38. Shappell, S. B. *et al.* Prostate Pathology of Genetically Engineered Mice: Definitions and Classification. The Consensus Report from the Bar Harbor Meeting of the Mouse Models of Human Cancer Consortium Prostate Pathology Committee. *Cancer research* **64**, 2270–2305 (2004).

39. Passler, K., Nuster, R., Gratt, S., Burgholzer, P. & Paltauf, G. Piezoelectric annular array for large depth of field photoacoustic imaging. *Biomedical optics express* **2**, 2655–64 (2011).

40. Passler, K., Nuster, R., Gratt, S., Burgholzer, P. & Paltauf, G. Annular piezoelectric ring array for photoacoustic imaging. *European Conferences on Biomedical Optics* 809012–809012–7 (2011).

41. *American National Standard for the safe use of lasers / secretariat, the Laser Institute of America*. (Orlando, FL : The Institute, c1993: 1993).

42. Xi, L. *et al.* Photoacoustic imaging based on MEMS mirror scanning. *Biomedical Optics Express* **1**, 1278 (2010).

43. Cox, B., Laufer, J. G., Arridge, S. R. & Beard, P. C. Quantitative spectroscopic photoacoustic imaging: a review. *Journal of Biomedical Optics* **17**, 061202 (2012).

44. Arnfield, M. R., Chapman, J. D., Tulip, J., Fenning, M. C. & McPhee, M. S. Optical properties of experimental prostate tumors in vivo. *Photochemistry and photobiology* **57**, 306–311 (1993).

45. de, la Z. *et al.* Ultrahigh sensitivity carbon nanotube agents for photoacoustic molecular imaging in living mice. *Nano Letters* **10**, 2168–2172 (2010).

46. Bouchard, L.-S. *et al.* Picomolar sensitivity MRI and photoacoustic imaging of cobalt nanoparticles. *Proceedings of the National Academy of Sciences of the United States of America* **106**, 4085–9 (2009).

47. Strohm, E., Gorelikov, I., Matsuura, N. & Kolios, M. Photoacoustic spectral characterization of perfluorocarbon droplets. *SPIE BiOS* 82232F–82232F–8 (2012).

48. Silverman, R., Kong, F., Lloyd Harriet & Y. C. Chen Fine-resolution photoacoustic imaging of the eye. *Proceedings of SPIE* **7564**, 8 (2010).

49. Mamou, J. *et al.* Original Contribution: Three-Dimensional High-Frequency Backscatter and Envelope Quantification of Cancerous Human Lymph Nodes. *Ultrasound in medicine & biology* **37**, 345–357

50. Folkman, J. Tumor angiogenesis: therapeutic implications. *The New England journal of medicine* **285**, 1182–1186 (1971).

51. Banihashemi, B. *et al.* Ultrasound imaging of apoptosis in tumor response: novel preclinical monitoring of photodynamic therapy effects. *Cancer research* **68**, 8590–8596 (2008).

52. Kumon, R. E., Deng, C. X. & Wang, X. Frequency-Domain Analysis of Photoacoustic Imaging Data From Prostate Adenocarcinoma Tumors in a Murine Model. *Ultrasound in medicine & biology* **37**, 834–839 (2011).

53. Montilla, L. G., Olafsson, R., Bauer, D. R. & Witte, R. S. Real-time photoacoustic and ultrasound imaging: a simple solution for clinical ultrasound systems with linear arrays. *Physics in medicine and biology* **58**, N1–12 (2013).

CHAPTER 4

OPTOACOUSTIC SIGNAL AMPLITUDE AND FREQUENCY SPECTRUM ANALYSIS OF LASER HEATED BOVINE LIVER *EX VIVO*

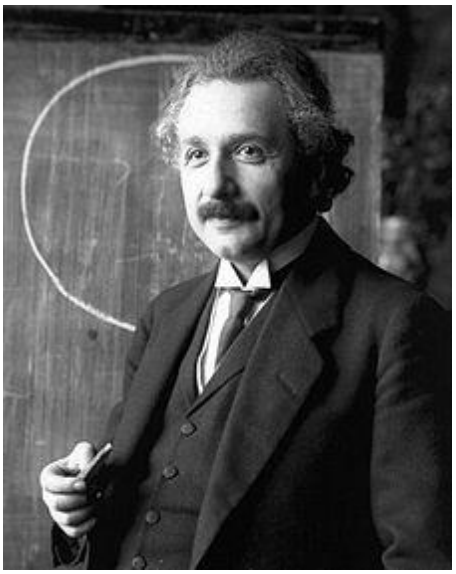

"There are only two ways to live your life. One is as though nothing is a miracle. The other is as though everything is a miracle."
-Albert Einstein (1879-1955)
picture from http://www.goodreads.com/author/show/9810.Albert_Einstein

Summary

Frequency analysis of optoacoustic (OA) signals has been investigated for the direct detection of tissue thermal damage for the purpose of monitoring laser thermal therapy (LTT). Spectrum analysis is commonly performed on ultrasound backscatter radio frequency (RF) data, which calculates the spectral midband fit, slope, and the intercept of the data, and was used to quantify the frequency changes in the OA RF signal. The potential to monitor tissue damage directly and in real-time, using OA imaging is desirable, rather than through a surrogate of temperature. OA images were acquired from ex vivo bovine liver using a reverse-mode OA imaging system consisting of a pulsed laser operating at 775 nm and an 8 element annular array ultrasound transducer. LTT was performed with an 810 nm laser at 4 W for 5 minutes. OA signals were acquired for 2 minutes prior to, 5 minutes during, and 7 minutes post treatment at a rate of 2 Hz. Heat induced effects were identified based on the OA signal amplitude in combination with spectral analysis of the OA radio frequency (RF) data.

In agreement with previous work, the OA signal amplitude was strongly affected by the temperature of the target and increased continuously as the heat was applied. The spectral midband fit and intercept increased to a maximum within three minutes of heating then remained at this maximum for the duration of the experiment (even as the temperature of the sample decreased). The spectral slope decreased to a minimum within two minutes of heating and remained at this value for the duration of the experiment.

The midband fit and intercept increased on average by 7 dB and 9 dB respectively, and the slope decreased on average by 0.3 dB. The amplitude of the OA signals post-treatment was on average three times higher compared with pre-treatment signals.

The results of this study demonstrate that analysis of OA frequency components may prove to be a more direct measure of tissue damage, than temperature. Such OA frequency analysis in combination with OA thermometry may prove to be an improved strategy for monitoring laser thermal therapy.

4.1 Introduction

Laser Thermal Therapy (LTT) is a minimally invasive technique for destroying diseased tissue. The feasibility of LTT as a tool for selective tissue destruction has been demonstrated in a number of sites including the breast [1], brain [2,3], liver [4,5] and prostate [6,7]. Thermal therapy involves heating tissue to between 55 and 90^{o}C for several minutes resulting in cell death [8]. Cell death occurs when thermal damage results in irreversible denaturation of proteins (i.e. coagulation), typically at temperatures above 55^{o}C. Contrary to other approaches such as hyperthermia (heating tissues between 41-45^{o}C), thermal therapy may act as a stand-alone therapy.

Heating tissues to induce cellular death results in highly variable outcomes which can result in insufficient (leading to recurrence) or overly aggressive treatment (morbidity of surrounding healthy tissues) [9]. These risks necessitate precise and continuous monitoring during treatment [10]. For prostate treatments, real-time monitoring offers the possibility of ensuring that the entire tumour has been destroyed while peri-prostatic critical structures are spared.

Several non-invasive techniques have been used for monitoring tissue temperatures during LTT including point sensors (e.g. thermocouples, fluoroptic probes) [11], magnetic resonance imaging (MRI) [12,13], ultrasound imaging [14,15] and photoacoustic (i.e. optoacoustic) imaging[16,17]. Point sensors provide temperature information at specific locations, hence offer only a limited data set for monitoring. Furthermore, temperature monitoring using point sensors has proven to be inadequate due to the time delay in the conduction of thermal energy from the heating source to the temperature probe [8]. This may result in temperatures exceeding safe limits close to the heating

source before they are detected by the temperature probes resulting in undesirable tissue charring [18].

MRI thermometry provides real-time, three-dimensional maps of tissue temperature [2]. Unfortunately, significant image artifacts often arise from patient movement, which necessitates constant recalibration [19]. This type of monitoring is also generally cost-prohibitive for most treatment centers [20].

Ultrasound monitoring provides real-time imaging, and is relatively cost effective. However it suffers from low contrast for coagulation monitoring, because the speed of sound in coagulated tissue is similar to that of native tissue [21,22]. MRI thermometry is also expensive and logistically challenging for temperature measurements in a clinical setting due to need for repeated calibrations due to patient movement [23,24].

Optoacoustic (OA) imaging exposes tissues to nanosecond pulsed laser light, which induces tissue generated acoustic waves which can be detected using wide band transducers [25,26]. OA imaging can provide three-dimensional information in real-time with high contrast and deep penetration depth [27,28]. The amplitude of an OA signal is dependent upon the Grüneisen parameter, which increases with temperature. The amplitude is also dependent on the optical absorption properties of the target tissues, and therefore provides the opportunity to take advantage of the significant changes in tissue optical properties, at wavelengths in the visible and near infrared (NIR) range, due to thermal coagulation [11].

The frequency content of the generated OA sound waves is broadband, but the detected signals are limited by the finite bandwidth of the ultrasound imaging

transducers (detection range) and the frequency dependent attenuation of ultrasound in tissues [29]. The frequency components of the signals may depend on anatomical properties of the absorbing structures in a manner somewhat similar to conventional ultrasound imaging [30–32].

In this work, we hypothesize that the physical changes which occur in the tissue during coagulation, such as the constriction of blood vessels, increased optical scattering, changes to the Grűneisen parameter, and protein unfolding [33], may influence the frequency content of the OA wave generation and be detected using spectrum analyzing techniques commonly performed on ultrasonic backscatter RF data [34].

4.2 Materials and Methods

4.2.1 Imaging protocol

Sixteen randomly selected liver samples obtained from 8 different bovine livers (purchased from a local butcher) were cut to approximately 2 cm by 2 cm with 1 cm thickness and vacuum sealed inside a clear plastic bag (Figure 4.1). Bovine liver was chosen because its optical properties ($\mu_a \approx 3$ cm^{-1} and $\mu_s \approx 5$ cm^{-1} at 775 nm) have been reported to be representative of a highly vascularized tumour ($\mu_a \geq 2$ cm^{-1} and $\mu_s \geq 5$ cm^{-1} at 775 nm) [35].

Each liver sample was secured inside the waterbath (held at 38 °C) of a reverse-mode optoacoustic imaging system (Seno Medical Instruments Inc., San Antonio, TX) (Figure 4.2). The system consisted of an Nd:YAG pumped Ti:Sapphire laser operating at 775 nm and an 8 element annular array piezo-electric transducer with a nominal central frequency of 5 MHz (-6dB bandwidth of 60%). A bifurcated optical fiber bundle delivered 6 ns pulses at a 10 Hz repetition rate and 12 mJ of energy per pulse, for a

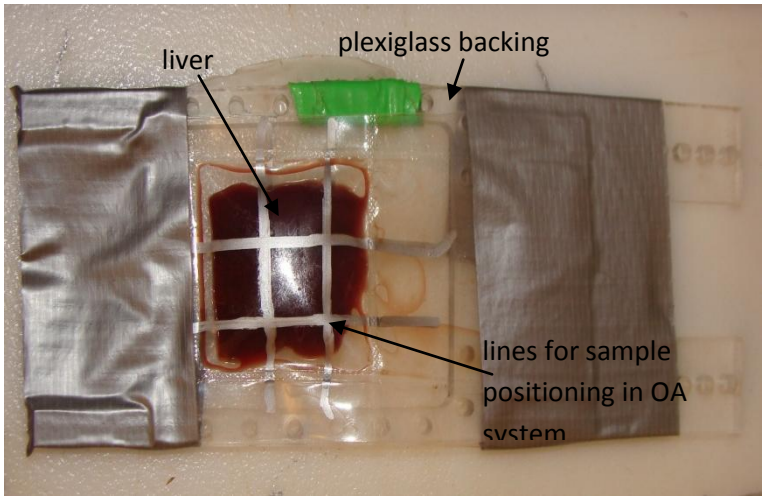

Figure 4.1*:* A representative bovine liver sample cut to approximately 2 cm by 2 cm by 1 cm thickness post-heating. Each sample was sealed inside a clear plastic bag and secured to a holder during the image acquisition. Lines were drawn on the plastic bag, using a metallic permanent marker, forming a box of 3 mm by 3 mm for easier positioning.

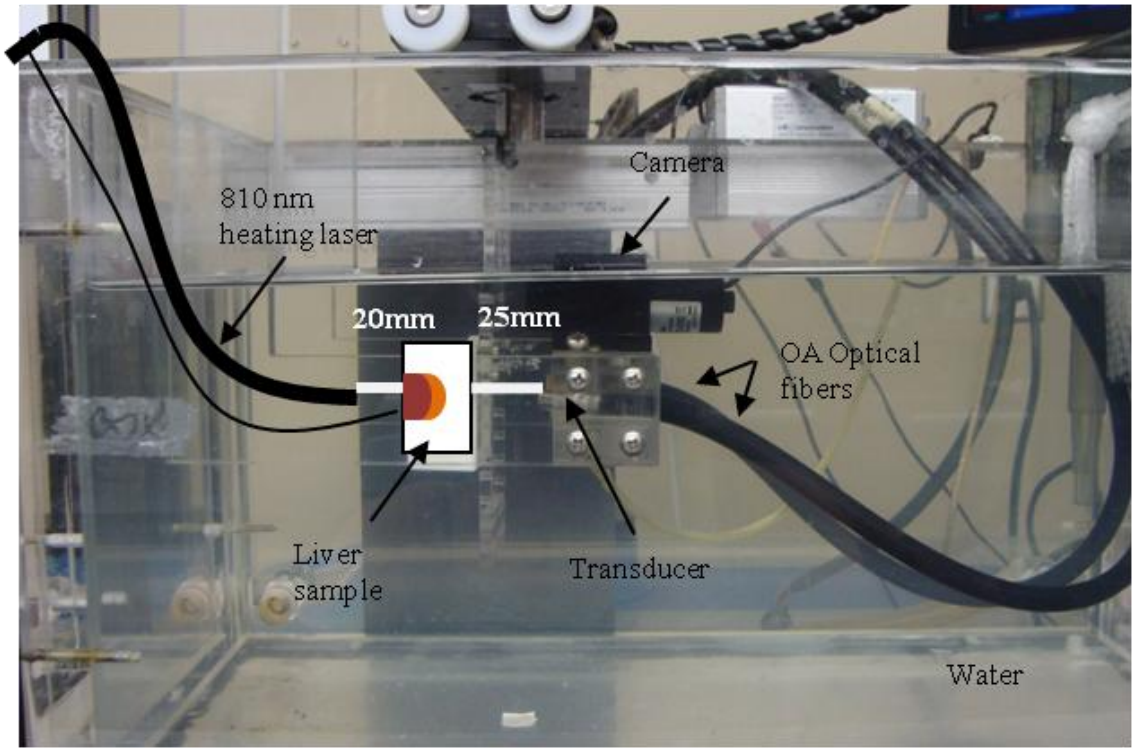

Figure 4.2: Photograph and schematic of the Imagio small animal optoacoustic imaging system setup. Laser optical path intercepts at 25 mm from the transducer which is located beneath a camera used for image positioning. The sample remained stationary as optoacoustic signals were acquired at one point over 14 minutes including 2 minutes prior to heating, 5 minutes during 4W laser heating and 7 minutes post heating

surface irradiance of 0.19 W/cm^2. The bifurcated fiber bundle and transducer array were positioned 2 cm from the surface of the liver sample

An 810 nm laser (BWF2, BWTEK, Inc) with a maximum power output of 15 W was used to deliver the thermal therapy. The laser fiber was positioned in the water bath approximately 2 cm from the opposite side of the liver sample, along the same axis as the OA transducer array. This resulted in an illuminated area on the samples surface of approximately 1 cm in diameter. The liver irradiation was performed at 4 W for 5 minutes. A calibrated fluoroptic temperature probe (Lumasense Technologies, CA) (icebath calibrated) was placed along the same axis as the center of the 810 nm laser beam and OA transducer on the surface of the sample facing the 810 nm laser to measure the surface temperature of the sample. Once aligned, the transducer array position was fixed for the entire period of heating. Prior to OA imaging the fluoroptic probe was used to ensure that the liver sample had equilibrated to 38^{o}C (core body temperature of a murine animal). During laser heating, the temperature was measured every one second.

A-lines (2 signals/second) were acquired along the axis of the 810 nm laser with no temporal averaging. OA signals were acquired for 2 minutes prior to heating to obtain baseline data for the liver sample. The tissue was then exposed to the 810 nm laser for 5 minutes while OA data was continuously acquired. A 5 minute exposure duration was used which created 1 cm wide and 0.5 cm deep lesions at the heated surface of the sample. The 810 nm laser was then turned off and OA signals were acquired for 7 minutes during which time the temperature of the liver sample decrease to below 43^{o}C, as measured by the fluoroptic probe.

4.2.2 Data Analysis

A MATLAB® (The MathWorks Inc., MA) based script was developed and used for the analysis of both amplitude and spectral components of the OA signals. The Hilbert transform was applied to all RF data [36–38]. The OA signals from a time window that represents tissue from 27 mm and 32 mm from the transducer was used. This window excluded the typically strong OA signals obtained from tissue surfaces[39] and included all signals within the 0.5 cm of liver tissue that was thermally damaged. An integration of each A-line between 27 mm and 32 mm was performed. The average OA signal obtained prior to laser exposure was divided from all OA signals to remove the baseline signal originating from the untreated tissue.

To obtain the sensitivity of the transducer at different frequencies**,** a calibrated power spectrum was obtained by using a 200 nm thick gold film. The film was deposited onto a thin microscope cover slide with no annealing. A gold film was used because it has a broad OA power spectrum as well as a flat response in the known bandwidth of the transducer, thus providing a measure of the transducer response [40]. OA measurements at 775 nm were obtained across an area of approximately 1 cm by 1 cm using the same power settings as were used for the liver samples. A total of 20 OA signals were recorded. These are referred to as the calibrated power spectra.

For each signal, the FFT was applied to the tissue RF data to calculate the RF echo spectrum. The mean of the squared spectral magnitudes is equivalent to the averaged power spectrum (APS). The APS was converted into the decibel (dB) scale. A calibrated power spectrum was subtracted from the converted APS to remove any

system-specific artifacts caused by the transducer characteristics at the focus and system electronics.

Linear regression was performed on the averaged power spectrum between 1 and 6 MHz and the midband fit, slope, and intercept extracted from the fit. This frequency region was chosen based on the approximate linearity of the dataset and the high signal to noise (SNR of 3.7 dB) within these frequencies. The statistical spread of these parameters for ultrasound RF data has been previously established by others [34].

A region of interest (ROI) of 5 mm by 5 mm by 5 mm centered on the lesion and on the treated side of the sample (the approximate depth in which all the samples were damaged) was chosen for analysis.

During LTT, the clinical goal is to raise the tissue temperature to induce coagulated necrosis. This thermal damage can be quantified using the concept of thermal dose [41]. Thermal dose was calculated using continuous tissue temperature data and as approximated by the cumulative equivalent minutes at 43°C, CEM43°C, model [41–43].

$$CEM43°C = \sum_{i=1}^{n} R^{(43-T)} \Delta t_i \quad (1)$$

Where R is 0.5 when T is greater than 43°C, and 0.25 when T is less than 43°C. T is the temperature during a change in time Δt_i.

Surface temperatures, which were recorded every 1 second using a calibrated fluoroptic probe, were input into the CEM43°C equation to calculate the thermal dose.

The normality of the spectral parameters was confirmed using a Shapiro-Wilk test with W>0.05 used as the criterion for normality [44]. The variances of the spectral

parameters were found to be equal using an *F*-test with F<0.05 used as the criterion for equal variance. A paired t-test was used to compare the spectral parameters between normal and neoplastic tissue. A *p*-value of 0.05 or less was used to define statistically significant differences.

4.3 Results

Each liver sample underwent the same laser treatment protocol which produced coagulated lesions approximately 1 ± 0.2 cm diameter (at the heated surface) and of 0.5 ± 0.1 cm depth. Figure 4.3 shows a representative liver sample post-heating.

Figure 4.4 presents a boxplot of normalized OA signal amplitudes (Hilbert transformed) of 16 liver samples prior to, during and post heating near the surface, as well as the temperatures at the surface of the sample. Figure 4.5 shows the average amplitude values of all 16 samples versus temperature.

Sample temperature prior to imaging was 38°C. Maximum surface temperatures of 60-70^{o}C were measured using the fluoroptic probe (an increase of 22-32°C). The amplitude of the OA signal increased continuously with heading, and reached a maximum that is on average 9 ± 2 times higher than the pre-heating OA signal. With the heat source removed, at 7 minutes, the OA signal decreased for approximately 4 minutes and then leveled off at an amplitude 7 ± 2 times higher than the pre-heating OA

a) 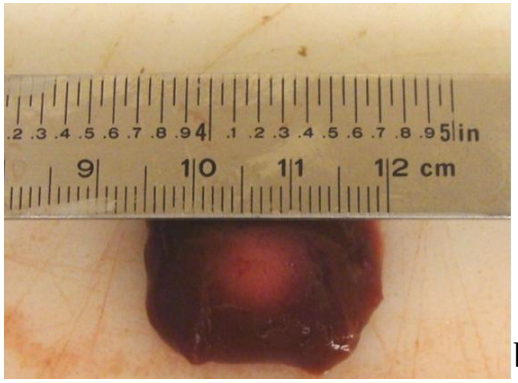 b) 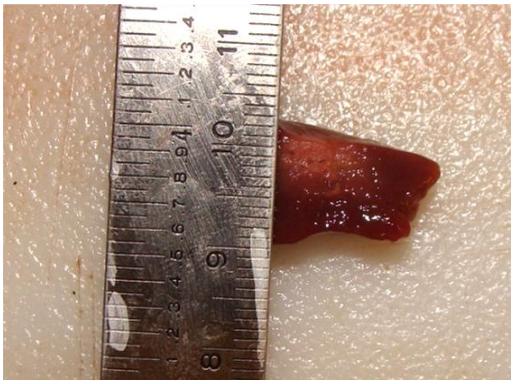

Figure 4.3: A representative bovine liver sample cut to approximately 2 cm by 2 cm by 1 cm post-heating with a) ~1 cm of coagulation on the heated surface, and b) a coagulation depth of ~0.5 cm.

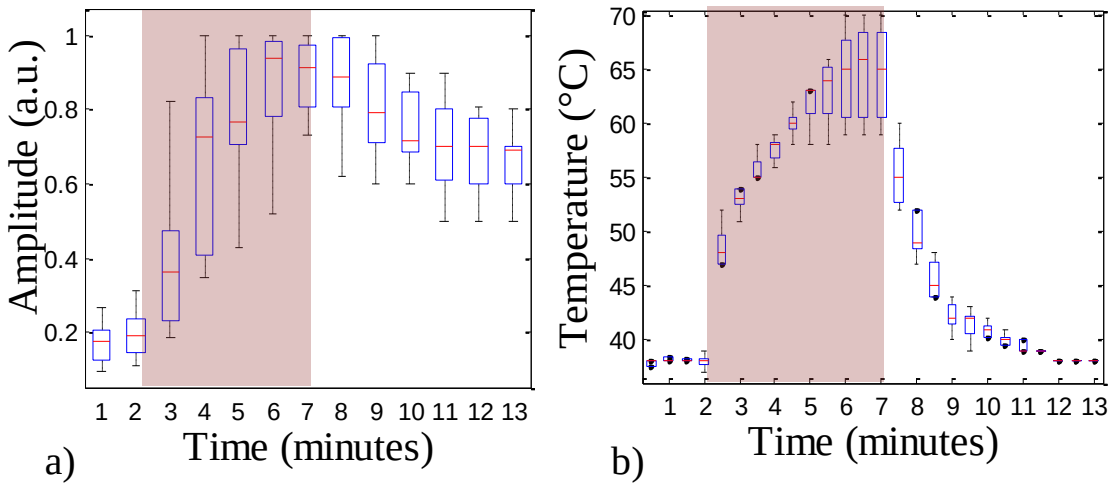

Figure 4.4: Normalized integrated optoacoustic signal (a) and surface temperature measurements (b) versus time of the 16 repeated trials (N=16). The shaded red area represents the time during heating. Boxplot represents mean, one standard deviation and spread of data.

signal. The data presented in Figure 4.5 can also be separated into three different phases, 1) heating without coagulation, 2) heating with coagulation and 3) cooling. The amplitude increased slowly up to the temperature of approximately 53°C, with a slope of 0.008. The sharp increase in the amplitude was detected at temperatures above 53°C where the slope increases to 0.05. This steep increase was considered likely due to the rapid changes in optical scattering coefficient which occur during the coagulation process. During the cooling of the tissue, the amplitude decreased slowly with a slope of 0.01, similar to that during heating without coagulation. Variation was not included in the average data points presented in this figure for easier viewing. Variation in the OA signal strength ranged from 0.05 to 0.2 a.u. Spectral parameters were measured and averaged over one minute intervals and are presented in Figure 4.6.

The midband fit and intercept values increased for approximately three minutes as the heat was applied to the sample and then leveled off at a maximum value of 7 ± 1 dB and 8 ± 1 dB higher than pre-heating values respectively (unlike the OA amplitude which increased continuously during heating). When the laser was turned off and the heat removed (at 7 minutes), the midband fit and intercept values remained at their maximum values (unlike amplitude values which decrease during cooling). The slope values decreased to a minimum within two minutes of heating and remained at this value during and the post-heating phase. The midband fit and intercept values increased until the temperature reached approximately 55°C and then leveled off. The slope values increased until the temperature reached approximately 50°C.

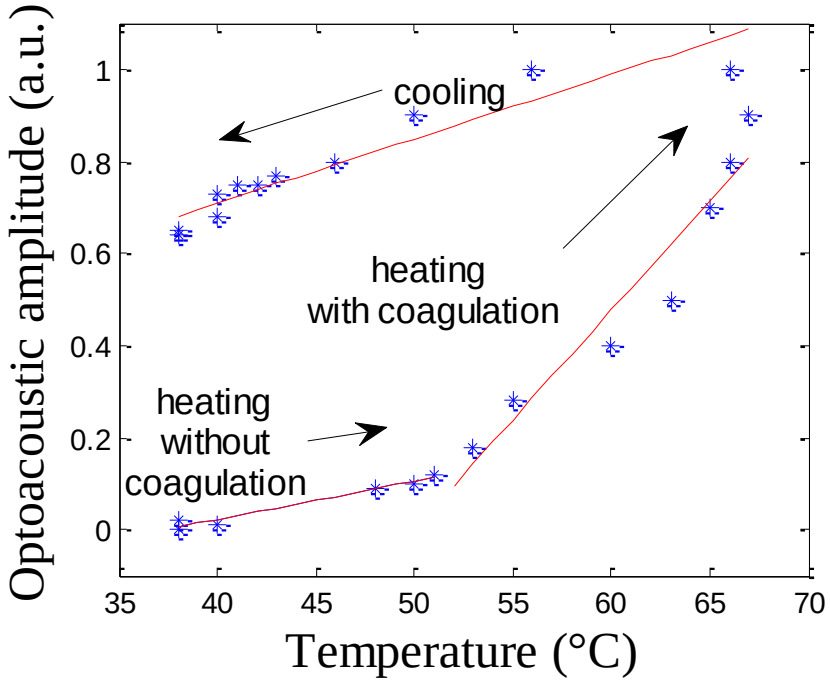

Figure 4.5: Average optoacoustic signal amplitude versus temperature for the 16 repeated heating experiments (N=16). Signals was acquired 2 minutes prior to laser thermal therapy (LTT), 5 minutes during LTT and 7 minutes post LTT in bovine liver ex vivo.

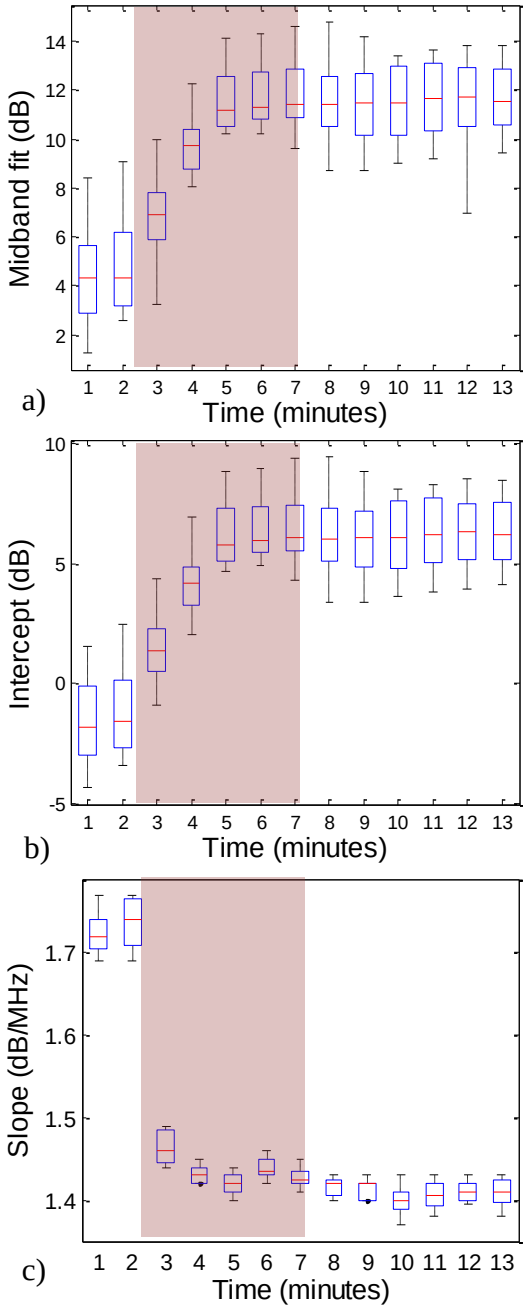

Figure 4.6: Spectral parameters a) midband fit, b) intercept and c) slope) recorded prior to, during and post laser thermal therapy performed on ex vivo bovine hepatic tissue. Shaded area represents the period of laser heating. The shaded red region represents the time of heating. Boxplot represents mean, one standard deviation and spread of data (N=16).

Figure 4.7 presents the average spectral parameter values of the 16 samples versus calculated CEM43°C. Variation was not included in the average data points presented in this figure for easier viewing. Variation in the OA signal strength ranged from 0.05 to 0.2 a.u.

The mean and standard deviations that apply to the OA signal amplitude and each spectral component were calculated prior to heating (0-2 minutes), during heating (2-7 minutes) and post heating (7-14 minutes). A Welch's t-test was applied to the data (α=0.05). Significant differences were found between the amplitude and spectral components prior to and post-heating. Significant differences were not found between any of the parameters during and post-heating. Results are summarized in Table 4.1.

Detectable changes were seen in the amplitude and all three spectral parameters prior to heating compared to during and post laser application. The intercept and midband fit increased by 9 dB and 7 dB respectively and the slope decreased by 0.3 dB post-treatment compared to pre-treatment. Post-treatment, as the tissue returned to its initial temperature, and there were no significant changes in the spectral components compared to those measured during treatment.

4.4 Discussion and Conclusions

The absolute OA amplitude is largely affected by the position of the transducer in relation to the sample [16]. Therefore, the OA signals from each sample were normalized to account for small discrepancies in the transducer placement.

The amplitude of the OA signal is strongly affected by the temperature of the target [21,45]. As shown in Figure 4.4, the OA signal increases continuously as heat is

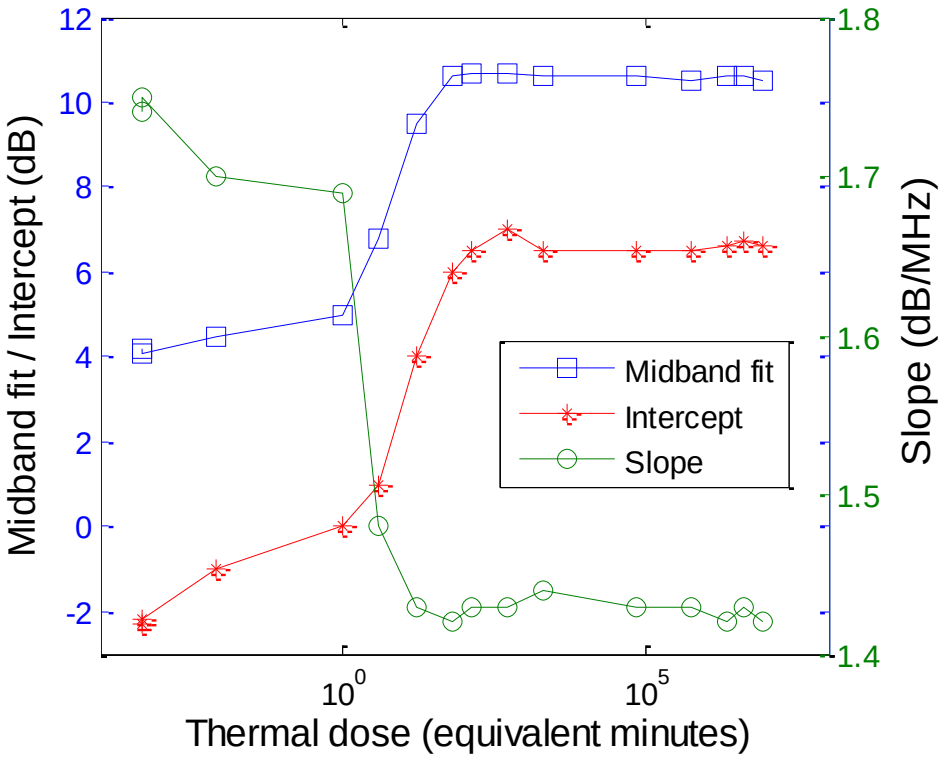

Figure 4.7: Spectral parameters versus calculated thermal dose at 43°C from the averaged temperature during heating of 16 repeated trials (N=16).

Table 4.1: Averages and standard deviations of OA signal amplitude and spectral components prior to, during and post laser heating of *ex vivo* bovine liver tissues (N=16).

Spectral Parameter	Prior to heating	During heating	Post heating	t-test (p value)		
				prior/ during	prior/ post	during/ post
OA midband fit (dB)	5±1	10±2	12±1	<0.001	<0.001	0.0721
OA slope (dB/MHz)	1.73±0.04	1.43±0.03	1.42±0.02	<0.001	<0.001	0.4159
OA intercept (dB)	-2±1	5.2±2	7±1	<0.001	<0.001	0.0753
OA signal amplitude (a.u.)	0.01±0.02	0.7±0.3	0.7±0.2	<0.001	<0.001	0.4385

being applied. Below 53°C the amplitude increases slowly, then around 55°C it increases more sharply. This two-step increase in amplitude during heating has been reported by others [46], and is likely due to the rapid changes in optical scattering which occurs during coagulation. Amplitude reaches a maximum value 9 times higher than signals prior to heating. Increases similar to this of 2-4 times higher amplitude post-treatment compared with pre-treatment have been reported by others [46,47]. When the laser is turned off and the temperature of the sample returns to its initial temperature, the amplitude does not decrease to its initial value, but remains 7 times higher than signals prior to heating. This is indicative of a permanent change in a tissue property sensitive to OA wave generation (i.e. coagulation) including the optical absorption and scattering coefficients, and Griuneisen parameter of the target [11,17]. Increased signal post-treatment, after the tissue returns to its initial temperature, has also been reported by others [46].

The midband fit and intercept increased during laser heating of the liver (to maximum of 7 and 8 dB higher than pre-treatment values). However, unlike the OA amplitude values, these components reached a maximum after approximately three minutes of heating and remained at that maximum even when the laser is turned off and the sample returns to its initial temperature. Although these components are affected by the amplitude of the OA signal (and therefore the temperature of the target), they are more strongly affected by the tissue state which is made apparent by the fact that post-treatment, as the temperature decreases, these frequency components remain stable. We posit that as the tissue coagulation is initiated, the components increase to a maximum value, within 2-3 minutes, which indicates that the majority of the tissue within the ROI

had reached a state of coagulation, and the components remain at this value even as the temperature continues to increase within the sample. During the first 2 minutes of treatment, the coagulation zone commonly increases rapidly in diameter and then slows down as heating continues [46,48]. The slope decreased to a minimum (0.31 dB less than pre-treatment values) within 2 minutes of heating. This parameter may be an even more sensitive measure of tissue change as it is not affected by the amplitude of the OA signal (and thus it is likely not affected by the tissue temperature directly). The calculated thermal dose versus the spectral parameter values shows that the three parameters reach a 'steady state' at approximately 120 equivalent minutes at 43°C (within the range of thermal dose at which liver tissue coagulates *ex vivo*). When the CEM_{43} value exceeds a critical threshold, the tissue is considered to be thermally coagulated. Thresholds for CEM_{43} have been tabulated in the literature for several types of tissue based upon experimental observation of tissue injury at 43°C. The critical threshold value for *ex vivo* liver tissue ranges from 80 to 340 equivalent minutes at 43°C [41,42].

When the laser is turned off the frequency components are not affected likely because the tissue remains in a coagulated state even as its temperature decreases. It is known that the frequency of an OA signal depends on the physical characteristics of the target, therefore, as the physical characteristics of the target change (e.g. due to coagulation) we should expect to see changes to the frequency. However, there is still a need to better understand the sensitivity among the frequency metrics and the tissue property changes during heating. Future experiments will aim at understanding these relationships.

Changes to the pressure amplitude (OA signal) with temperature increase is greater than the changes in acoustic properties and the chemical content of the tissue [46]. Therefore, OA imaging has the potential to be more sensitive to temperature changes than ultrasound imaging. The sensitivity of OA amplitude, however, is dependent on the number of signals which can be acquired and often the number of signals acquired is limited by the necessity to achieve practical imaging time [16]. An additional challenge with using OA amplitude to monitor temperature is that as the tissue coagulates, its optical and physical properties change, and thus, the amplitude is affected by both the changing temperature and the changing optical and physical properties of the tissue during coagulation [47]. It has proven difficult to decouple the influences of thermally induced changes in tissue optical and physical property (which are tissue- specific) and that of temperature on OA signals acquired during tissue heating. The frequency analysis of OA signals described herein provides an additional analysis technique which is shown to be more sensitive than amplitude at detecting changes to the tissue during heating (which would allow for smaller sample size without sacrificing sensitivity). Furthermore, the frequency components are not highly affected by temperature, and thus, we propose they are affected by the changes to the optical and physical properties of the tissue.

Overall the results of this study demonstrate that while the OA amplitude is sensitive to temperature changes, the frequency components of the OA signals may prove to be a more direct measure of tissue damage. Such OA frequency analysis in combination with OA thermometry may prove to be an improved strategy for monitoring laser thermal therapy.

References

1. van Hillegersberg, R., van Staveren, H. J., Roggan, A., Müller, G. & IJzemans, J. Interstitial laser photocoagulation as a treatment for breast cancer. *The British journal of surgery* **82**, 856 (1995).

2. Schrottner, O., Ascher, P. W. & Ebner, F. Interstitial laser thermotherapy of brain tumour under MRI control. *Fifth Int. Congress of the European Laser Association* (1990).

3. Roux, F. *et al.* Laser interstitial thermotherapy in stereotactical neurosurgery. *Lasers in Medical Science* **7**, 121 (1992).

4. Hahl, J., Haapiainen, R., Ovaska, J., Puolakkainen, P. & Schröder, T. Laser-Induced hyperthermia in the treatment of liver tumors. *Lasers in Surgery & Medicine* **10**, 319 (1990).

5. Dowlatshahi, K., Bhattacharya, A. K., Silver, B., Matalon, T. & Williams, J. W. Percutaneous interstitial laser therapy of a patient with recurrent hepatoma in a transplanted liver. *Surgery* **112**, 603–606 (1992).

6. Stern, J. M., Stanfield, J., Kabbani, W., Hsieh, J.-T. & Cadeddu, J. A. Investigative urology: Selective Prostate Cancer Thermal Ablation With Laser Activated Gold Nanoshells. *The Journal of urology* **179**, 748–753 (2008).

7. Jason Stafford, R. *et al.* Investigative Urology: Magnetic Resonance Guided, Focal Laser Induced Interstitial Thermal Therapy in a Canine Prostate Model. *The Journal of urology* **184**, 1514–1520

8. Whelan, W. M., Chun, P., Chin, L. C., Sherar, M. D. & Vitkin, I. A. Laser thermal therapy: utility of interstitial fluence monitoring for locating optical sensors. *Physics in Medicine and Biology* **46**, N91–N96 (2001).

9. Vakoc, B. J., Tearney, G. J. & Bouma, B. E. Real-time microscopic visualization of tissue response to laser thermal therapy. *Journal of Biomedical Optics* **12**, 20501 (2007).

10. Dewhirst, M. W., Viglianti, B. L., Lora-Michiels, M., Hanson, M. & Hoopes, P. J. Basic principles of thermal dosimetry and thermal thresholds for tissue damage from hyperthermia. *International journal of hyperthermia* **19**, 267–94 (2003).

11. Whelan, W. M., Davidson, S. R., Chin, L. C. & Vitkin, I. A. A Novel Strategy For Monitoring Laser Thermal Therapy Based on Changes in Optothermal Properties of Heated Tissues. *International Journal of Thermophysics* **26**, 233–241 (2005).

12. Carpentier, A. *et al.* MR-guided laser-induced thermal therapy (LITT) for recurrent glioblastomas. *Lasers in surgery and medicine* **44**, 361–8 (2012).

13. Fernando, R., Downs, J., Maples, D. & Ranjan, A. MRI-Guided Monitoring of Thermal Dose and Targeted Drug Delivery for Cancer Therapy. *Pharmaceutical research* **30**, 2709–17 (2013).

14. Wang, S. *et al.* Contrast ultrasound-guided photothermal therapy using gold nanoshelled microcapsules in breast cancer. *European Journal of Radiology* (2013).doi:10.1016/j.ejrad.2013.09.010

15. Papini, E. *et al.* Percutaneous ultrasound-guided laser ablation is effective for treating selected nodal metastases in papillary thyroid cancer. *The Journal of clinical endocrinology and metabolism* **98**, E92–7 (2013).

16. Pramanik, M. & Wang, L. V Thermoacoustic and photoacoustic sensing of temperature. *Journal of biomedical optics* **14**, 054024 (2009).

17. Shah, J. *et al.* Photoacoustic imaging and temperature measurement for photothermal cancer therapy. *Journal of Biomedical Optics* **13**, 34024 (2008).

18. Sonntag, P. D., Hinshaw, J. L., Lubner, M. G., Brace, C. L. & Lee, F. T. Thermal ablation of lung tumors. *Surgical oncology clinics of North America* **20**, 369–87, ix (2011).

19. Vogel, M.W. Suprijanto, A.M. Vossepoel, H. A. Vrooman, A. M. Vossepoel, P. M. T. P. Towards Motion-Robust Magnetic Resonance Thermometry. *MACCAI-Medical Image Computing and Computer-Assisted Intervention 2001* 401–408 (2001).

20. Atri, M., Gertner, M. R., Haider, M. A., Weersink, R. A. & Trachtenberg, J. Contrast-enhanced ultrasonography for real-time monitoring of interstitial laser thermal therapy in the focal treatment of prostate cancer. *Canadian Urological Association Journal* **3**, 125–130 (2009).

21. Larin, K. V, Larina, I. V & Esenaliev, R. O. Monitoring of tissue coagulation during thermotherapy using optoacoustic technique. *Journal of Physics- London* **38**, 2645–2653 (2005).

22. Worthington, A., Trachtenberg, J. & Sherar, M. Ultrasound properties of human prostate tissue during heating. *Ultrasound in Medicine & Biology* **28**, 1311–1318 (2002).

23. Lou, C. & Xing, D. Temperature monitoring utilising thermoacoustic signals during pulsed microwave thermotherapy: a feasibility study. *International journal of hyperthermia* **26**, 338–46 (2010).

24. Chitnis, P. V, Brecht, H.-P., Su, R. & Oraevsky, A. A. Feasibility of optoacoustic visualization of high-intensity focused ultrasound-induced thermal lesions in live tissue. *Journal of biomedical optics* **15**, 021313 (2010).

25. Oraevsky, A. A. *et al.* Laser optoacoustic imaging of the breast: detection of cancer angiogenesis. *Proceedings - Society of Photo-Optical Instrumentation Engineers* **3597**, 352–363 (1999).

26. Esenaliev, R. O., Karabutov, A. A. & Oraevsky, A. A. Sensitivity of laser opto-acoustic imaging in detection of small deeply embedded tumors. *IEEE Journal of Selected Topics in Quantum Electronics* **5**, 981 (1999).

27. Yao, J. & Wang, L. V Photoacoustic tomography: fundamentals, advances and prospects. *Contrast media & molecular imaging* **6**, 332–45

28. Song, K. H. & Wang, L. V Deep reflection-mode photoacoustic imaging of biological tissue. *Journal of Biomedical Optics* **12**, 60503 (2007).

29. Saha, R. K., Karmakar, S., Hysi, E., Roy, M. & Kolios, M. C. Validity of a theoretical model to examine blood oxygenation dependent optoacoustics. *Journal of Biomedical Optics* **17**, 55002 (2012).

30. Lizzi, F. L., Greenebaum, M., Feleppa, E. J., Elbaum, M. & Coleman, D. J. Theoretical framework for spectrum analysis in ultrasonic tissue characterization. *The Journal of the Acoustical Society of America* **73**, 1366–1373 (1983).

31. Frederic, L. L., Ernest, J. F., S, K. A. & Cheri, X. D. Ultrasonic spectrum analysis for tissue evaluation. *Pattern Recognition Letters* **24**, 637–658 (2003).

32. Zalev, J. & Kolios, M. C. Detecting abnormal vasculature from photoacoustic signals using wavelet-packet features. *Proceedings of SPIE* 78992M (2011).

33. Barton, J. K. *et al.* Photothermal coagulation of blood vessels: a comparison of high-speed optical coherence tomography and numerical modelling. *Physics in medicine and biology* **46**, 1665–78 (2001).

34. Lizzi, F. L. *et al.* Ultrasonic spectrum analysis for tissue assays and therapy evaluation. *International Journal of Imaging Systems & Technology* **8**, 3–10 (1997).

35. Cheong, W.-F., Prahl, S. A. & Welch, A. J. A review of the optical properties of biological tissues. *SPIE Milestone series* **102**, 129 (1995).

36. Xu, X.-H. & Li, H. Photoacoustic imaging in biomedicine. *Physics - Beijing* **37**, 111–119 (2008).

37. Liu, T. *et al.* A feasibility study of novel ultrasonic tissue characterization for prostate-cancer diagnosis: 2D spectrum analysis of in vivo data with histology as gold standard. *Medical physics* **36**, 3504–3511 (2009).

38. Xi, L. *et al.* Photoacoustic imaging based on MEMS mirror scanning. *Biomedical Optics Express* **1**, 1278 (2010).

39. Xu, Y., Wang, L. V, Ambartsoumian, G. & Kuchment, P. Reconstructions in limited-view thermoacoustic tomography. *Medical physics* **31**, 724–33 (2004).

40. Strohm, E., Gorelikov, I., Matsuura, N. & Kolios, M. Photoacoustic spectral characterization of perfluorocarbon droplets. *SPIE BiOS* 82232F–82232F–8 (2012).

41. Yarmolenko, P. S. *et al.* Thresholds for thermal damage to normal tissues: an update. *International journal of hyperthermia* **27**, 320–43 (2011).

42. Chang, I. A. Considerations for thermal injury analysis for RF ablation devices. *The Open Biomedical Engineering Journal* **4**, 3–12 (2010).

43. Nandlall, S. D., Arora, M., Schiffter, H. A., Coussios, C.-C. & Ebbini, E. S. On the Applicability of the Thermal Dose Cumulative Equivalent Minutes Metric to the Denaturation of Bovine Serum Albumin in a Polyacrylamide Tissue Phantom. *8th International Symposium on Therapeutic Ultrasound* **1113**, 205–209 (2009).

44. Liang, J., Tang, M.-L. & Chan, P. S. A generalized Shapiro–Wilk statistic for testing high-dimensional normality. *Computational Statistics & Data Analysis* **53**, 3883–3891 (2009).

45. Irina, V. L. & Kirill V Larin and Rinat, O. E. Real-time optoacoustic monitoring of temperature in tissues. *Journal of Physics: D Applied Physics* **38**, 2633 (2005).

46. Larin, K. V, Larina, I. V & Esenaliev, R. O. Monitoring of tissue coagulation during thermotherapy using optoacoustic technique. *Journal of Physics- London* **38**, 2645–2653 (2005).

47. Cui, H. & Yang, X. Real-time monitoring of high-intensity focused ultrasound ablations with photoacoustic technique: an in vitro study. *Medical physics* **38**, 5345–50 (2011).

48. THOMSEN, S. Identification of lethal thermal injury at the time of photothermal treatment. *SPIE Optical Engineering Press* 459–467 (1995).

CHAPTER 5

OPTOACOUSTIC CHARACTERIZATION OF HEPATIC AND RENAL VASCULATURE USING VASCULAR CORROSION CASTS, *IN VIVO* TISSUES AND MATHEMATICALLY SIMULATED MODELS

"How wonderful that we have met with a paradox. Now we have some hope of making progress."

-Niels Bohr (1885-1962)

picture from http://www.goodreads.com/author/show/821936.Niels_Bohr

5.1 Introduction

The diagnosis of cancer is often based on qualitative data obtained through an invasive tissue biopsies procedure [1]. Quantitative data on the tumours' unique vascular network, however, may elucidate a better understanding of its aggressiveness, and facilitate improved treatment planning [2,3]. Ideally, this would be obtained via a non-invasive technique. Many solid tumours are characterized by unique vascular networks (e.g. vessel diameter; density; branching angles) compared with normal, healthy tissues [1]. Most strikingly, tumour capillaries are often more tortuous, leaky, dense and disorganized than normal capillaries making the evaluation of the vascular components of neoplasms a viable approach for detecting them [4,5].

Currently, the most common quantitative analysis of tumour microvasculature used in preclinical models is histological diagnosis [3]. However, the cut surface dictates a view of the tumour which is a randomly selected two-dimensional slice of the mass, making it difficult to be confident that it is representative of a complex three-dimensional structure [6,7]. Intravital microscopy is an emerging technique that has enabled *in vivo* detection of orthotopic tumours (implantated tumours into their originating tissue) [8,9]. This approach allows for submicrometer lateral resolution and three-dimensional reconstructions, however it suffers from its lack of flexibility with respect to the microscope body and lenses [8]. For this technique to be maximally effective, the surface of the tumour should be flat, which is rarely the case [8].

Optoacoustic imaging has the ability to image vascular structures with high contrast and high resolution [10,11]. The majority of the OA systems, presented in recent

literature, describe the ability to image vasculature with high resolution (e.g. less than 0.5 mm) and deep penetration (e.g. greater than 5 mm) using spherical or cylindrical detection geometries [12,13] (see section 1.6). These detection geometries are ideal for accurate OA image reconstruction, and provide high contrast and resolution in real time. However, these geometries are constrained by the need for access to all sides of the target. They are not suitable for imaging superficial structures, such as the skin, or if strongly echogenic structures such as bone or lung are situated along the acoustic propagation path (as is the case for the prostate) [10]. These circumstances call for more versatile planar detection geometry in which detection is performed over a finite plane using a one or two-dimensional ultrasound array [10]. The OA imaging systems that employ this geometry often resemble conventional ultrasound imaging systems. Frequently OA imaging instruments may use existing clinical ultrasound scanners, sufficiently modified, so that the RF (radio frequency) acquisition can be triggered by the excitation laser in order to detect OA waves as well as ultrasound echoes [14–18]. Co-registration of the OA and ultrasound images is then relatively straightforward and absorption-based contrast, from the OA image, can provide structural and functional information about the vasculature, while the ultrasound image provides information on the tissue morphology based on elasto-mechanical properties [10,19].

Real-time optoacoustic imaging has been demonstrated using planar geometry detection to visualize tumours *in vivo* (see section 1.6). However, the resolution associated with these images rarely matches that of spherical/cylindrical detection systems [20]. Three-dimensional, high-resolution OA images can also be acquired using planar detection systems as shown by Laufer et. al. [21] (see section 1.6). However, these

images necessitate axial and lateral mechanical scanning which consequently increases imaging time. This imaging time remains a common limiting factor for three-dimensional planar detection systems limiting applicability for clinical use [22,23].

Thus, planar detection geometry, although ideal for clinical use, lacks the necessary resolution or cannot be performed in real time [10]. In order to overcome these limitations, the mechanical scanning speed must be increased (limited, and often itself introduces artifacts) or the resolution of two-dimensional OA images must be improved.

An indirect means of improving the resolution of OA images may exist in the alternative analyses of the detected signal. In addition to the amplitude, the frequency content of the OA signals may provide sub-resolution information, making two-dimensional, relatively low-resolution OA images more viable for clinical use. Even if vascular structures themselves are not resolved in the reconstructed images (reconstruction often loses a great deal of information, particularly the sub-resolution detail [24]), frequency content of the generated OA signals may be used to identify regions in the tissues with specific vascular characteristics which may indicate the presence of disease [25]. This may provide essential information about the target that replaces the need for very high resolution imaging, which is associated with long acquisition times when using planar detection geometry.

The information content of a transducer's signals is related to the frequency response and the field profile of the transducer [26]. As the number of transducer locations decreases, limiting the system's resolution, the information content from each individual signal remains unchanged. There is significant information with sub-resolution detail

contained in each OA signal [27,28]. For example, it is known that the size and concentration of the optical absorber dictates the frequency content of the OA RF signals [29,30]. Work is ongoing to identify how other target characteristics are manifested in the frequency content of the OA signals as well [25,31].

5.1.1 Hepatic and renal vasculature

Hepatic and renal vascular characteristics (including root vessel diameter, branching angle, relative vessel sizes and density) differ significantly in several strains of adult mice [32–34]. However, these differences are minimal compared with the differences between normal/healthy vasculature and neoplastic vasculature [32]. The ability to discriminate these two tissues would, therefore, imply that discriminating between normal and neoplastic tissue, based on their different vascular characteristics, is conceivable.

Healthy hepatic and renal vascular characteristics in the mouse have been well documented [1,33–35]. Mouse hepatic and renal vessels and capillaries range in diameter from approximately 5 μm to 200 μm. Hepatic vessels of adult female nude mice are on average, approximately 10 μm, while renal vessels are slightly larger at approximately 15 μm on average [1]. Average vessel densities are approximately 6 and 3 % length/area for hepatic and renal vascular, respectively [1]. Therefore, averaged over the entire organs (in several strains of adult mice) hepatic vessels are smaller and more dense than renal vessels (see Results, Figure 5.7) [33–36].

5.1.2 Vascular corrosion casts

Vascular corrosion casting is a standard method of visualizing the three-dimensional architecture of a vascular network, and involves injecting a casting material into the circulatory system of the animal, which quickly polymerizes into a hardened plastic cast [37]. Tissues are then corroded away, leaving behind a detailed cast of the circulatory system.

The casting material used can significantly affect the quality of the resulting cast, and should have low viscosity, quick and even polymerization, minimal shrinkage during drying, and resistance to corrosion during cleaning, dissection and drying. Latex and silicone rubber have been used due to their low viscosity and low resistance to corrosion but result in inconsistent replication of luminal surface microstructures [37]. Polyurethane based resin (PU4ii), which has low viscosity, quick polymerization, minimal shrinkage and is highly elastic post-casting, is an emerging compound for vascular casting [32]. However, the most common material for constructing casts, and that which was chosen for this study, is methyl methacrylate (Mercox®) which has a low viscosity, quick polymerization, minimal shrinkage and results have been well documented [32]. Mercox® has the ability to infiltrate capillaries as small as 5 μm in diameter [38]. The limiting resolution of vascular casts is therefore often in the CT images which are used to observe the capillaries. A relatively high-resolution CT system (e.g. micro-CT) would have a resolution of approximately 15 -30 μm^1. When hardened, resins similar to Mercox® have a Grüneisen parameter of approximately 5 compared with soft tissue which has a Grüneisen parameter of typically less than 1 at between 20-40 °C [39,40].

5.1.3 Computer simulation of vasculature

There are several methods used to generate models of vasculature in tissue. The goal of all of these approaches is to mimic the tissue with parameters based on actual physical characteristics. Vascular networks of an organ with blood flow considerations were modeled by Kretowski et al. (2003) who simulated the vascular geometry by simulating the process of vessel formation [41,42]. Kurz and Godde (2001) used cellular automaton to simulate angiogenisis and vascular remodeling [43]. Turing reported using activator inhibitor models to record the transfer of chemical signals [44]. Wang et al. (2007) described the generation of realistic vascular branching patters by using Markov probability models based on actual vasculature [45]. Zamir (2001) and Kharchakdjian (2001) also modeled renal vascular tissue, using fractral trees consisting of many branching vessel segments [46,47].

A fractal tree is a mathematical structure that is formed by iteratively applying a branching pattern to the result from the previous iteration. The pattern is specified as a relationship between the parent segment, the left child segment and the right child segment. Here, the terms "left" and "right" are mathematical conventions and do not necessarily correspond to the physical directions for which they are named.

A single iteration of the fractal tree pattern is shown in Figure 5.1. Three segments are connected in a Y-shaped configuration. Each segment is a finite-length cylinder with length L and diameter D. The child segments meet the parent segment at a junction located at the end of the parent segment. The angle at which a child branch diverges from the parent segment is called θ. The rotation of a child branch with respect

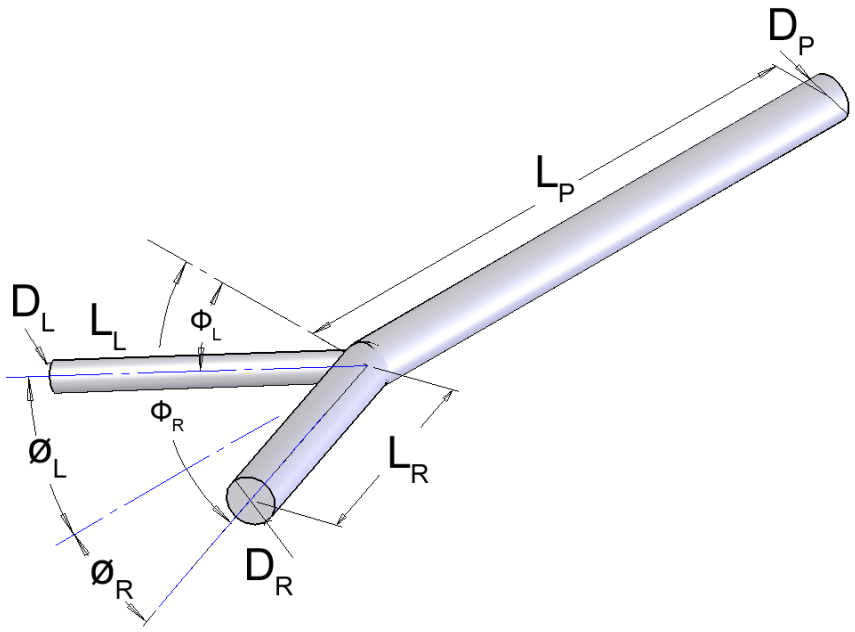

Figure 5.1: Fractal tree pattern used to model vascular morphology adapted from Zavel [48]. The posterior end of the parent segment splits into two child segments. Each child segment becomes a parent segment in the succeeding iteration [48].

to a reference plane through the parent is given by the angle ø [26]. The diameter asymmetry (also called the bifurcation index) is defined as;

$$\beta_i = D_R/D_L \qquad 0 \leq \beta_i \leq 1$$

where D_R and D_L are the diameters of the right and left child branches respectively. A uniform probability distribution is used to induce randomness into the branching structure. This fractal pattern is repeated upon multiple iterations.

Simulation of vascular networks using fractal trees is a convenient method for generating datasets of tissue. The mathematical structure of the fractal tree model allows specific morphological parameters to be varied in a deliberate way which facilitates controlled testing [26]. Quantitative validation of the use of fractal trees for simulating human liver has found that there is up to 85% agreement between the simulation and casts of human hepatic vasculature [49]. Fractal tree simulations may also be used to assess morphological and functional properties of biological tissues based on their fractal nature [50]. Clinically, fractal tree simulations have also been used for surgery planning of split-liver transplants and tumor resection with much success [51].

Based on structural morphology, we postulated that it would be possible to differentiate between different sub-resolution vascular morphologies using optoacoustic techniques. In this study, we aimed to investigate: the relationships between the size and concentration of OA targets and the frequency spectrum of the detected OA signals, and the ability of OA imaging to distinguish two sub-resolution vascular structures (hepatic and renal vasculature), via frequency analysis of the OA RF signals.

5.2 Materials and Methods

All procedures performed in this study were approved by the Animal Care Committee of the University of Prince Edward Island, and were written in accordance with the guidelines of the Canadian Council for Animal Care. The following methods were used to achieve the above objectives.

5.2.1 Polystyrene microsphere phantoms

Tissue-mimicking phantoms were constructed using gelatin powder derived from porcine skin (Sigma-Aldrich Co., St. Louis, MO) and black polystyrene microspheres (Polyscience Inc., Warrington, PA) as spherical absorbers with diameters of 10 μm, 50 μm and 100 μm. These diameters were chosen to represent the approximate published diameter range (5 μm for smaller capillaries, to 100-200 μm for larger vessels [52]) of vessels and capillaries that are found in murine hepatic and renal vasculature [53,54] . Phantom preparation involved mixing the microspheres with degassed water which was then heated to approximately 80 ^{o}C. The gelatin powder was added and mixed until it had completely dissolved (approximately 10 minutes). This solution was then poured into phantom molds (measuring 4 cm by 4 cm by 2 cm) which were then cooled to 4^{o}C for at least 2.5 hours. For each phantom, 4 g of gelatin was mixed with 40 mL of degassed water. For each microsphere size, three different phantoms were constructed with the following concentrations of microspheres: 0.1, 0.2 and 0.3% (v/v), by mixing the appropriate amount of microspheres with degassed water prior to heating.

Optoacoustic signals were obtained at 50 unique locations, within 3 different regions of interest (ROIs; 2 mm x 2 mm) on each phantom (Figure 5.2) using the SENO optoacoustic imaging system. Twenty-seven ROIs from nine phantoms were imaged in

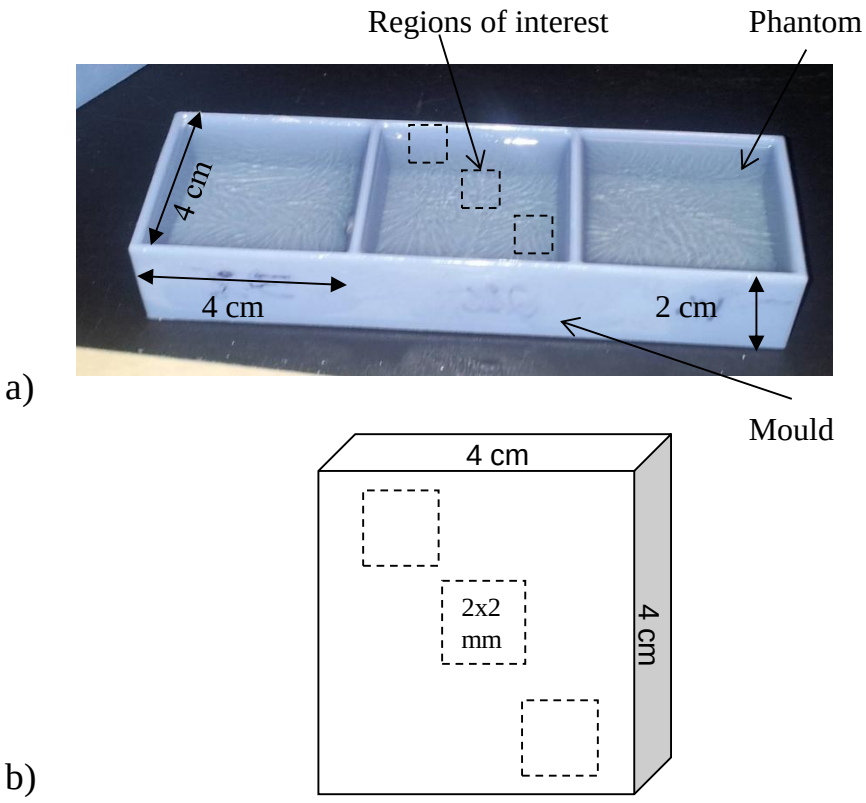

Figure 5.2: a) Photograph of three gelatin phantoms with 50 μm spheres at 0.3, 0.2 and 0.1% concentrations in molds. Three regions of interest (2 mm x 2 mm) were imaged on each phantom as shown on b) the phantom schematic. Fifty signals were acquired within each region.

total. Sample size was determined by performing a power analysis using results of a similar study [55]. Images were acquired using laser fluence of 2.5 W at 775 nm, and 0.2 mm step size.

Each image was recorded in duplicate to verify that there was no significant intra-sample variation between image acquisitions. Amplitude and frequency analysis was performed on all OA signals acquired.

5.2.2 Vascular corrosion casts

Vascular corrosion casts were created using methyl methacrylate (Mercox®) [32] . Casts were prepared as described by Giuvărăşteanu (2007) [37]. Prior to casting, four C57Bl/6 mice were transcardially perfused with 20 ml of saline. The catalyst (2 ml; Benzoyl Peroxide (40%)) was added to 20 ml of Mercox® and stirred until completely dissolved. This 22 ml solution was injected into the left ventricle of the mouse using a 20 ml syringe at a constant rate (10 ml/min) until the liquid exiting the pericardium turned red. For 30 minutes post injection the animal remained undisturbed to allow the casting medium to harden. The tissue surrounding the casting medium was removed by immersing the animal into sodium hydroxide (40%) for 3 days. The sodium hydroxide solution was changed once per day. The casts were washed in distilled water to remove any white saponified materials and air dried in a fume hood for 24 hours.

The casts were embedded into gelatin derived from porcine skin (Sigma-Aldrich Co., St. Louis, MO) prior to OA imaging. Optoacoustic signals were acquired in a 2 by 2 mm^2 ROI centered on each of the three cast organs (liver and two kidneys). Signals were acquired every 0.2 mm within the ROI for a total of 100 signals. Images were acquired using laser fluence of 2.5 W at 775 nm, and 0.2 mm step size (identical to those

used for imaging microsphere phantoms).

5.2.3 Computed tomography of vascular corrosion casts

Computed tomography (CT) images of four vascular casts (each containing one liver and two kidneys) were obtained using a micro-CT imaging system (Siemens Inveon Micro-CT). The system has a 12-cm bore for small animal imaging and a 10 x 10 cm field of view and is equipped with a variable focal spot X-ray source. The CT protocol used in this study was designed to represent a scan that might be typical for whole-body mouse imaging. CT set up included 210 degrees of rotation, acquiring 210 projections (i.e. 1 projection acquired per degree of rotation). The x-ray tube had a voltage of 80 kV and a current of 500 μA. Exposure time was 5100 ms/projection, with an effective pixel size of 13.32 μm and a field of view of 40.9 mm (transaxial) by 27.27 mm (axial). Reconstructions were done by slice rather than by volume using Shepp-Logan reconstruction filter and bilinear interpolation [56].

Vessel diameters and relative densities of the blood vessels within the hepatic and renal vascular casts were measured manually in the reconstructed images using ImageJ® software [37].

5.2.4 Computer simulation of vascular trees and associated theoretical OA signals

Murine hepatic and renal vasculature were simulated using a Matlab R2009b (The Math Works, Inc, Natick, MA) based script which involved simulating blood vessel networks with fractal trees [26]. The fractal trees were generated using published values of murine hepatic and renal characteristics, and values measured in the micro-CT images. For the kidneys these values were: branching angle 25° [48], diameters 10-100

μm [53](not including parent vessel diameter), and density 3.5 %length/area [1]. For the liver these values were: branching angle 25° [48], diameters 5-100 μm [1,53] (not including parent vessel diameter) and density 5.5 % length/area [1], Values measured in the micro-CT images of the casts were parent diameters of 250 μm and 300 μm for kidney and liver respectively, and density of 3 and 5 % length/area for kidney and liver respectively. Simple spherical source geometry was used to model OA sources, and simulated theoretical OA signals generated by each fractal tree. The theoretical transducer used in this script had a 1 MHz central frequency with a -6 dB bandwidth of 60%. Validation of the simulator has been performed by Zalev et al. (2010) against a derived exact equation for finite-length cylindrical OA sources and through finite element method (FEM) models [26].

5.2.5 In vivo optoacoustic imaging

All procedures performed in the *in vivo* portion of this study were approved by the Animal Care Committee of the University of Prince Edward Island, and were conducted in accordance with the guidelines of the Canadian Council for Animal Care. Nine adult C57Bl /6 male mice were used in this study. Prior to imaging, each animal was placed in an anesthetic induction chamber and anesthetized with 4% isoflurane in 100% oxygen. Once anesthetized, the hair on the lower abdomen of the animal was removed using a chemical hair remover (Nair ®, Church & Dwight Corporation Inc., ON, Canada). Animals were maintained under general anesthesia, secured to a vertical holder, and lowered up to the neck level into a water-bath which held the laser fibers and the transducer. The imaging system is described in detail in Chapter 2, Materials and Methods. Images were acquired using laser fluence of 2.5 W at 775 nm, and 0.2

mm step size. ROI's of approximately 5 mm x 5 mm were imaged. Analysis was performed on 2 mm x 2 mm ROI's centered on the target organs (liver and kidneys).

Immediately following the image acquisition, animals were euthanized via intracardiac injection of sodium pentobarbital (Euthanyl, Supplier, Location; 65 mg/kg). The animals were then flash frozen in liquid nitrogen (approximately -190 °C) in an upright position on the holder to reduce organ migration. The abdomen was dissected, and 100 µm lateral cryosections were acquired using a cryostat for gross anatomical comparison with the OA images.

5.2.6 Optoacoustic data analysis

The analysis of each data set was performed using an in-house built script written using Matlab R2009b (The Math Works, Inc, Natick, MA). The Hilbert transform was applied to the RF data [57,58]. The signal strength is presented in arbitrary units and all data were collected with the same constant gain settings.

In order to account for optical attenuation by tissues which reduces the light available at depth for OA wave generation, we have employed a depth-dependent signal correction to each A-line. This is somewhat analogous to the use of time gain controls (TGC) in ultrasound imaging to account for acoustic attenuation, However, optical attenuation is significantly greater than the acoustic attenuation below 10 MHz in tissues [58]. For a non-collimated laser beam incident on tissue, the light intensity, decays exponentially according to [1],

$$I(z) = I_o e^{-\mu eff * z} \qquad [1]$$

where μ_{eff} is the effective attenuation coefficient and z is the depth. An effective optical attenuation coefficient of 1.9 cm^{-1} was used (average of mouse skin, fat and muscle attenuation coefficient) [59]. The final form of the correction factor was

$$OA_{Corr}(z) = OA_{HT}(z)e^{\mu eff * z} \quad [2]$$

A MATLAB® (The MathWorks Inc.) based script was developed and used to apply the attenuation estimate to the signals. Such a correction is important given the variation in liver and kidney depths in mice [37].

The signal amplitude was calculated by integrating each signal envelope (obtained by taking the Hilbert transform). Average signal amplitude values were calculated for liver and kidney within the ROI on each organ [60].

5.2.7 Optoacoustic frequency spectrum analysis

A spectrum analysis technique previously described for OA RF data was used for this analysis (Chapter 2, Material and Methods).

The FFT was applied to the RF data to calculate the RF echo spectrum. The mean of the squared spectral magnitudes is the averaged power spectrum (APS). The APS was converted into the decibel (dB) scale. The transducer's power spectrum was subtracted from the converted APS to remove any system-specific artifacts caused by transducer and imaging device.

A sliding Hamming window was employed in order to localize the signal from the sample as well as minimize spectral leakage [61]. The Hamming window had a width of 1 mm and moved in 0.5 mm steps along the axial direction.

A linear fit was applied to the calibrated power spectrum between 1 and 6 MHz. This region was chosen based on the approximate linearity of the dataset and the high signal to noise (SNR of >3 dB) within these frequencies. The signal to noise ratio decreased to close to 1 when the frequencies were above 6 MHz. At the extremely low frequencies (below 1 MHz), a very strong spectrum amplitude is observed. This, however, is not from the illumination of the targets (microsphere or casts), but instead from the residual background signal caused by the illumination on the gel [25]. The midband fit, intercept and slope of the linear fit were calculated and defined as the spectral parameters.

Using the slope and the midband fit together, size and concentration of OA targets can be inferred. If the slope of target 'A' is higher than the slope of target 'B' then it was deduced that target 'A' is smaller in size than target 'B'. Therefore, the midband fit of target 'A' was lower than that of target 'B' at similar concentrations. If the midband fit of 'A' was less than that of 'B' then the concentration of 'A' was considered less than or equal to that of 'B'. If the midband fit of 'A' was greater than that of 'B' then the concentration of 'A' was found to be greater than that of 'B'.

A two-way ANOVA was used to compare the signal amplitudes and spectral parameters of the microsphere phantoms. A paired t-test for different sample sizes was used to compare the signal amplitudes and spectral parameters between hepatic and renal vascular casts and tissue *in vivo*. A p-value of 0.05 or less was used to establish statistically significant differences.

5.3 Results

5.3.1 Polystyrene microsphere phantoms

Representative OA signals from 10, 50 and 100 μm microsphere phantoms all with a 0.3% (v/v) concentration are presented in Figure 5.3. The integrated signal amplitude for all phantoms are presented in Figure 5.4 and summarized in Table 5.1.

Figure 5.5 presents representative power spectrum (APS) of the 50 μm, 0.2% microsphere phantom, the transducer's power spectrum and the calibrated spectrum. The portion of the calibrated APS curve between 1 and 6 MHz was fitted using a linear equation, and the slope, intercept and midband fit of the linear fit were recorded. These variables are defined as the spectral parameters.

The spectral parameters (slope, midband fit and intercept) for the phantoms are presented in Figure 5.6 and summarized in Table 5.1. The OA signal amplitude increased with increasing concentration (of the same size microsphere) and increasing size of microspheres. The amplitude was approximately 32% higher for 100 μm spheres compared with 10 μm spheres. Significant differences ($p<0.05$) in OA amplitude were found between each size of sphere at every concentration, and between each concentration at every size. Interaction between the size and concentration of the spheres was not significant ($p = 0.1841$). There was no significant difference between the amplitude values at different concentrations (when the values of all three sizes were included). The spectral slope decreased significantly with increasing microsphere size

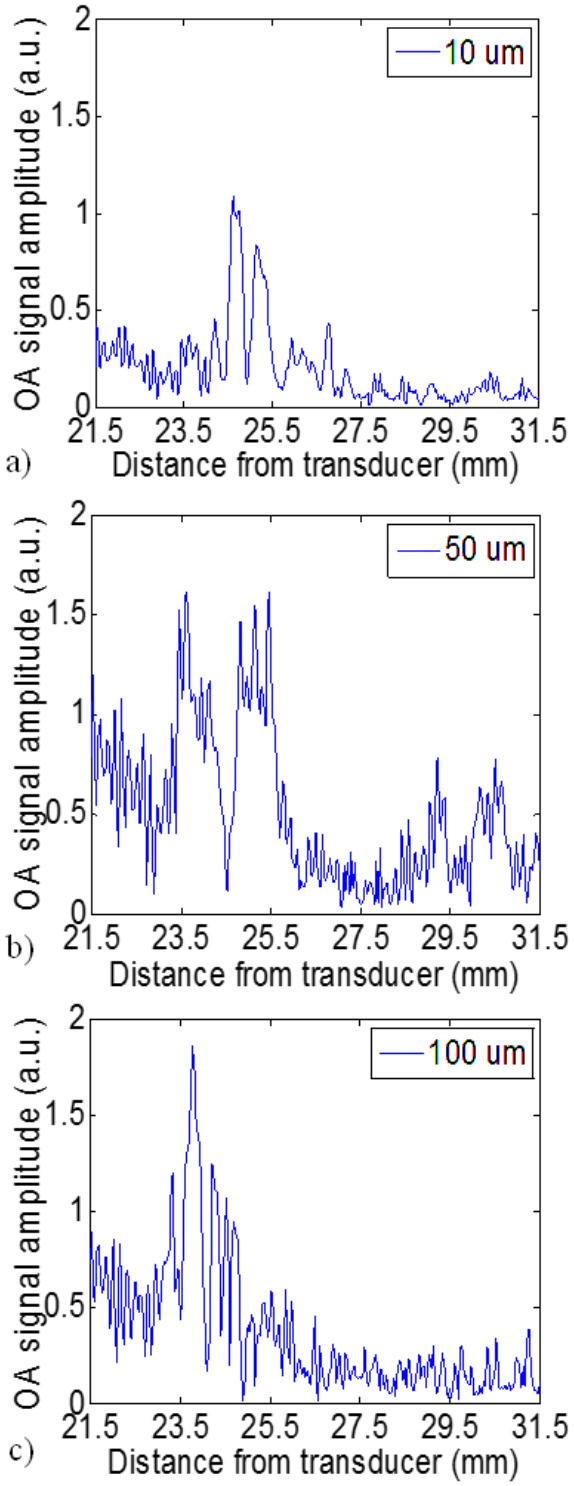

Figure 5.3: Representative optoacoustic signals (Hilbert transformed) for a) 10, b) 50 and c) 100 μm microsphere phantoms of 0.3% (v/v) concentration.

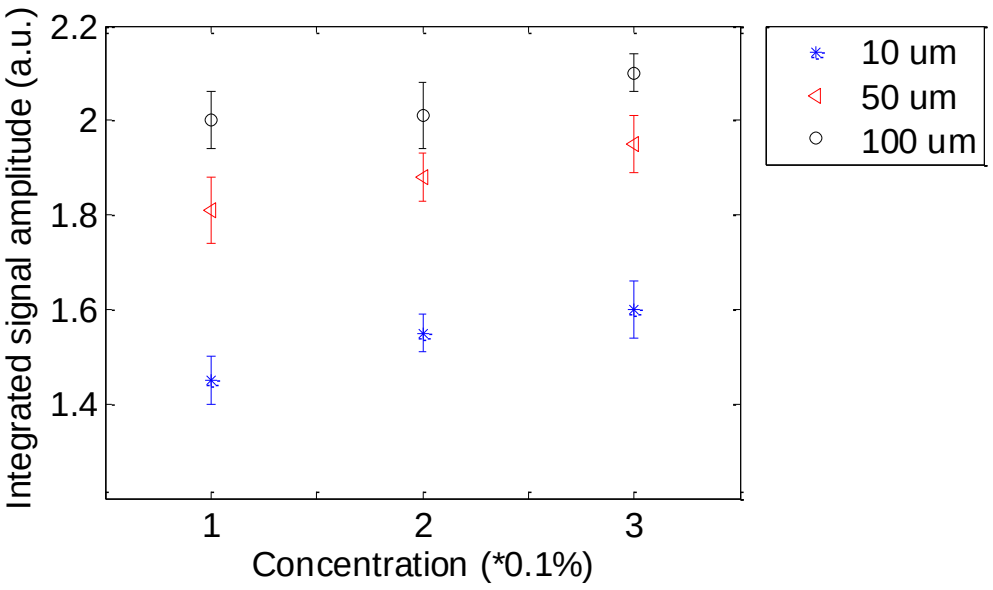

Figure 5.4: Integrated signal amplitude (area under the curve) in arbitrary units for each size and concentration of polystyrene microsphere (N=3). Error bars represent one standard deviation.

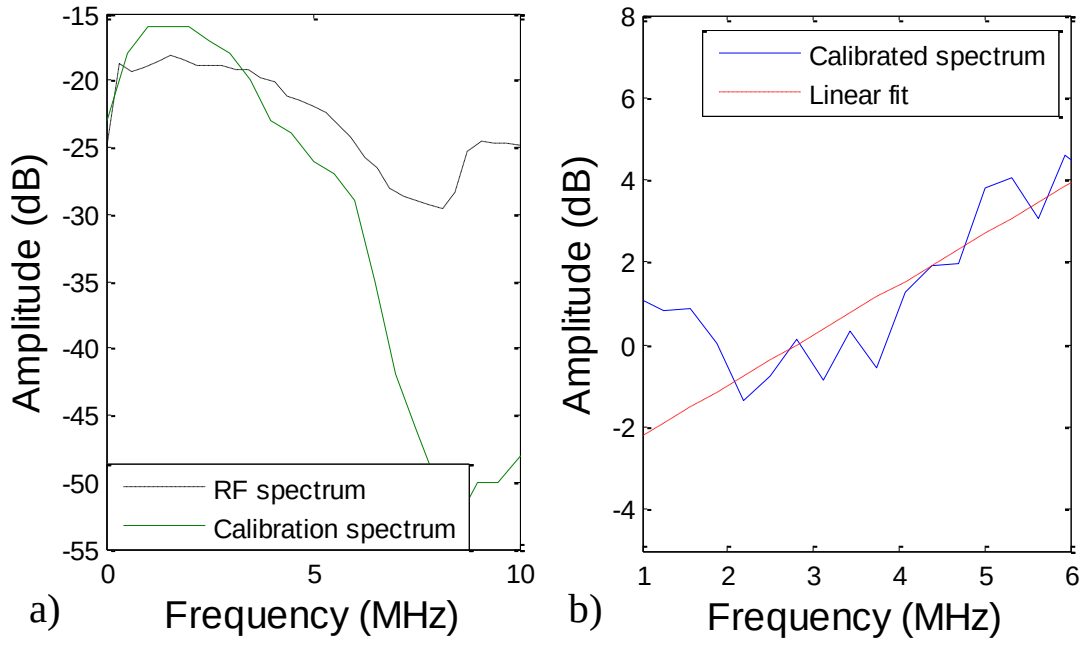

Figure 5.5: Representative power spectrums of; a) uncalibrated radio frequency spectrum and calibration spectrum of the 5 MHz transducer, b) The calibrated power spectrum and linear fit applied between 1 and 6 MHz.

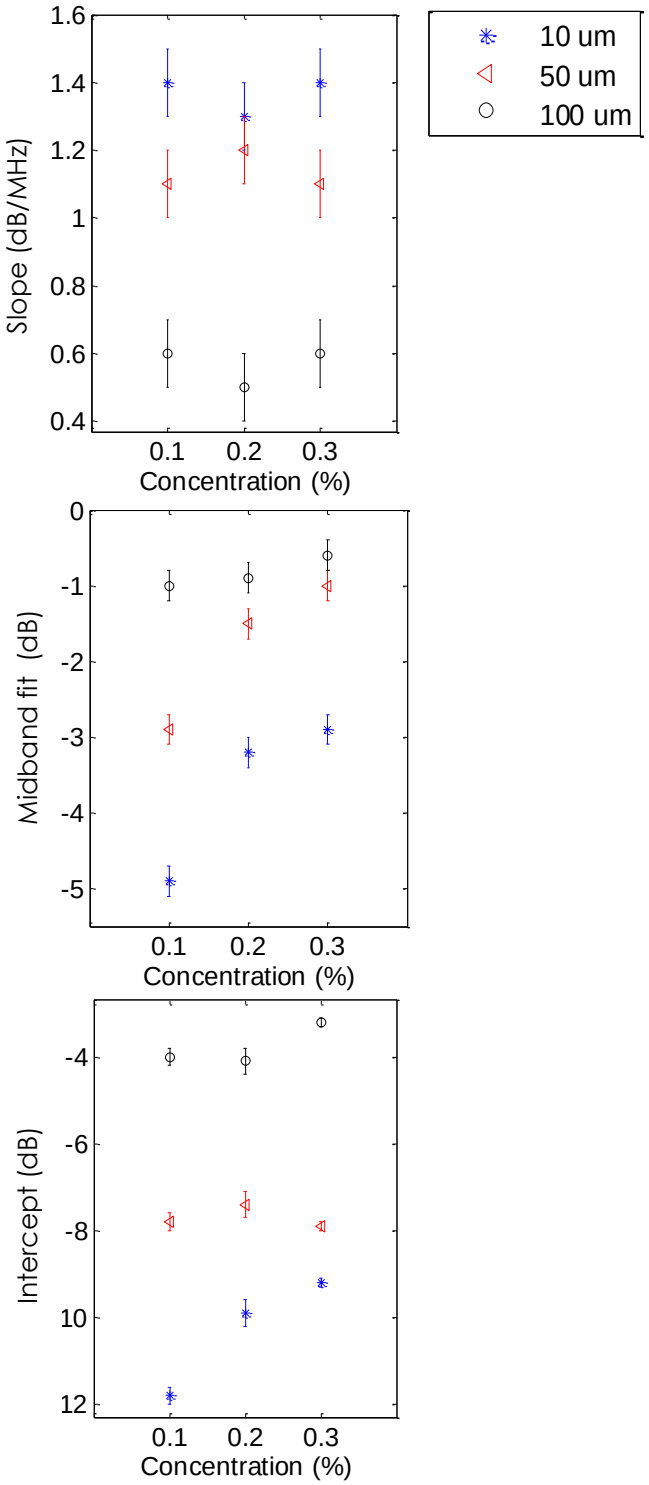

Figure 5.6: Spectral parameters (slope, midband fit and intercept) of polystyrene phantoms with varying sphere concentration and size. Error bars represent one standard deviation (N=3).

Table 5.1: Mean (± standard deviation) integrated optoacoustic signal amplitude and spectral parameterss (slope, midband fit and intercepts) for 10, 50 and 100 μm polystyrene microspheres at concentrations of 0.1, 0.2 and 0.3%. N=3.

Phantom / Parameter	10 μm			50 μm			100 μm		
	0.1%	0.2%	0.3%	0.1%	0.2%	0.3%	0.1%	0.2%	0.3%
Signal amplitude (a.u)	1.5 ±0.1	1.55 ±0.05	1.6 ±0.1	1.8 ±0.1	1.8 ±0.1	1.9 ±0.1	2.0 ±0.1	2.0 ±0.1	2.11 ±0.05
Slope (dB/MHz)	1.4 ±0.1	1.3 ±0.1	1.4 ±0.1	1.1 ±0.1	1.2 ±0.1	1.1 ±0.1	0.6 ±0.1	0.5 ±0.1	0.6 ±0.1
Midband fit (dB)	-4.9 ±0.2	-3.2 ±0.2	-2.9 ±0.2	-2.9 ±0.2	-1.5 ±0.2	-1.0 ±0.2	-1.0 ±0.2	-0.9 ±0.2	-0.6 ±0.2
Intercept (dB)	-11.8 ±0.8	-9.9 ±0.2	-9.2 ±0.4	-7.8 ±0.2	-7.4 ±0.2	-7.9 ±0.9	-4.0 ±0.3	-4.1 ±0.1	-3.2 ±0.3

(p-value <0.001) and was unchanged with increasing concentration (p-value 0.6766). The midband fit significantly increased with increasing size of microsphere (p-value <0.001). As with amplitude, there was no significant difference between the midband fit values at different concentrations (when the values of all three sizes were included) (p-value 0.8440), however, the midband fit value did increase with concentration if size was kept constant. The intercept value significantly increased with increasing size of microsphere (p-value 0.0162). There were no significant differences between the intercept values between different concentrations (0.8564).

5.3.2 Vascular corrosion casts

Figure 5.7 shows representative images of murine hepatic and renal vascular casts. Representative OA signals from hepatic and renal vascular casts are shown in Figure 5.8. Integrated OA signal amplitude values of 0.25 ± 0.06 and 0.21 ± 0.07 were found for hepatic and renal vascular casts respectively. No significant differences were found between the average signal amplitude of each casted organ (p=0.1207).

Spectral parameters from hepatic and renal vascular casts are shown in Figure 5.9. There were no significant differences found in any of the spectral parameters between the casts of the left and right kidney (data not shown). Mean and standard deviation values for both casted tissues are presented in Table 5.2. Each of the spectral parameters was significantly higher for liver compared with kidney casts.

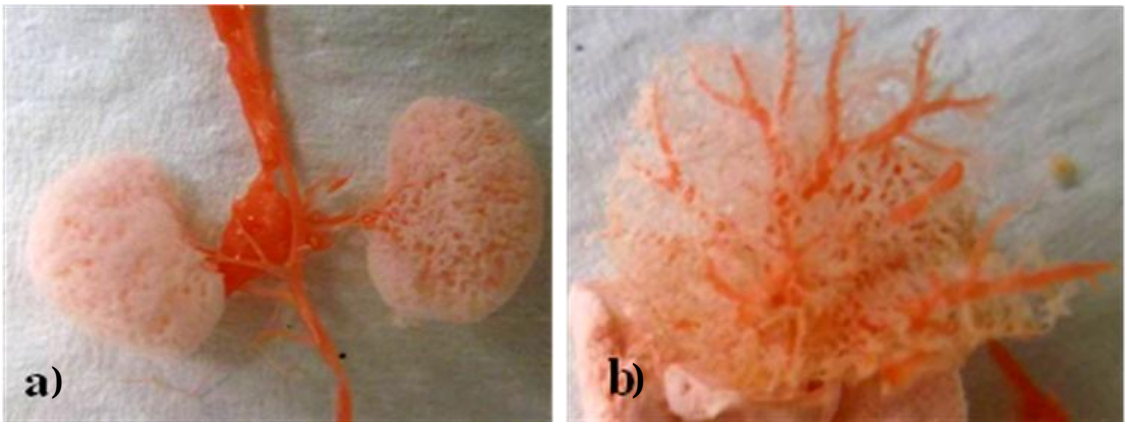

Figure 5.7: Representative images of murine vascular corrosion casts of a) kidneys, b) liver. Mercox® resin was injected into a perfused mouse at a constant rate and allowed to harden. The tissues of the mouse were removed by immersing the body into 40% sodium hydroxide. The kidney and liver were dissected from the cast after removing the overlaying tissue.

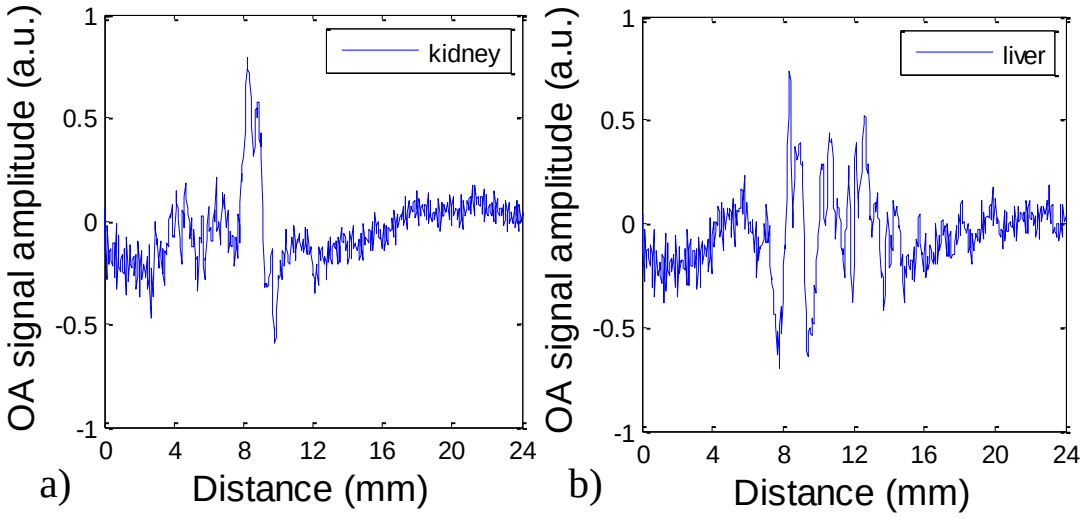

Figure 5.8: Representative optoacoustic signals of a) kidney and b) liver corrosion casts.

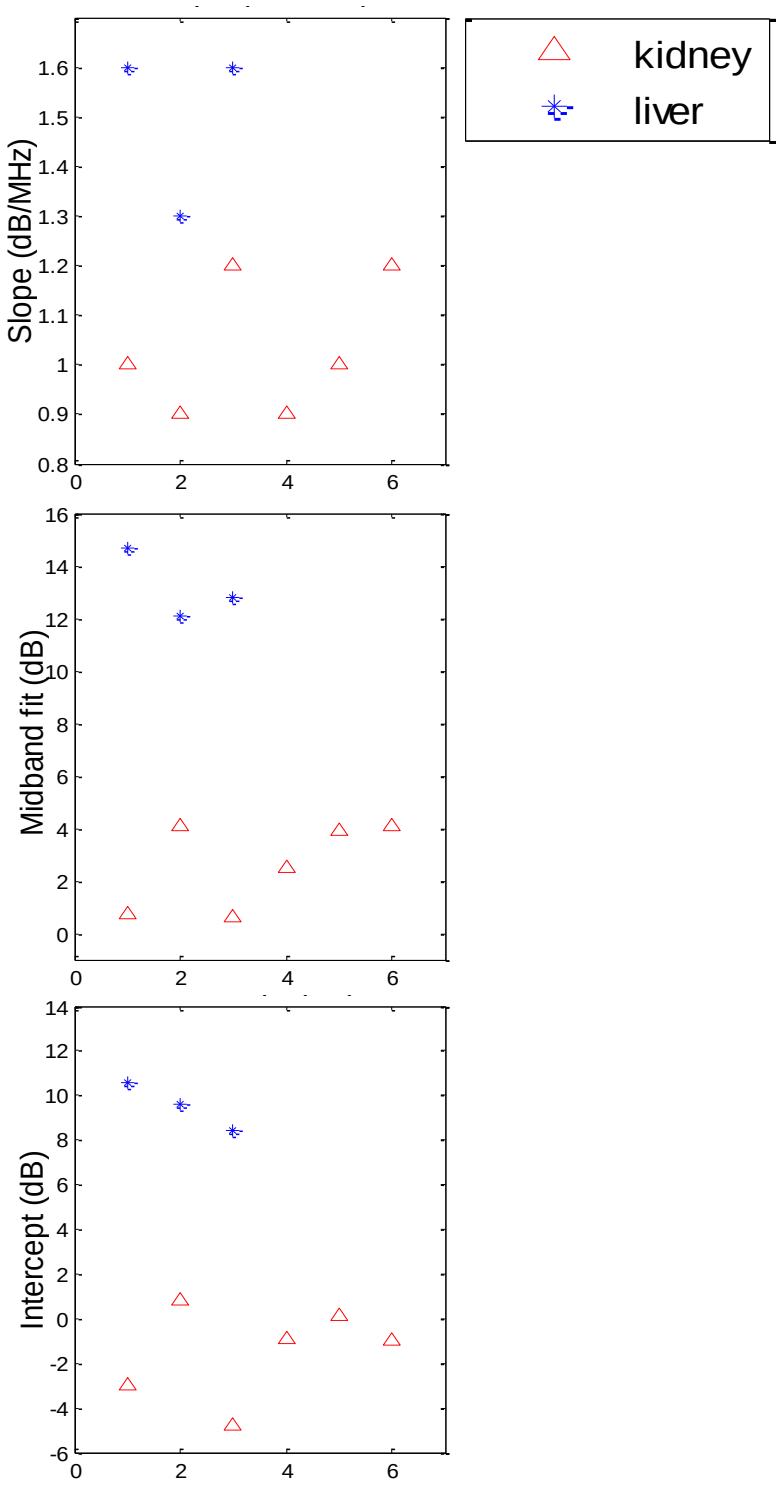

Figure 5.9: Spectral parameters (midband fit, intercept and slope) of optoacoustic signal from liver (N=3) and kidney (N=6) casted tissues.

Table 5.2: Average (± standard deviation) variability of spectral parameters of murine hepatic (N=3) and renal (N=6) vascular casts.

Spectral Parameter	Liver cast	Kidney cast	Paired t-test (p value)
midband fit (dB)	14±1	3±2	<0.001
slope (dB/MHz)	1.5±0.1	1.0±0.2	<0.001
intercept (dB)	9±1	-1±3	<0.001

5.3.3 Computer simulation of vascular trees and associated theoretical OA signals

Representative two-dimensional images of computer simulated hepatic and renal vasculature are presented in Figure 5.10. The associated OA signals of each vascular tree were simulated using the software, and frequency analysis was performed using the same software as was used to analyze the microsphere data. The power spectrum and calibrated power spectrum are presented in Figure 5.11. The frequency parameters of both simulated vasculatures are presented in Table 5.3.

Calibration of the RF spectrum was done using a power spectrum of a transducer with the characteristics of that used to simulate data (i.e. single point element, 1 MHz central frequency).

5.3.4 *In vivo murine model*

An axial cryosection image of the gross anatomy of the liver and kidney region of a mouse is shown in Figure 5.12. Due to natural variations in the positions of the kidneys with respect to the liver and the small imaging window, not all kidneys were within the imaged area in all nine animals and thus, only data from 13 of the 18 kidneys were available for further anlaysis. Integrated signal amplitude values of hepatic and renal tissues are shown in Figure 5.13. Average integrated OA signal amplitude values of 2.4 ± 0.9 and 2.1 ± 0.9 were found for hepatic and renal tissues respectively. No significant differences were found between these two values ($p = 0.4464$).

Spectral parameters from hepatic and renal vasculature are shown in Figure 5.14. There were no significant differences found in any of the spectral parameters between

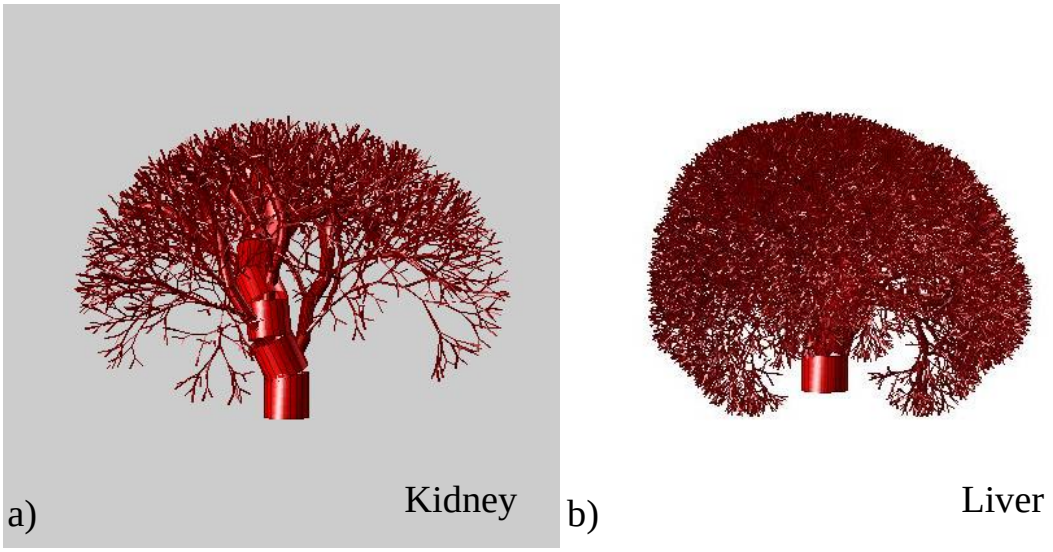

Figure 5.10: Two-dimensional images of vascular trees simulated to represent a) kidney vasculature and b) liver vasculature.

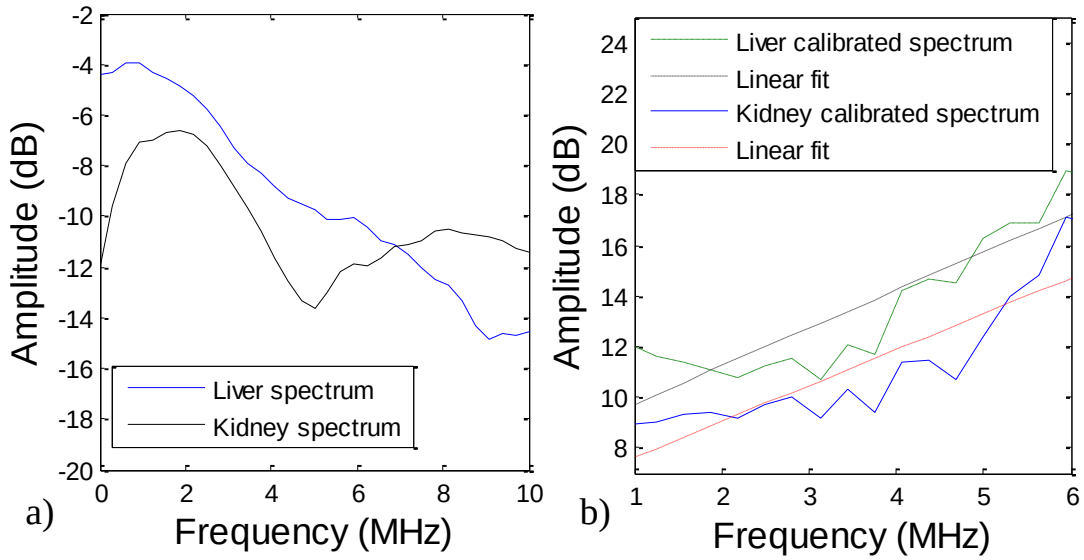

Figure 5.11: Representative power spectrums of simulated hepatic and renal vasculature. a) Uncalibrated RF simulated tissue spectrums, b) Calibrated simulated tissue power spectrums and linear fits applied between 1 and 6 MHz.

Table 5.3: Average ± standard deviations of spectral parameters of simulated murine hepatic and renal vasculature. Uncertainties were defined by varying the vascular characteristics within their spectrum of values given in literature. N=3.

Simulated organ	**Intercept (dB)**	**Slope (dB/MHz)**	**Midband fit (dB)**
Kidney	6.2±0.8	1.42±0.03	12.5±0.7
Liver	8.2±0.6	1.50±0.02	14.9±0.5

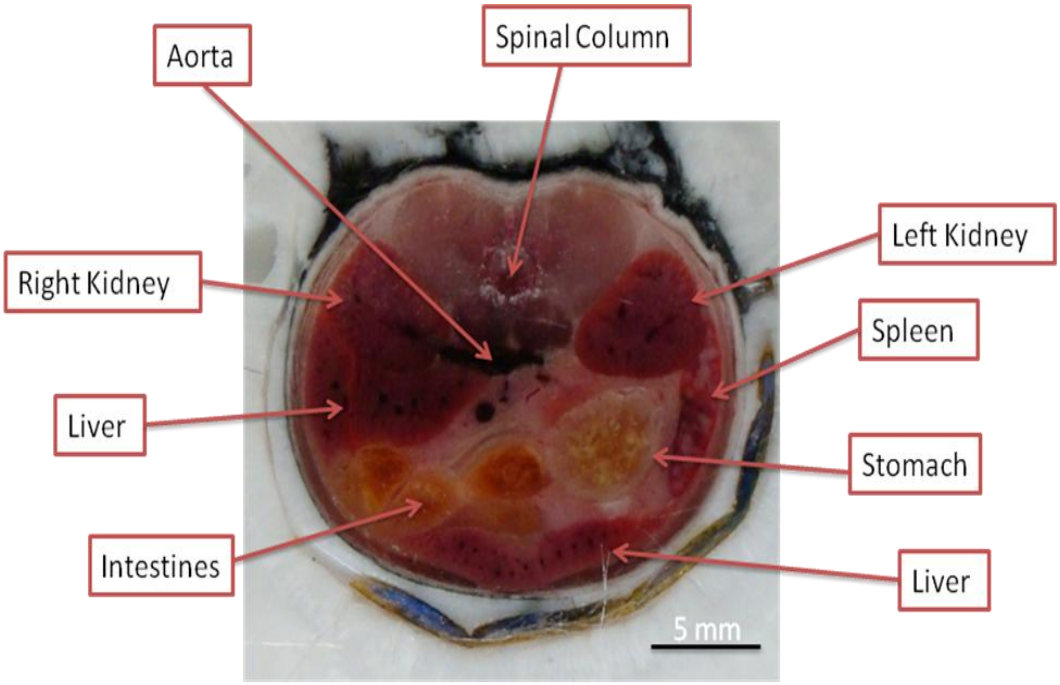

Figure 5.12: Representative Axial cryosection of the liver and kidney region of a C57Bl/6 mouse (photograph by M. Arsenault).

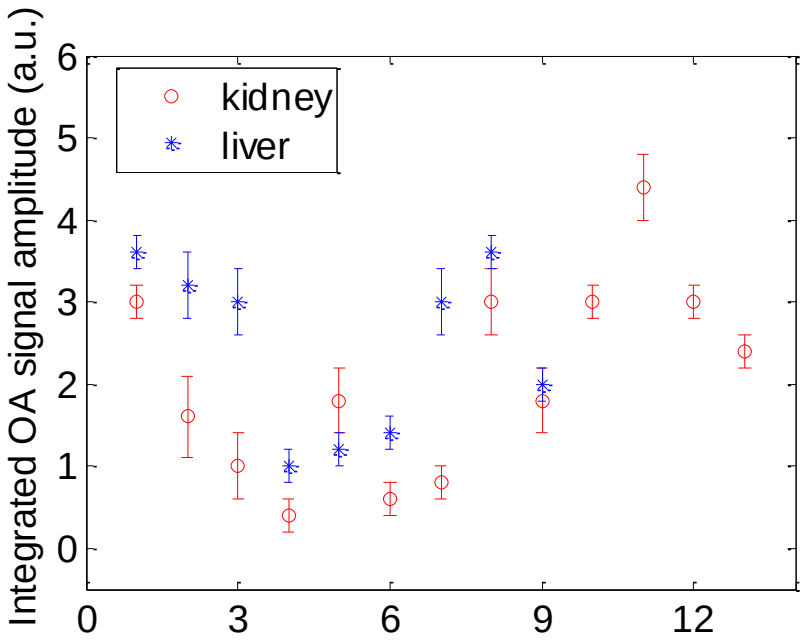

Figure 5.13: Integrated signal amplitude values of optoacoustic signal from liver and kidney tissues of nine C57Bl/6 mice. Error bars represent one standard deviation.

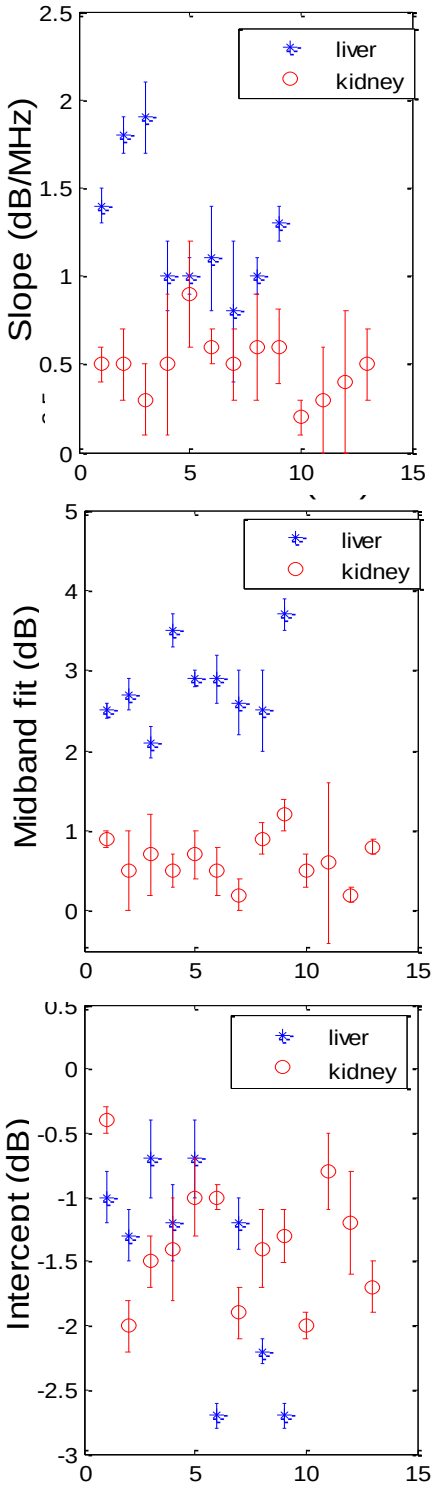

Figure 5.14: Spectral parameters (slope, midband fit, and intercept) of optoacoustic signals from liver (N=9) and kidney (N=13) tissues of nine C57Bl/6 mice. Error bars represent one standard deviation.

the left and right kidneys (data not shown). Mean and standard deviation values for both tissues are presented in Table 5.4.

Midband fit and slope were higher on liver compared with kidney tissue. No significant difference was found between the intercept values of the two tissues.

5.4 Discussion and Conclusions

This study demonstrates the potential for OA imaging to be used to discriminate size and concentration of sub-resolution OA sources (microspheres, and cast, simulated and *in vivo* blood vessels). When reconstructed, the RF signals acquired in this study, did not resolve these individual targets (data not shown). However, when frequency analysis was performed, structural characteristics of these un-resolvable structures were determined. The frequency spectrum of these RF signals was sensitive to the changes in size and concentration of absorbers (microspheres) and thus, was successful in discriminating between tissues with different vascular densities and vessel size distributions (e.g. hepatic and renal vascular). The ability of these two tissues to be discriminated by OA frequency analysis was investigated using vascular corrosion casts, *in vivo* tissues, as well as computer simulated vasculature. To our knowledge, this is the first study which demonstrates the ability to discriminate between healthy sub-resolution vasculature using OA frequency analysis via three different media.

Phantom and simulation studies by Yang et al. (2012) and Xu et al. (2012) experimentally confirmed the feasibility of discriminating target size and concentrations based on the OA frequency spectrum characteristics [25,31]. A similar phantom was

Table 5.4: Average ± standard deviations of spectral parameters on murine liver (N=9) and kidney (N=13) tissues.

Spectral Parameter	Liver	Kidney	t-test (p value)
midband fit (dB)	3.4±0.9	0.8±0.3	<0.001
slope (dB/MHz)	1.4±0.3	0.6±0.2	<0.001
intercept (dB)	-1.7±0.8	-1.5±0.5	0.5434

employed (microspheres embedded in porcine gelatin) by Xu et al. (2004) and found similar trends in the spectral parameters to those presented in this study [25]. The absolute values of the parameters, however, could not be compared as the diameters and concentrations of the microspheres were greater than those used in this study [25]. As the size of the optical absorber (polystyrene microsphere) increased, the corresponding OA signal amplitude also increased (Figure 5.4). This agrees with theoretical solutions to the wave equations which predict that with simple geometries, the amplitude of the pressure wave (i.e. signal) is proportional to the radius of the absorber squared [29]. If the size is kept constant, the amplitude also increases with increasing concentration of absorber.

The slope spectral parameter decreased as the size of the absorber increased (Figure 5.6). A target with a larger diameter generates a signal with a lower frequency compared with a smaller target. Therefore, it is reasonable to expect that absorbers with larger diameters would result in smaller slopes [25,30]. However, upon closer inspection, there does appear to be a discrepancy between the theory presented by Oraevsky et al. (2000) and the results presented herein [62]. The portion of the power spectrum that was used for analysis in this study included only those frequencies between 1 and 6 MHz. According to Oraevsky et al. (2000) this band of frequencies would be generated largely by targets with diameters greater than 100 μm (the targets in this study were 10, 50 and 100 μm in diameter) [62]. Therefore, the larger targets would more significantly affect these frequencies, and should increase the slope rather than decrease it. However, this discrepancy may be explained by the presence of the overlying phantom material and the methodology used. The gelatin phantom with no embedded microspheres produces

relatively strong low frequency (1-2 MHz) signals. Therefore, the presence of the frequency increase centered at 10 MHz, due to the 100 μm targets, results in a more negative slope compared to the presence of the smaller targets which have less impact on the frequencies in the chosen range. The methodology used herein involves the subtraction of the calibration spectrum which peaks at approximately 2 MHz. Due to the sharp negative slope of the calibration spectrum, the subtraction of it results in a calibrated frequency spectrum with a positive slope.

The midband fit increased as the size of the absorber increased and as the concentration increased, similar to the amplitude. Midband fit may be superior to amplitude based on the relative increases of each parameter with change in size and concentration of the target. Signal amplitude varied by 0.61 a.u. with average standard deviation of 0.09 (15% of the variation) while the midband fit varied by 4.3 dB with an average standard deviation of 0.2 (5% of the variation). This suggests that midband fit values are more sensitive to distinguishing between these target characteristics compared with amplitude.

During the process of frequency analysis a FFT is performed which yields a real and imaginary value. Only the real value is used for analysis in this and other published OA and ultrasound frequency spectrum analysis techniques [31,63,64]. The imaginary value of the FFT may be important when estimating the scatterer size, if the data is noise [65]. Some size estimates might turn out to be imaginary if the scatterers are very small (<5 μm) [65]. The phantoms/vasculatures imaged herein, contained targets mostly greater than 5 μm and, therefore, should not be significantly impacted by the imaginary value of the FFT.

OA signals generated by the vascular casts of murine hepatic and renal vascular did not differ significantly in amplitude. Therefore, there was no affect of amplitude on the differences between midband fit and intercept values of the casts. The midband fit, intercept and slope values did differ significantly between the two casted tissues. Based on the results of the microsphere phantoms, the differences found are, thus, more likely to be due to structural differences in the casts The higher slope value associated with the liver casts indicates that it has, on average, smaller vessels than the kidney cast. Assuming the two casted tissues had similar densities (but liver has smaller vessels) the midband fit would have been expected to be less on liver than on kidney. The midband fit, however, was found to be greater on liver which indicates that the liver has a higher vessel density. These results agree with published results of hepatic and renal vasculature as well as with the characteristics which were measured in CT images of these vascular casts [1].

A theoretical 1 MHz central frequency was used to simulate the OA signals. Although a 5 MHz central frequency transducer was used herein, the transducer's power spectrum was similar to a 1 MHz transducer with a -6 dB bandwidth of 60% (this is most likely due to the system electronics which may decrease the frequency focus of the transducer during signal acquisition and processing). The spectral parameters were all greater on liver compared with kidney which agrees with the experimentally acquired data. The relative differences in each parameter were 2.0 for intercept, 0.08 for slope and 2.4 for midband fit. These differences were approximately 80% lower than the experimentally acquired values; however, their associated uncertainties were also 80% lower. The simulated kidney casts produced much higher signal amplitude and,

therefore, midband fit and intercept values, than the experimental kidney data while the simulated liver values were similar to the experimental values. This is likely what caused the decrease in the spectral differences between the two organs. Furthermore, in the case of slope, where the values are not affected by amplitude, the differences were similar among the experimental and simulated data. The simulation script does not take into account wavelength or absorption differences and, therefore, the exact pressure values at the origins of the OA targets are unknown. The absolute values of the generated OA signals are based only on size and relative density of the targets.

Similar trends were observed in the frequency response of the hepatic and renal vascular between experimental and simulated data. Hepatic vasculature (both cast and simulated) generated signals with higher associated midband fit, slope and intercept values compared with renal. A higher slope indicates smaller vessel sizes in the hepatic tissue. Knowing this, if the concentration of vessels in the hepatic tissue were equal or less than that in the renal tissue, the midband fit of the hepatic tissue should be lower (smaller target size results in weaker signal, see Figure 5.6). However, the hepatic tissue has a higher midband fit value, indicating that the concentration of vessels higher. This agrees with published characteristics of these two tissues [1]. Similar differences in slope values were observed in two artificial, melanomas-like tumours with vessel diameters averaging 49 μm and 199 μm [31]. The tumours with smaller vessel diameters had higher slope values than the tumours with larger vessel diameters [31].

No significant difference was found between amplitudes of liver and kidney tissues *in vivo.* Again, as in the cast study, we can thus neglect the affect that amplitude has on the spectral parameters and assume that the differences are due to physical

characteristics of the tissues. The midband fit and slope values of liver were significantly higher than those of kidney *in vivo* (no significant difference was found between intercept values). The loss of significance in the intercept value when obtained *in* vivo may be due to a number of reasons. The intercept value was shown to not be affected by small changes in the density of the absorbing structures (Figure 5.6). The casted hepatic and renal vascular did show significant differences in their respective intercept values, however, this in combination with physiological differences (e.g. blood flow rate, blood pressure, and oxygenation of blood) which would not be present in the cast or simulated data may have caused the intercept values to shift.

Based on theoretical [29,30] and experimental results (microsphere phantoms), this study has shown, using three experimental medium (casts, simulation and *in* vivo), that the frequency response of OA signals can be used to describe unresolvable structures in an OA image. Frequency analysis of OA signals from murine hepatic and renal vascular was used to discriminate between the two tissues based on the differences in their vascular characteristics [1]. These results suggest that this type of analysis of OA signals may be applied to distinguish between normal and neoplastic tissues as the latter tissues often have considerably different vascular characteristics compared with normal tissues [23,32]. Furthermore, knowledge of the vascular characteristics of neoplastic tissues is often highly beneficial in treatment planning [2,3].

This work demonstrates the ability of OA imaging to describe structural characteristics of targets through frequency analysis. Structural differences between murine hepatic and renal vascular were detected using frequency analysis of vascular casts, computer simulation and *in vivo* methods. Frequency results agreed with expected

results based on OA theory and controlled phantom study, in combination with the published characteristics of murine hepatic and renal vascular. Due to the considerable difference in vascular characteristics between normal and cancerous tissues, these results suggest that cancerous tissues may be differentiated from normal tissues and characterized using this method.

References

1. In vivo quantitative microvasculature phenotype imaging of healthy and malignant tissues using a fiber-optic confocal laser microprobe.

2. Feleppa, E. J. *et al.* Recent developments in tissue-type imaging (TTI) for planning and monitoring treatment of prostate cancer. *Ultrasonic imaging* **26**, 163–172 (2004).

3. Gazit, Y. *et al.* Fractal characteristics of tumor vascular architecture during tumor growth and regression. *Microcirculation* **4**, 395–402 (1997).

4. Folkman, J. & Kalluri, R. Cancer without disease. *Nature* **427**, 787 (2004).

5. Laemmel, E. *et al.* Fibered confocal fluorescence microscopy (Cell-viZio) facilitates extended imaging in the field of microcirculation. A comparison with intravital microscopy. *Journal of vascular research* **41**, 400–411 (2004).

6. Baish, J. W. & Jain, R. K. Fractals and cancer. *Cancer research* **60**, 3683–3688 (2000).

7. Spillman J., W. B., Robertson, J. L., Huckle, W. R., Govindan, B. S. & Meissner, K. E. Complexity, fractals, disease time, and cancer. *Physical Review.E, Statistical, Nonlinear, And Soft Matter Physics* **70**, 61911 (2004).

8. Tréhin, R. *et al.* Fluorescent nanoparticle uptake for brain tumor visualization. *Neoplasia* **8**, 302–311 (2006).

9. Alencar, H., Mahmood, U., Kawano, Y., Hirata, T. & Weissleder, R. Novel multiwavelength microscopic scanner for mouse imaging. *Neoplasia (New York, N.Y.)* **7**, 977–983 (2005).

10. Beard, P. Biomedical photoacoustic imaging. *Interface focus* **1**, 602–31 (2011).

11. Mallidi, S., Luke, G. P. & Emelianov, S. Photoacoustic imaging in cancer detection, diagnosis, and treatment guidance. *Trends in biotechnology* **29**, 213–21 (2011).

12. Brecht, H.-P. *et al.* Whole-body three-dimensional optoacoustic tomography system for small animals. *Journal of biomedical optics* **14**, 064007

13. Kruger, R. A., Lam, R. B., Reinecke, D. R., Del Rio, S. P. & Doyle, R. P. Photoacoustic angiography of the breast. *Medical physics* **37**, 6096–100 (2010).

14. Niederhauser, J. J., Jaeger, M., Lemor, R., Weber, P. & Frenz, M. Combined ultrasound and optoacoustic system for real-time high-contrast vascular imaging in vivo. *IEEE Transactions on Medical Imaging* **24**, 436–440 (2005).

15. Kruger, R. A., Kiser, W. L., Reinecke, D. R. & Kruger, G. A. Thermoacoustic computed tomography using a conventional linear transducer array. *Medical physics* **30**, 856–60 (2003).

16. Shah, J. *et al.* Photoacoustic imaging and temperature measurement for photothermal cancer therapy. *Journal of Biomedical Optics* **13**, 34024 (2008).

17. Fronheiser, M. P. *et al.* Real-time optoacoustic monitoring and three-dimensional mapping of a human arm vasculature. *Journal of biomedical optics* **15**, 021305

18. Aguirre, A. *et al.* Coregistered three-dimensional ultrasound and photoacoustic imaging system for ovarian tissue characterization. *Journal of biomedical optics* **14**, 054014

19. Zhang, C., Maslov, K. & Wang, L. V Subwavelength-resolution label-free photoacoustic microscopy of optical absorption in vivo. *Optics Letters* **35**, 3195–3197 (2010).

20. Montilla, L. G., Olafsson, R., Bauer, D. R. & Witte, R. S. Real-time photoacoustic and ultrasound imaging: a simple solution for clinical ultrasound systems with linear arrays. *Physics in medicine and biology* **58**, N1–12 (2013).

21. Laufer, J., Zhang, E., Raivich, G. & Beard, P. Three-dimensional noninvasive imaging of the vasculature in the mouse brain using a high resolution photoacoustic scanner. *Applied Optics* **48**, D299–D306 (2009).

22. Emelianov, S. *et al.* Intravascular ultrasound and photoacoustic imaging. *Conference proceedings : IEEE Engineering in Medicine and Biology Society. Conference* **2008**, 2–5 (2008).

23. Hu, S. & Wang, L. V Photoacoustic imaging and characterization of the microvasculature. *Journal of Biomedical Optics* **15**, 11101 (2010).

24. Noble, J. A. Ultrasound image segmentation and tissue characterization. *Engineering in medicine* **224**, 307–16 (2010).

25. Xu, G. *et al.* Photoacoustic spectrum analysis for microstructure characterization in biological tissue: A feasibility study. *Applied physics letters* **101**, 221102 (2012).

26. Zalev, J. & Kolios, M. C. Detecting abnormal vasculature from photoacoustic signals using wavelet-packet features. *Proceedings of SPIE* 78992M (2011).

27. Candes, E. J., Romberg, J. & Tao, T. Robust uncertainty principles: exact signal reconstruction from highly incomplete frequency information. *IEEE Transactions on Information Theory* **52**, 489–509 (2006).

28. Provost, J. & Lesage, F. The Application of Compressed Sensing for Photo-Acoustic Tomography. *IEEE Transactions on Medical Imaging* **28**, 585–594 (2009).

29. Diebold, G. J., Beveridge, A. C. & Hamilton, T. J. The photoacoustic effect generated by an incompressible sphere. *The Journal of the Acoustical Society of America* **112**, 1780–1786 (2002).

30. Gertsch, A. G., Bush, N. L., Birtill, D. C. C. & Bamber, J. C. Toward characterizing the size of microscopic optical absorbers using optoacoustic emission spectroscopy. *BiOS* 75641M–75641M–10 (2010).

31. Yang, Y., Wang, S., Tao, C., Wang, X. & Liu, X. Photoacoustic tomography of tissue subwavelength microstructure with a narrowband and low frequency system. *Applied Physics Letters* **101**, 034105 (2012).

32. Konerding, M. A., Miodonski, A. J. & Lametschwandtner, A. Microvascular corrosion casting in the study of tumor vascularity: a review. *Scanning microscopy* **9**, 1233–1243 (1995).

33. Vasquez, S. X. *et al.* Optimization of microCT imaging and blood vessel diameter quantitation of preclinical specimen vasculature with radiopaque polymer injection medium. *PloS one* **6**, e19099 (2011).

34. Zagorchev, L. *et al.* Micro computed tomography for vascular exploration. *Journal of angiogenesis research* **2**, 7 (2010).

35. Kline, T. L., Zamir, M. & Ritman, E. L. Relating function to branching geometry: a micro-CT study of the hepatic artery, portal vein, and biliary tree. *Cells, tissues, organs* **194**, 431–42 (2011).

36. Op Den Buijs, J., Bajzer, Z. & Ritman, E. L. Branching morphology of the rat hepatic portal vein tree: a micro-CT study. *Annals of biomedical engineering* **34**, 1420–8 (2006).

37. Giuvărăşteanu, I. Scanning electron microscopy of vascular corrosion casts--standard method for studying microvessels. *Romanian journal of morphology and embryology* **48**, 257–261 (2007).

38. Verli, F. D., Rossi-Schneider, T. R., Schneider, F. L., Yurgel, L. S. & De Souza, M. A. L. Vascular corrosion casting technique steps. *Scanning* **29**, 128–32

39. Yao, D.-K. & Wang, L. V. Measurement of Grüneisen parameter of tissue by photoacoustic spectrometry. *SPIE BiOS* 858138 (2013).doi:10.1117/12.2004117

40. Soroushian, B., Whelan, W. M. & Kolios, M. C. Dynamics of thermoelastic expansion for native and coagulated ex vivo bovine liver tissues. *Proceedings of SPIE* **7899**, 75641N–75641N–4 (2010).

41. Kretowski, M., Rolland, Y., Bézy-Wendling, J. & Coatrieux, J.-L. Physiologically based modeling of 3-D vascular networks and CT scan angiography. *IEEE transactions on medical imaging* **22**, 248–57 (2003).

42. Herrero, M. Á., Kohn, Á. & Perez-pomares, J. M. Modelling vascular morphogenesis: Current views on blood vessels development. *Mathematical Models and Methods in Applied Sciences* **19**, 1483–1537 (2009).

43. Gödde, R. & Kurz, H. Structural and biophysical simulation of angiogenesis and vascular remodeling. *Developmental dynamics : an official publication of the American Association of Anatomists* **220**, 387–401 (2001).

44. Turing, A. M. The Chemical Basis of Morphogenesis. *Philosophical Transactions of the Royal Society B: Biological Sciences* **237**, 37–72 (1952).

45. Wang, L., Bhalerao, A. & Wilson, R. Analysis of retinal vasculature using a multiresolution Hermite model. *IEEE transactions on medical imaging* **26**, 137–52 (2007).

46. Zamir, M. Arterial branching within the confines of fractal L-system formalism. *The Journal of general physiology* **118**, 267–76 (2001).

47. Kharchakdjian, R. Modelling the structure of the tumour vasculature and its effect on Doppler ultrasound signals. 100–150 (2001).

48. Zalev, J. *Detection and monitoring for cancer and abnormal vasculature by photoacoustic signal characterization of structural morphology*. *Theses and dissertations* (2010).

49. Dirk Selle, W. S. B. P. H. P. Mathematical Methods in Medical Imaging: Analysis of Vascular Structures for Liver Surgery Planning.

50. Kamiya, A. & Takahashi, T. Quantitative assessments of morphological and functional properties of biological trees based on their fractal nature. *Journal of applied physiology (Bethesda, Md. : 1985)* **102**, 2315–23 (2007).

51. Manfred Georg, T. P. H. K. H. M. G. T. P. H. K. H. Global Constructive Optimization of Vascular Systems.

52. RUAN, X., OLIVERIO, M. I., COFFMAN, T. M. & ARENDSHORST, W. J. Renal Vascular Reactivity in Mice: AngII-Induced Vasoconstriction inAT1A Receptor Null Mice. *J. Am. Soc. Nephrol.* **10**, 2620–2630 (1999).

53. Yamauchi, K. *et al.* Real-time in vivo dual-color imaging of intracapillary cancer cell and nucleus deformation and migration. *Cancer research* **65**, 4246–52 (2005).

54. VanTeeffelen, J. W. G. E., Constantinescu, A. A., Brands, J., Spaan, J. A. E. & Vink, H. Bradykinin- and sodium nitroprusside-induced increases in capillary tube haematocrit in mouse cremaster muscle are associated with impaired glycocalyx barrier properties. *The Journal of physiology* **586**, 3207–18 (2008).

55. Hysi, E. *Photoacoustic Detection of Red Blood Cell Aggregation*. *Theses and dissertations* (2012).

56. Yu, H., Zhao, S. & Wang, G. A differentiable Shepp-Logan phantom and its applications in exact cone-beam CT. *Physics in medicine and biology* **50**, 5583–95 (2005).

57. Liu, T. *et al.* A feasibility study of novel ultrasonic tissue characterization for prostate-cancer diagnosis: 2D spectrum analysis of in vivo data with histology as gold standard. *Medical physics* **36**, 3504–3511 (2009).

58. Xu, X.-H. & Li, H. Photoacoustic imaging in biomedicine. *Physics - Beijing* **37**, 111–119 (2008).

59. Cheong, W.-F., Prahl, S. A. & Welch, A. J. A review of the optical properties of biological tissues. *SPIE Milestone series* **102**, 129 (1995).

60. de, la Z. *et al.* Ultrahigh sensitivity carbon nanotube agents for photoacoustic molecular imaging in living mice. *Nano Letters* **10**, 2168–2172 (2010).

61. Lizzi, F. L. *et al.* Ultrasonic spectrum analysis for tissue assays and therapy evaluation. *International Journal of Imaging Systems & Technology* **8**, 3–10 (1997).

62. Oraevsky, A., Karabutov, A. Ultimate sensitivity of time-resolved opto-acoustic detection. *Biomedical Optics* **3916,** 228-239 (2000).

63. Xu, Y., Wang, L. V, Ambartsoumian, G. & Kuchment, P. Reconstructions in limited-view thermoacoustic tomography. *Medical physics* **31**, 724–33 (2004).

64. Lizzi, F. L., Greenebaum, M., Feleppa, E. J., Elbaum, M. & Coleman, D. J. Theoretical framework for spectrum analysis in ultrasonic tissue characterization. *The Journal of the Acoustical Society of America* **73**, 1366–1373 (1983).

65. Liu, W. & Zagzebski, J. A. Trade-offs in data acquisition and processing parameters for backscatter and scatterer size estimations. *IEEE transactions on ultrasonics, ferroelectrics, and frequency control* **57**, 340–52 (2010).

CHAPTER 6

SUMMARY AND FUTURE DIRECTIONS

"What I am going to tell you about is what we teach our physics students in the third or fourth year of graduate school... It is my task to convince you not to turn away because you don't understand it. You see my physics students don't understand it... That is because I don't understand it. Nobody does."

-Richard P. Feynman (1918-1988)
picture from http://www.goodreads.com/author/show/1429989.Richard_P_Feynman

6.1 Summary

Prostate cancer is a common disease among men in developed countries and, fortunately, has a relatively high survival rate provided diagnosis occurs in its early stages [1]. However, methods of detection of the disease in its early stages remain unreliable due to the limitations of current diagnosis techniques [2]. Furthermore, treatments of early-stage prostate cancer, when diagnosed, are often associated with adverse side effects [3]. New treatment options for early-stage prostate cancer which have minimal to no side effects are available [4], but lack adequate monitoring tools. There is, thus, a growing need for techniques that are be capable of detecting prostate cancer with high contrast and high resolution, as well as modalities for monitoring these new, preferable prostate cancer treatments.

OA imaging has been demonstrated to acquire high contrast and resolution images in real-time [5]. This thesis addresses one of the major limitations with OA imaging of prostate cancer; the need to use planar detection geometry in prostate imaging, which is often associated with relatively lower resolution when operating in real-time [6–8]. Frequency analysis of OA signals, described herein, may offer a means of providing sub-resolution detail to low resolution OA images. This could greatly enhance the applicability of OA imaging in prostate cancer detection and monitoring by providing sub-resolution detail about the vasculature of the tumour (which is indicative of its aggressiveness), and physical changes that occur during treatment that indicate successful tumour destruction. This analytical technique could strengthen all OA imaging applications, by providing complementary information to the current amplitude based analysis technique.

The experiments presented in this thesis aim to determine if optoacoustic signal intensity and frequency are sensitive indicators of physiological differences between healthy and neoplastic tissues, and to treatment-induced physiological changes.

Before focusing on the cancer-related studies (i.e. cancer detection and therapy monitoring) the OA imaging system is characterized (Chapter 2). The sensitivity, reproducibility, resolution and contrast (based on absorption coefficient) of the system was determined. Knowledge of these parameters is essential for setting up the following experiments. The sensitivity and reproducibility allow us to choose sample sizes (e.g. of *in vivo* animals, *ex vivo* tissue) that would yield results with high statistical power while limiting the number of animals sacrificed. The resolution of the system was determined to be approximately 0.5 mm and the contrast of the system is capable of distinguishing targets with absorption coefficients that differed by more than 0.2 cm^{-1}. Therefore, when choosing an animal model for the *in vivo* studies the tissues to be detected must be at least 0.5 mm in diameter at the time of imaging and the absorption coefficients must differed from the surround tissues by more than 0.2 cm^{-1}. Thus, the absorption coefficients of TRAMP tumours compared to absorption coefficients of mouse prostate, and the absorption coefficients of mouse liver and kidney compared to the surrounding tissues differ by at least 0.2 cm^{-1}.

The SENO system has a relatively large pulse energy variation. This may necessitate larger sample sizes and larger signal averaging to be performed to ensure our results are valid. The annular array transducer is optimal for maximum intensity and integrated amplitude projection images. The planar geometry detects large signals at boundaries which could be projected onto a two-dimensional plane to form the image.

The distance that a target is placed from the transducer, however, greatly impacts the amplitude of the detected signal (detected signal amplitude decreases up to 50% when the target is 5 mm away from the focal point of the transducer). Therefore, targets could be imaged using this transducer at greater depths than those demonstrated in this thesis (>5 mm), if the laser energy is sufficient, and if the targets are positioned close to the transducers focus. This degradation of detected signal also demonstrates that this system would not be optimal for three-dimensional imaging.

The main research topics (i.e. prostate cancer detection and therapy monitoring) are presented in Chapters 3-5. Chapter 3 describes the *in vivo* experiment which demonstrates the ability of OA imaging to detect tumours with high contrast and good resolution. The major technical limitations of this study are the long image acquisition time (approximately 1.5 hours for each image) and that individual blood vessels are not well resolved. A novel analytic technique (frequency spectrum analysis) is further developed and employed. This technique shows promise in providing sub-resolution information that may be complementary to the information content in amplitude-based images. Spectrum analysis involves removing system-dependent features by calibrating the spectrum with the frequency spectrum of the transducer. Three frequency parameters (the slope, intercept and midband fit) are extracted from this calibrated spectrum. The changes in these parameters could be quantitatively compared with parameters obtained using different OA systems (OA data cannot currently be quantitatively compared between systems).

The greatest challenge of this study is the interpretation of the detected OA signals. Significant differences in the amplitude of the OA signals are found on tumour

compared to surrounding tissues, however, this is not solely due to increased hemoglobin concentrations (and therefore absorption coefficients) as some of the tumours were visually not highly vascularized. The changes in the signal may be due to the differences in the Grűneisen parameter between normal and neoplastic tissues [9]. Significant differences in the frequency spectrums are also found. This is interesting and important data as our understanding of the connection between the frequency of the OA signal and the specific target characteristics is limited. This data leads to future studies (Chapter 5) to investigate the connection between the size and density of OA targets and the frequency spectrum of the resulting signals. Using these results, the larger slope value on tumour compared with surrounding tissues indicates that the tumours are composed of blood vessels with smaller diameters, on average. The higher intercept and midband fit values on tumour, in combination with the higher slope values, indicate that the tumours have a more dense network of blood vessels than the surrounding tissues. These interpretations are consistent with the known characteristics of the TRAMP model in that the neoplastic prostate tissue consist of smaller and more dense blood vessels compared to normal prostate [10–12].

Chapter 4 demonstrates the ability of OA imaging to monitor laser thermal therapy (LTT), by monitoring the change in OA signal strength (which is directly related to target temperature) during treatment, in real-time. Post-heating (i.e. after the heating laser is turned off) as the tissue temperature decreased back to its initial temperature, the OA signal decreases slightly but remained higher than pre-treatment values. This demonstrates that the amplitude of the OA signal is simultaneous affected by the temperature as well as the physical state of the tissue. These two effects are difficult to

decouple and make OA monitoring of either temperature alone or tissue state alone very difficult. Frequency spectrum analysis is performed on the data and the frequency parameters of the OA signals do not change when the heating laser is turned off and the tissue temperature decreases. This indicates that the frequency of the OA signals may be related to the state of the tissue (e.g. native or damaged/coagulated) more so than to the temperature (which is used as a surrogate for damage). This may offer a more direct method to detect and monitor tissue coagulation during thermal therapy compared to OA temperature prediction.

Chapter 5 further investigates the relationship between the target and the frequency spectrum of the OA signal. A phantom experiment is performed to determine the relationship between the frequency parameters (the slope, midband fit and intercept) and the size and concentration/density of the targets. The frequency parameters of two casted and *in vivo* tissues (mouse liver and kidneys) are measured and compared under the hypothesis that the frequency spectrum would be affected by the different vascular characteristics of the tissues (e.g. vessel diameters and densities). Both casted and *in vivo* hepatic vasculatures have higher associated slope and midband fit values compared to those associated with renal vasculature. These results, in combination with the results of the phantom study, are compared with published values of the density and sizes of the vessels of these two tissues (renal vasculature has larger vessels and lower vascular density on average compared to hepatic vasculature). Based on the phantom study results, targets with larger vessel diameters and less vascular density would yield greater slope values and smaller midband fit and intercept values. These experimental OA slope values for renal and hepatic vasculature are consistent with the known differences

in vascular size and density. Characteristics associated with mouse hepatic and renal vasculature, obtained via CT imaging of the vascular casts and literature, are input into a computer script which simulates three-dimensional vascular trees of hepatic and renal vasculature and their associated OA signals. Frequency analysis is then performed on these simulated signals and, as with the cast and *in vivo* data, the slope and midband fit values associated with hepatic vasculature are higher than those associated with renal vasculature.

This thesis addressed one of the major limitations of the use of OA for the imaging of prostate cancer. Due to the location of the prostate gland, planar detection geometry must be employed in OA imaging which is associated with relatively low resolution when performed in real time. The frequency-based analysis developed and tested in this thesis should contribute additional information on sub-resolution structures to OA images, which may provide for advanced detection and monitoring of prostate cancer. Differences in vascular characteristics (between hepatic and renal vasculature) resulted in significant differences between the frequency parameters while the OA signal amplitude do not. Neoplastic and the surrounding prostate tissues show significant differences in both the frequency and amplitude of the OA signal. This analysis technique could be applied to any OA signal to provide additional information on sub-resolution tissue structures. This would be especially important for low resolution systems. Once the tumour is located, OA imaging can be used to monitor laser thermal therapy (LTT) in real-time. The frequency spectrum of the OA signals may indicate tissue state (i.e. native and coagulated) rather than temperature based on the result in Chapter 4. In combination with the amplitude of the OA signal, this may

provide the first treatment monitoring system for LTT which could provide temperature as well as tissue state information simultaneously. This would be by far the most important finding of this thesis, from the clinical perspective.

6.2 Future directions

There are many possibilities for further exploration arising from the work presented in this thesis, some of which have been noted in previous chapters. Given the novelty of the frequency analysis technique and the limited published material exploring this technique, the potential for future study is understandably substantial. While the focus of this thesis was on prostate cancer detection and treatment monitoring, it is reasonable to assume that other OA imaging applications would benefit from this technique.

Future studies directly stemming from this study could include further investigation into the relationship between the target characteristics (e.g. size, concentration, shape, etc) and the OA spectrum parameters. Comprehensive studies must be performed to investigate this relationship, involving reliable phantoms with specific and varying physical characteristics (similar to the microsphere phantoms in Chapter 5). Furthermore, the analysis technique used herein closely mimics that used in ultrasound image analysis. Modifications to this technique may improve its validity. For example, the optimal method used to calibrate the RF tissue power spectrum (i.e. obtain the power spectrum of the transducer) is still unclear [13,14]. Vascular corrosion casts used for modeling complex vascular structures may be a valuable tool for investigating the relationship between the frequency response of the OA signal and a

complex vascular target. Investigating vascular casts of tumours would be especially critical to advance the applicability of this technique.

An *in vivo* study similar to the one performed in Chapter 3 with a larger number of animals may provide more accurate results. A system with improved stability in laser pulse energy is desirable as it would reduce required signal averaging and likely improve the overall reproducibility. In addition to tumour detection, laser thermal therapy (LTT) could also be performed in real-time and monitored using OA imaging in these models. This is necessary to determine the affects of parameters such as blood flow on the OA signal amplitude and frequency spectrum during and post-heating. The logical progression to advance this technique to a medically applicable state would then be to transition these studies into a more complex model (e.g. canine prostate) which would require the development of a transrectal OA system.

References

1. Shah, N. L. & Sanda, M. Health-related quality of life in treatment for prostate cancer: looking beyond survival. *Supportive Cancer Therapy* **1**, 230–236 (2004).

2. el-Gabry, E., Halpern, E. J., Strup, S. E. & Gomella, L. G. Imaging prostate cancer: current and future applications. *Oncology (Williston Park, N.Y.)* **15**, 325–336 (2001).

3. Eton David T, L. S. J. Prostate cancer and health related quality of life: a review article. *Psychooncology* **11**, 307–326 (2002).

4. Turkbey, B., Pinto, P. A. & Choyke, P. L. Imaging techniques for prostate cancer: implications for focal therapy. *Nature Reviews.Urology* **6**, 191–203 (2009).

5. Xu, X.-H. & Li, H. Photoacoustic imaging in biomedicine. *Physics - Beijing* **37**, 111–119 (2008).

6. Beard, P. Biomedical photoacoustic imaging. *Interface focus* **1**, 602–31 (2011).

7. Laufer, J., Zhang, E., Raivich, G. & Beard, P. Three-dimensional noninvasive imaging of the vasculature in the mouse brain using a high resolution photoacoustic scanner. *Applied Optics* **48**, D299–D306 (2009).

8. Hu, S. & Wang, L. V Photoacoustic imaging and characterization of the microvasculature. *Journal of Biomedical Optics* **15**, 11101 (2010).

9. Yao, D.-K. & Wang, L. V. Measurement of Grüneisen parameter of tissue by photoacoustic spectrometry. *SPIE BiOS* 858138 (2013).doi:10.1117/12.2004117

10. Gingrich, J. R., Barrios, R. J., Foster, B. A. & Greenberg, N. M. Pathologic progression of autochthonous prostate cancer in the TRAMP model. *Prostate Cancer & Prostatic Diseases* **2**, 70 (1999).

11. Gingrich, J. R. *et al.* Metastatic prostate cancer in a transgenic mouse. *Cancer research* **56**, 4096–4102 (1996).

12. Marvin, H. E. *et al.* Basic Science: Early castration reduces prostatic carcinogenesis in transgenic mice. *Urology* **54**, 1112–1119 (1999).

13. Kumon, R. E., Deng, C. X. & Wang, X. Frequency-Domain Analysis of Photoacoustic Imaging Data From Prostate Adenocarcinoma Tumors in a Murine Model. *Ultrasound in medicine & biology* **37**, 834–839 (2011).

14. Xu, G. *et al.* Photoacoustic spectrum analysis for microstructure characterization in biological tissue: A feasibility study. *Applied physics letters* **101**, 221102 (2012).